Curved and bimorph piezoelectric micromachined ultrasonic transducers (PMUT)

By

Sina Akhbari

A dissertation submitted in partial satisfaction of the

requirements for the degree of

Doctor of Philosophy

in

Engineering – Mechanical Engineering

in the

Graduate Division

of the

University of California, Berkeley

Committee in charge:

Professor Liwei Lin, Chair
Professor George C. Johnson
Professor Tsu-Jae King Liu

Spring 2016

Curved and bimorph piezoelectric micromachined ultrasonic transducers (PMUT)

by

Sina Akhbari

Abstract

Curved and bimorph piezoelectric micromachined ultrasonic transducers (PMUT)

by

Sina Akhbari

Doctor of Philosophy in Mechanical Engineering

University of California, Berkeley

Professor Liwei Lin, Chair

Ultrasonic transducers have been realized as nondestructive tools for a variety of applications, such as medical imaging, diagnosis, therapy, nondestructive testing, range finding, and gesture recognitions. Ultrasonic transducers fabricated by MEMS (Microelectromechanical Systems) technologies are known to have distinct advantages over conventional ultrasound devices in terms of device resolution, bandwidth, power consumption, and cost. This work focuses on innovative architectures of Piezoelectric Micromachined Ultrasonic Transducers (pMUT) for improved electro-mechano-acoustical energy efficiency and increased sensitivity using CMOS-compatible fabrication. Specifically, curved and dual-electrode bimorph (DEB) pMUT structures have been proposed and demonstrated; pMUT systems in the form of large arrays have been analyzed and simulated; as a proof-of-concept demonstration, a DEB pMUT device has been shown for potential muscle spasm diagnosis application in power-efficient hand-held medical systems.

Highly responsive curved pMUT devices have been constructed using a curved AlN layer. Prototype curved pMUTs have resonant frequencies between 1 to 4 MHz and it has been shown that curved pMUTs can in practice have 50X higher low frequency displacement per input voltage and higher electromechanical coupling comparing to flat pMUTs of the same piezoelectric material, lateral size and resonant frequency. The dynamic equations of motion of spherically-curved piezoelectric elastic shells have also been derived followed by analytical equivalent circuit modeling of curved pMUT and the results match well with the FEA simulations and experimental results.

The concept, basic theory, fabrication, and testing results of dual-electrode bimorph (DEB) pMUT for both air- and liquid-coupled applications have also been presented in this thesis. Both theoretical analyses and experimental verifications under the proposed differential drive scheme display high drive sensitivity and an electromechanical coupling energy efficiency that is as high as 4X of the state-of-the-art pMUT with similar geometry, material,

and frequency. The prototype transducers are fabricated in a CMOS-compatible process with radii of 100-230 μm using aluminum nitride (AlN) as the piezoelectric layers with thicknesses varying from 715 nm to 950 nm, and molybdenum (Mo) as the electrodes with thicknesses of 130 nm. The tested operation frequencies of the prototype transducers are 200-970 kHz in air for possible ranging and motion detection applications, and 250 kHz to 1 MHz in water for medical ultrasound applications such as fracture healing, tumor ablation, and transcranial sonothrombolysis. A 12×12 array structure is measured to have the highest intensity per voltage squared, per number of pMUTs squared, and per piezoelectric constant squared ($I_n = I/(VNd_{31})^2$) among all reported pMUT arrays. The generated acoustic intensity is in the range of 30-70 mW/cm^2 up to 2.5 mm from the transducer surface in mineral oil with a driving voltage of 5 V_{ac}, which is suitable for battery-powered therapeutic ultrasound devices.

Equivalent circuit models of large arrays of curved (spherical-shape) and flat pMUTs have been developed for complex pMUT arrays design and analysis. The exact solutions for circuit parameters in the electromechanical domain, such as: mechanical admittance, input electrical impedance, and electromechanical transformer ratio were analytically derived. The array model includes both the self- and mutual-acoustic radiation impedances of individual transducers in the acoustic medium. Volumetric displacement, induced piezoelectric current, and pressure field can be derived with respect to the input voltage matrix, material and geometrical properties of each individual transducer and the array structure. As such, the analytical models presented here can be used as a guideline for analyses and design evaluations of large arrays of curved and flat pMUTs efficiently, and can be further generalized to evaluate other pMUT architectures in form of single-devices or arrays.

Finally, we have successfully demonstrated DEB pMUT arrays capable of detecting slight variations in mechanical properties of samples with similar characteristics to human muscles. It has been experimentally shown that 5.9% speed of sound difference between two PDMS samples can be detected by a 1D DEB pMUT array operating in pulse-echo mode at 300 kHz and driving voltages as low as 2 V_{pp}. As such, DEB pMUT arrays can be implemented in battery-powered handheld devices like cell-phones or used as dermal patches with external communication devices for real-time or off-line monitoring of muscle spasm due to ergonomics and repetitive strain.

To my parents: Afsaneh & Saeed.

TABLE OF CONTENTS

LIST OF FIGURES

LIST OF TABLES

ACKNOWLEDGEMENTS

First and foremost, I would like to thank my parents Afsaneh and Saeed for raising me with care, passion, and love. In every milestone I accomplished, I had their support and advice throughout the way. They are the kindest, wisest, and the best people I have ever known and I am truly blessed to be a son to these angels.

I would like to thank my advisor Prof. Liwei Lin for his help and guidance throughout my PhD. He is one of the most efficient and understanding directors I have ever had a chance to work with, and I greatly appreciate his approach and support in letting me explore my ideas and not micromanaging me, but at the same time showing me the big picture and reminding me of the major goals needed to be fulfilled whenever was necessary. I would also like to thank my qualifying examination and thesis committee members Prof. George Johnson and Prof. Tsu-Jae King Liu for their great advice and support.

During my PhD work I had the privilege of meeting and collaborating with Dr. Firas Sammoura, who is one of the most intelligent people I have ever known, and whose ongoing research has provided the inspiration and impetus for a large portion of my PhD work. I greatly appreciate his help and support. I would also like to thank Dr. Chen Yang, who is one of the most righteous, modest, caring, and hardworking colleagues I have ever had. He basically taught me all the necessary ins and outs of microfabrication processing so that I could develop my own process flows. It has always been inspiring, fruitful, and fun to bounce ideas off these two.

I am also very glad that I had labmates like Mr. Yumeng Liu, Miss Xining Zang, Dr. Roseanne Warren, Mr. Eric Sweet, Mr. Ilbey Karakurt, Mr. Casey Glick, Mr. Hyun Sung Park, Mr. Caiwei Shen, Miss Emmeline Kao, and Mr. Kaiyuan Yao that always helped and supported me with kindness. I would also like to thank my labmate and colleague Mr. Benjamin Eovino for his great work and help on this project, and I am looking forward to seeing his great future work. I am also very glad to have the chance to work with Dr. Nazly Pirmoradi on a side project during my PhD. Overall, I want to thank all my labmates in the Linlab for building such a creative and amazing lab environment.

I would also like to thank Prof. David Horsley from UC Davis and his lab, especially Dr. Amir Heidari, Dr. Hadi Najar, Dr. Yipeng Lu, Dr. Stefon Shelton, Dr. André Guedes, Mr. Parsa Taheri, and Miss Joy Jiang for their collaboration and their kind help and support - especially in some of the measurement data. In addition, I am thankful for the great help and work on ASIC design and testing from Prof. Jerald Yoo and his student Ms. Judyta Tillak from Masdar Institute of Science and Technology, and Mr. Zhikang Li from Xi'an Jiaotong University for his help with PCB design and some aspects of theoretical work. I would like to thank Dr. Arne Voie from BURL Concepts Inc for his work on some parts of the acoustic measurements. Furthermore, I would like to thank my uncle Dr. Behnam Akhbari for the technical advice and great insight he offered into some of the potential medical applications of this work. I am also grateful to my aunt Ms. Behnaz Shahedian, whose kind help and unconditional support was there to guide me whenever I needed.

The development and execution of new microfabrication processes is a lengthy and involved task, so I would like to thank all the Berkeley Marvell Nanofabrication Lab staff for their aid, especially Mr. Ryan Rivers, Dr. Jeffery Clarkson, Mr. Joseph Donnelly, Mr. Jay Morford, Mr. Richelieu Hemphill, and Ms. Kim Chan. The successful fabrication of the devices made throughout my PhD was made possible by the help and invaluable advice of this team.

I am also very lucky to have such a unique combination of genius, supportive, and chill friends like Mr. Ahmad Zareei and Mr. Sajjad Moazeni here in Berkeley, who were always kindly willing to spend time with me on both scientific and research-related materials as well as fun activities. I would like to thank my friend Dr. Behrooz Shahsavari, who is my first Berkeley friend and has always been a great support to me, as well as Dr. Behnam Behroozpour, whose valuable insight helped me learn much of the circuit-related aspects of my research. I also want to thank my Berkeley housemate and good friend Mr. Matthew Plinck for his genuine friendship and support. He is one of the most inspirational individuals in human growth and progress matters that I have ever met.

As the only child of our family, I am very grateful to have such awesome and lovely cousins like Hedi, Mani, Parimah, Rouzbeh, Hamid, Hasti, Shaya, Tous, Niloo, Kati and the rest that always made me laugh, even from thousands of miles away, and made me never feel lonely as I grew up. I have plenty of wonderful and invaluable memories with them since I was a little kid. I would also like to thank my grandparents Majid (*RIP*), Badri, Masoumeh, and Reza (*RIP*) for raising my parents, helping them raise me, and for their endless love and support. I am also very thankful to have the most amazing friends like Babak Nasouri, Morteza Amini, Farzad Jouzi, Reza Nasouri, Sahand Golnarian, Farhad Fallah, Reza Nouri, Takin Ghavimi, Zhaleh Amini, Pouria Kourehpaz, Delagah Dadbeh, Saghi Sadoughi, Ali Moin, Sayna Ebrahimi, Karen Diepstra, Alex Krohn, Moe Kamal-Aldin, Sadegh Asefi, and Amirhesam Afarin that tolerated me for years and who I have experienced the greatest and the most unforgettable memories with. I also owe thanks to all my family and friends from Iran, USA, and the rest of the world whose names I may not have been able to include here, but whose kindness and support will never be forgotten.

For as long as I can remember, music has provided me with an escape, inspiration, and so much more. In particular, I would like to acknowledge my favorite artist and musician Mr. Maynard James Keenan for his unique and excellent work, and his creation of the most splendid music groups like the world’s best band of all time, Tool, which I have been listening to constantly throughout my college years and PhD. I also want to thank the rest of the Tool band members: Adam Jones, Danny Carey, Justin Chancellor, and Paul D’Amour for creation and performance of such world-class, rich, complex, and inspirational music/art.

Finally, I would like to thank BURL Concepts Inc., Berkeley Sensor and Actuator Center (BSAC), and GlobalFoundries Singapore Pte. Ltd. under Abu Dhabi-Singapore Twin Lab between the Institute of Microelectronics (IME) and Masdar Institute of Science and Technology, Abu Dhabi, UAE for their contribution in funding this project.

Chapter 1

Introduction

1.1. Ultrasonic Transducers

Ultrasonic transduction has been realized as a remarkable transmitting and receiving mechanism for a variety of applications, such as medical imaging, nondestructive testing, sonar systems, range finding, gesture recognition, and therapeutic treatments [1]-[7]. The current state-of-the-art ultrasonic devices utilize bulk piezoelectric materials such as PZT (lead zirconate titanate) in the thickness mode acting as the transduction element to convert electrical energy to mechanical vibrations for acoustic wave emissions, and vice versa [8]. Microelectromechanical Systems (MEMS) devices, fabricated by means of micromachining technology, have several potential advantages over the conventional ultrasonic transducer technologies, including: small size and batch fabrication for low manufacturing cost, flexibility in frequency ranges with flexural mode operations, and high resolution. MEMS ultrasound devices are commonly known as Micromachined Ultrasonic Transducers (MUT) with two types of driving and sensing mechanisms: capacitive (cMUT) [9] and piezoelectric (pMUT) forms [10]. They can be fabricated in small sizes for high frequency applications and high resolutions with low power consumption. Furthermore, they have better impedance matching to medium than the thickness mode designs, thereby enabling wider bandwidths.

In general, cMUTs have high electromechanical coupling factors but are often constrained by the nonlinear drive effects with limited vertical deformations, and require high DC bias voltages [11]. On the other hand, pMUTs have linear drive responses, high vertical deformation, and low driving voltages with no DC biasing requirement [12], but typically have lower electromechanical coupling factors. The maximum achievable electromechanical coupling factor for pMUTs is a function of the material properties as well as the geometry and the boundary conditions [13]. One common approach to improve the electromechanical coupling factor of pMUTs is through the use of geometric design in the electrodes and diaphragm shapes. For example, Sammoura et al. have demonstrated a two-port pMUT that can improve the acoustic power per unit input voltage up to 100% and suppress the second harmonic effects by 485% [14]. Shelton et al. have introduced a resonant matching tube, etched beneath the pMUT to enhance the acoustic coupling and increase the Sound Pressure Level (SPL) by 350% [15]. Lu et al. have presented a ribbon-shape PZT pMUT based on dual mode resonance with high bandwidth of 97% [16].

1.2. Curved and Bimorph PMUTs

Two pMUT structures have been studied in this thesis as shown in Fig. 1.1, including the theory, design, fabrication and testing of curved pMUT (Fig. 1.1a); and the theory, design fabrication, and experimental performances of the dual-electrode bimorph (DEB) pMUT

(Fig. 1.1b)for air- and water-coupled applications. Since the fabrication processes of these pMUTs are IC-compatible, and in fact, very similar to the state-of-the-art pMUT process, they are excellent substitutes for the current pMUT designs for broad applications [17]-[18].

Previously, several groups have shown that curved-shape diaphragms can improve the electromechanical coupling factors. For instance, Feng et al. have developed dome-shape ZnO transducers based on using a fabrication method in which macro-scale spherical balls have been used to make wax molds with parylene coatings for the curved diaphragms [19]. Morris et al. have investigated the actuation characteristics of curved diaphragms with an initial curvature induced by a static pressure [20]. Hajati et al. have reported a dome-shaped pMUT with high electromechanical coupling factor using PZT (lead zirconate titanate) [21]. Our group solved the dynamic equations of motion of spherically-curved clamped piezoelectric elastic shells, [22] presented equivalent circuit modeling of curved pMUTs [23]-[24], and experimentally showed the superior performance of curved pMUTs over the flat design [25]-[26].

In the area of theoretical analyses, there are several reports on the theoretical analyses of piezoelectric transducers and MUTs. For example, Krimholtz el al. have modeled the lumped-element parameters of thickness-mode piezoceramics using constitutive piezoelectric equations [27]. Lohfink et al. have derived a 1D model for cMUT arrays by FEM simulations using the piston radiator and plate capacitance theory [28]. Wygant et al. showed a mass-spring-damper model of a circular cMUT along with equivalent circuit parameters [29]. Koymen et al. presented a lumped element nonlinear equivalent circuit model for a circular cMUT [30] which is an improved version of the large signal equivalent model by Oguz et al. with the effect of the immersion medium loading [31]. Prasad et al. have presented an analytical two-port, lumped-element model of a piezoelectric composite circular plate using the classical laminated plate theory [32]. Sammoura et al. have modeled flat pMUTs considering multiple ring-shape electrodes and residual stress with equivalent parameters in a circuit model using Green’s function approach, showing good consistency with experiments [33]-[36]. These analyses have been developed to optimize the electrode designs for maximum acoustic pressure per unit input voltage [37]. Furthermore, various techniques have been developed to optimize the performances of pMUTs such as: zero-bias deflection cancelation, higher harmonics suppression, and acoustic pressure per input voltage enhancement using annular and circular electrodes [38].

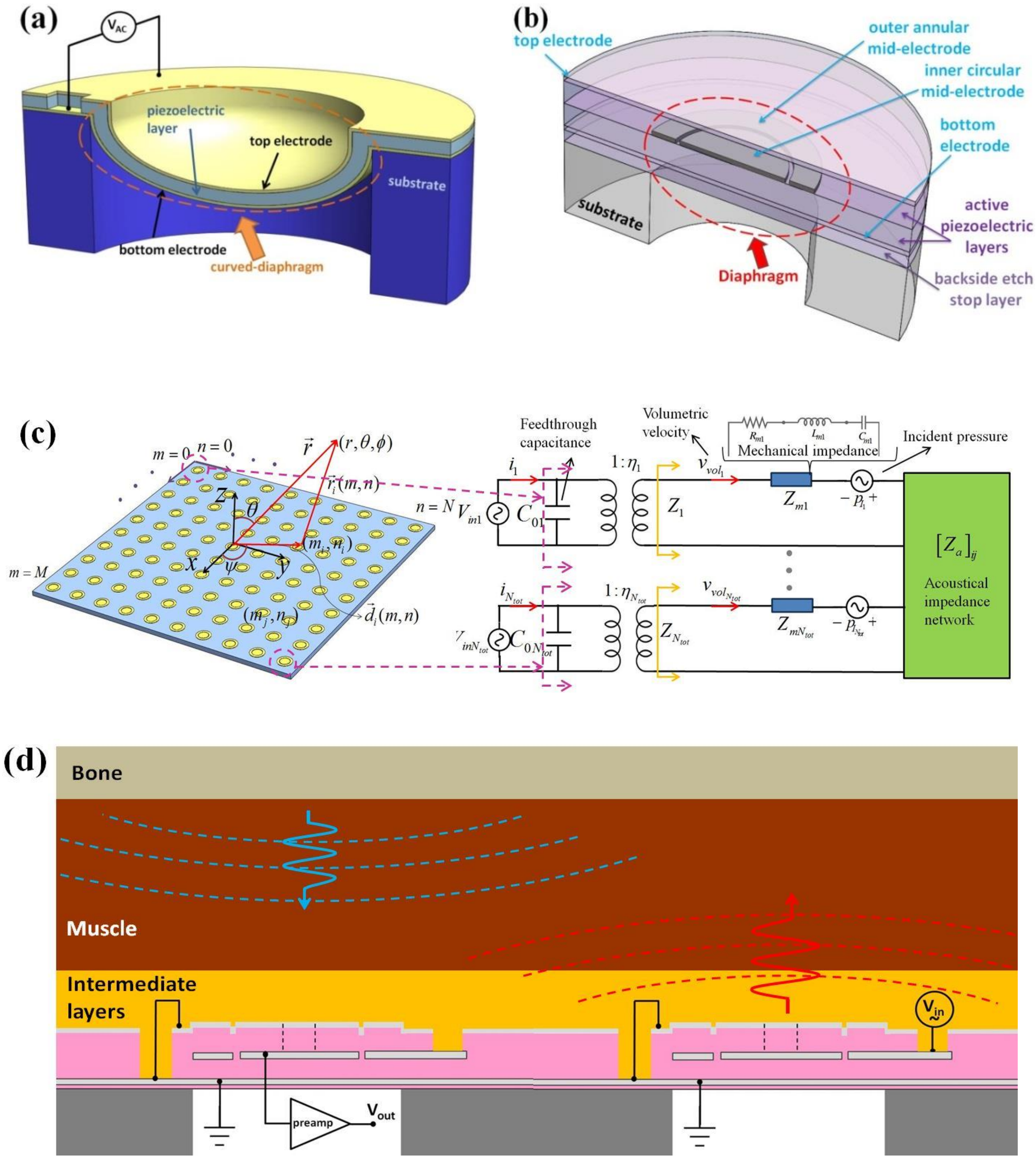

Fig. 1.1. 3D cross-sectional schematic of a (a) curved pMUT, and (b) dual-electrode bimorph pMUT. (c) Equivalent circuit modeling of arrays of pMUTs; (d) DEB pMUT array operating in pulse-echo mode for muscle spasm diagnosis.

Equivalent circuit modeling for clamped bimorph pMUTs with circular and annular electrodes has also been developed using matrix manipulation techniques by Sammoura et al. [39]-[40].

Several works have also analyzed spherical-shape diaphragms. For example, Peng et al. have used Finite Element Modeling (FEM) to analyze single-layer pMUTs with curvature formed by a static pressure difference across the membrane [41]. Toda et al. have derived an analytical model for the vibration modes of clamped, cylindrical transducers with single and double curvatures under piezoelectric actuation [42]. Berry et al. have introduced two fourth-order differential equations for thin, elastic, spherical shells under static radial stress [43]. Naghdi et al. have introduced the free vibration equations of axisymmetric elastic spherical shells and solved for a special case of a hemispherical bell anchored at its apex with free edges [44]. Kino et al. have derived the acoustic radiation of a piezoelectric spherical transducer with constant radial displacement [5]. These are good information for the development of differential equations for the forced vibration of a clamped spherical piezoelectric elastic shell with closed-form solutions as well as equivalent circuit model for clamped curved pMUT with spherical-shape diaphragms in this work.

In the area of array of pMUT systems, a single MUT transducer is similar to an acoustic point source due to its small physical size as compared with the acoustic wavelength (typically diameter over wavelength is between 0.05 and 0.5). Therefore, it is diffraction limited and has no controllability on the generated acoustic beam. In order to form an acoustic beam with certain design specifications such as axial/lateral resolution, bandwidth, and acoustic intensity, it is desirable to construct an array of transducers to generate the desired acoustic beam. An array also enables beamforming as well as focusing, by means of electronic phase delays. For example, in the cMUT field, Mills et al. showed imaging of carotid artery and thyroid gland using a wafer-bonded cMUT array [45]. Degertekin et al. demonstrated a 64-element annular cMUT array for forward-looking intravascular ultrasound imaging [46]. On the other hand, in the field of pMUT, Dausch et al. have developed a 5×5 2D pMUT array in a frequency range of 4 to 13 MHz for intravascular and intracardiac imaging [47]. Yang et al. have reported ultra-high density 6×6 pMUT arrays for 3D medical imaging applications using the Si-SOI bonding method [48]. Lu et al. have reported a 72×9 aluminum nitride pMUT array for high resolution (<100 µm) millimeter range imaging [49]. Jung et al. have fabricated a 2D 32×32 pMUT array using the top-crossover-to-bottom structure and metal bridge connections suitable for applications in medical imaging, ultrasonic communication, and range finding [50]. Przybyla et al. have demonstrated a 3D ultrasonic rangefinder with $\pm 45^{o}$ field of view and 1 m range, using AlN pMUT elements for transmission and receiving [51]. However, none of the aforementioned reports has equivalent circuit models for the experimentally demonstrated system, which limits their ability to do performance estimation and design optimization.

In order to estimate the array performance for the optimal system designs, it is important to model the acoustic responses of the pMUT array. Commercial Finite Element programs have difficulties in processing large arrays of transducers simultaneously involving complicated multi-physics [52], [53]. Theory-based acoustic simulators only consider the acoustic responses of the transducers with pre-defined displacement and frequency and do not take into account the electromechanical and mutual coupling of transducers [54], [55]. Therefore, analytical models for large arrays of pMUTs would be desirable for system-level designs and optimizations. In this area, Sherman and Butler have developed the theoretical modeling of arrays of thickness mode piezoelectric transducers for underwater applications [4]. Bayram et al. showed experimental characterization and FEM modeling of crosstalk in a 1D cMUT array by demonstrating dispersive guided modes as the main crosstalk mechanism [56]. Oguz et al. have shown circuit-based analysis of the dynamics of the individual elements for cMUT arrays [57], including mutual- and self-impedances of acoustic radiation of the flexural mode-transducers [58]. Senlik et al. analytically solved the radiation impedance of an array of circular cMUT using their velocity profiles for frequencies up to the parallel resonant frequency [59]. This thesis has developed an equivalent circuit modeling of arrays of pMUTs as shown in Fig. 1.1c to analyze the complex acoustic behaviors of a large array of pMUTs.

1.3. Dissertation Organization

In chapter 2, the differential equations for the forced vibration of a spherical piezoelectric elastic shell and closed-form solutions for both radial pressure and electric potential with clamped boundary conditions will be derived and described [22]. Afterwards, an analytical equivalent circuit model for curved pMUTs with spherical-shape diaphragms [23]-[24] is developed with detailed derivations of the acoustic radiations of such transducers [24]. Design, fabrication and experimental results from a CMOS-compatible aluminum nitride curved pMUT would show more than one-order of magnitude higher DC displacement per input voltage as compared with a flat pMUT of similar geometry and frequency [25]-[26].

In chapter 3, we present the concept of dual electrode bimorph (DEB) pMUT and show both theoretically and experimentally that the drive sensitivity and energy efficiency of the DEB pMUT are 4X those of a single-electrode unimorph pMUT with similar geometry and mechanical properties. Furthermore we show the fabrication and testing of both air- and liquid coupled DEB pMUTs, and finally in this chapter, we demonstrate that DEB pMUT arrays can generate high enough acoustic intensity at low input driving voltage which makes them suitable for implementation in battery-powered medical handheld devices.

In chapter 4, several advancements in terms of modeling and analyses of a large array of pMUTs are presented, including: (1) an analytical equivalent circuit model for a curved pMUT with explicit expressions for equivalent circuit parameters; (2) the acoustic radiation and impedance of a curved pMUT in the flextensional mode; and (3) a theoretical model capable of solving large arrays of curved and flat pMUTs including both self- and mutual-impedances of acoustic radiation based on the established methods for thickness-mode piezoelectric devices and cMUT arrays [4], [57]. These models are capable of extracting electro-mechano-acoustic parameters with respect to arbitrary electrical or acoustical actuation inputs.

Chapter 5 describes one potential application of pMUT arrays in portable medical devices. It is experimentally shown that slight mechanical variations, such as change of speed of sound, in muscle mimicking materials made of Polydimethylsiloxane (PDMS) can be detected using a 1D DEB pMUT array operating in the pulse-echo mode. Using FEA simulations and operating under the continuous mode (CW), it is shown that the variations of speed of sound between different materials can be projected as a higher pressure variation at the receiver to enhance the device sensitivity. The electrical cross-talk is also modeled for future signal processing purposes. These results indicate that such pMUT arrays operating at voltages as low as 2 V_{pp} could be implemented in portable medical devices for applications such as muscle spasm diagnosis due to ergonomics and repetitive strain (Fig. 1.1d).

Chapter 6 concludes the thesis by summarizing the work on high-efficiency CMOS-compatible pMUT structures, including curved and DEB pMUT, array modeling, and the applications of these transducers.

Chapter 2

Curved PMUT

2.1. Introduction

As mentioned in chapter 1, it has been previously shown that curved-shape diaphragms can enhance the electromechanical coupling factors of diaphragm-type transducers operating in flexural mode [19]-[21]. In this chapter we first present the concept of curved pMUT and the intuition behind its higher electromechancial coupling. Then we derive the differential equations for the forced vibration of a clamped spherical piezoelectric elastic shell and introduce closed-form solutions for the forced vibration equations [22]. Afterwards, we derive an analytical equivalent circuit model for curved pMUTs with spherical-shape diaphragms [23-24] and derive acoustic radiation and impedance of such transducers [24]. Finally we show the experimental results from a CMOS-compatible aluminum nitride curved pMUT with more than one-order of magnitude higher DC displacement per input voltage as compared with flat pMUT of similar geometry and frequency [25-26].

In summary, this chapter presents the concept of "curved pMUT" with several unique accomplishments: (1) theoretical vibration analyses and equivalent circuit modeling of curved pMUT with spherical-shape diaphragms and clamped boundary conditions. (2) CMOS-compatible fabrication processes using AlN as the piezoelectric layer; (3) experimental validations of optimal curved pMUT designs demonstrating more than one-order of magnitude increase in low frequency displacements per input voltage as compared with flat pMUTs of similar geometry, material, and resonant frequency.

2.2. Concept

Figure 2.2.1(a) shows the schematic diagram of the state-of-the-art flat pMUT, while Figure 2.2.1(b) shows the proposed curved pMUT. In the flat pMUT, the generated piezoelectric moment is expressed as:

$$M^{P} = Y_0^{'} d_{31}^{'} Z V \tag{2.2.1}$$

where $Y'_{0,}$ is the modified Young's modulus, d'_{31} is the modified piezoelectric charge constant, Z is the distance of the piezoelectric layer from the neutral axis, and V is the applied voltage [35]. In order to excite a flat pMUT, the Laplacian of the piezoelectric moment about the neutral axis of the structure should be nonzero. As a result, an additional structural layer, silicon is shown here as an example, is needed to generate a non-zero piezoelectric moment. In this mechanism a lot of energy would be dissipated through the silicon structural layer.

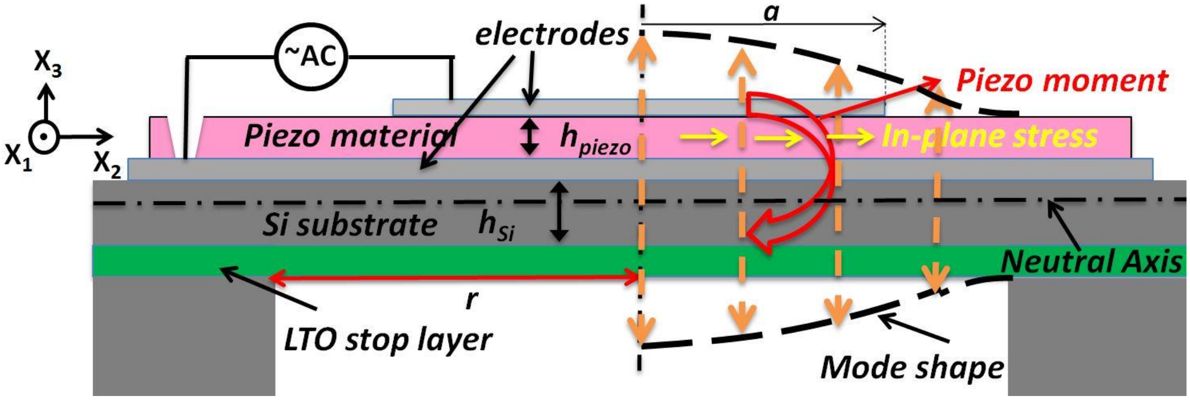

Fig. 2.2.1a. The schematic cross-sectional view of a flat pMUT with the silicon structural layer with height of 'h_{Si}', diaphragm radius of 'r', top electrode radius of 'a', and piezoelectric material thickness of 'h_{piezo}'.

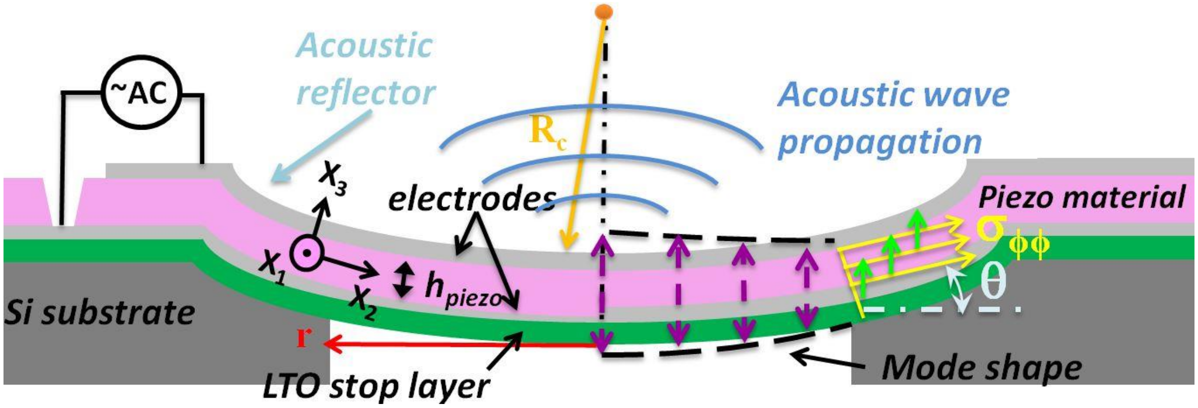

Fig. 2.2.1b. The schematic cross-sectional view of a curved pMUT, which promotes the conversion of in-plane stress '$\sigma_{\phi\phi}$' to vertical mechanical forcing function.

In contrast to a flat pMUT which relies on the large stress mismatch between the structural and the piezoelectric layer due to the in-plane d_{31} effect to create the moment required to induce vertical deformation, the induced piezoelectric membrane strain has a vertical component, which is in the direction of the normal motion, as illustrated in Fig. 2.2.1a. Hence, the curved-shape diaphragm promotes the conversion of membrane strain to vertical mechanical motion for higher electromechanical coupling and acoustic pressure. A simplified formula is derived[1] for the equivalent uniform normal pressure generated on a piezoelectric hemispherical shell under applied voltage V:

---

[1] The derivation is shown in section 2.3.4 and the equivalent pressure can be seen in Eq. (2.3.4.8)

$$p_{piezo} = 2Y_0^{'}d_{31}^{'}V / R_c \tag{2.2.2}$$

where R_c is the radius of curvature of the diaphragm. The normal driving force helps to eliminate the necessity of the additional structural layer to generate a moment about the neutral axis [22]. As such, the piezoelectric layer alone can also serve as the structural layer. It is noted that p_{piezo} goes to zero as the radius of curvature goes to infinity for a flat pMUT.

Curved pMUTs can be constructed based on a CMOS compatible process as illustrated in Fig. 2.2.2. A concave diaphragm, with a radius of curvature of R_c is chosen as the demonstration example by etching a cavity into the silicon substrate. The nominal diaphragm size is determined by the backside through-hole etching process, with an opening radius, r, and the rest of the curved surface serves as acoustic concentrator which could act as a physical lens and further enhance the transduction performances.

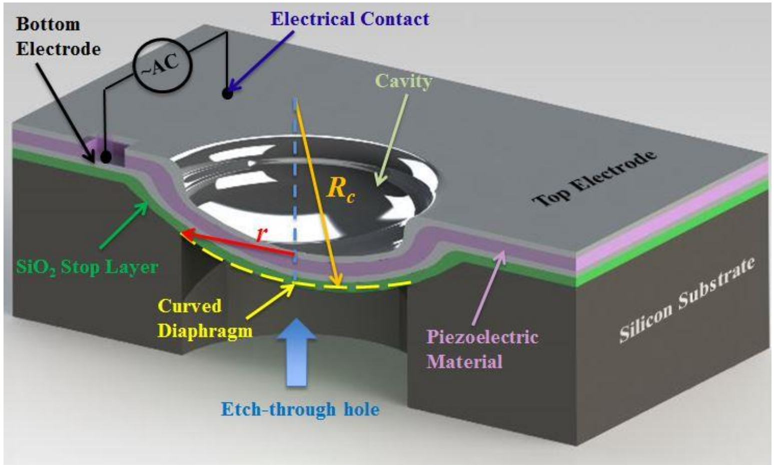

Fig. 2.2.2: 3D schematic of the curved pMUT with a radius of curvature of R_c and diaphragm radius of r, defined by the backside etching opening, based on a CMOS-compatible fabrication process using Aluminum Nitride as the piezoelectric material.

2.3. Vibration Theory of Elastic Piezoelectric Shells

Since the thickness of the structure is much smaller than its surface dimensions (two orders of magnitude), Love's first approximation theory is appropriate for geometrical and dynamic analysis of such device. In this approximation it is assumed that the thickness of the shell is small compared to the other dimensions, the transverse normals to the undeformed middle surface remain straight and normal to the deformed middle surface (i.e. transverse shear strains are negligible), and the strains are infinitesimal so that all nonlinear terms are neglected [61]. Also it is assumed that the transverse normal is inextensible and transverse normal stress is negligible.

2.3.1. Strain-Displacement Relations

Following the notation in [61] we parameterize the shell with $(\zeta_1, \zeta_2, \zeta)$ curvilinear coordinates where the middle surface (located at $\zeta=0$) is parameterized by ζ_1 and ζ_2 curves. In this way, the position of an arbitrary point in the shell, $\mathbf{R}$, can be defined as $\mathbf{R} = \mathbf{r} + \zeta\hat{\mathbf{n}}$

where $\mathbf{r}(\zeta_1, \zeta_2)$ is the position vector of a point on the middle surface and ζ is the distance from the middle surface along the normal vector of that surface, $\hat{\mathbf{n}}$. The geometrical and mechanical parameters are illustrated in Fig. 2.3.1.1.

In a moderately thick shell, which is a more general form of a thin shell, the displacement vector components can be expressed as the following [61]

$$u_i(\zeta_1,\zeta_2,\zeta,t) = u_i^0(\zeta_1,\zeta_2,t) + \zeta\varphi_i(\zeta_1,\zeta_2,t) \quad i=1,2 \tag{2.3.1.1}$$

$$u_3(\zeta_1,\zeta_2,\zeta,t) = u_3^0(\zeta_1,\zeta_2,t) \tag{2.3.1.2}$$

where u_i^0 are the displacement components of a point on the middle surface and φ_i is the rotation of a normal to the reference surface about ζ_j axis ($i \neq j$). By applying Love-Kirchhoff's assumption which results in vanishing of transverse shear strains, the term φ_i can also be expressed as a function of u_i^0

$$\varphi_1 = \frac{\partial u_1}{\partial \zeta} = \frac{u_1^0}{R_1} - \frac{1}{a_1}\frac{\partial u_3^0}{\partial \zeta_1}, \quad \varphi_2 = \frac{\partial u_2}{\partial \zeta} = -\frac{u_2^0}{R_2} - \frac{1}{a_2}\frac{\partial u_3^0}{\partial \zeta_2} \tag{2.3.1.3}$$

where R_i is the radius of the ζ_j=*”a constant value”* coordinate curve ($i \neq j$) and a_i is the magnitude of the tangent vector to ζ_i curve (i.e. ζ_i covariant vector).

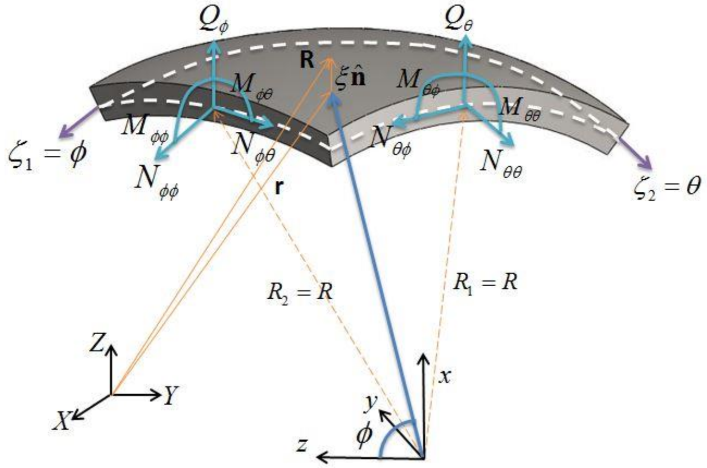

Fig. 2.3.1.1. Stress resultants (N_{ij}), stress couples (M_{ij}) and transverse shear-stress resultants (Q_i) of a shell element

It is common to decompose the total strains of a shell, $\{\varepsilon\}$, into membrane strains, $\{\varepsilon^0\}$, and flexural strains $\{\varepsilon^1\}$

$$\{\varepsilon\} = \{\varepsilon^0\} + \zeta\{\varepsilon^1\} \tag{2.3.1.4}$$

In addition, in every coordinate system, the strains can be expressed as functions of vector displacement components, their derivatives with respect to those curvilinear coordinate parameters and the components of that coordinate system.

Let the shell now be identically spherical, as this $R_1=R_2=R_c$, and let $\zeta_1 = \phi,\ \zeta_2 = \theta,\ u_1^0 = u_\phi,\ u_2^0 = u_\theta,\ u_3^0 = w$. The strain components may then be written as

$$\varepsilon_{\phi\phi}^0 = \frac{1}{R_c}\left(\frac{\partial u_\phi}{\partial \phi} + w\right) \tag{2.3.1.5}$$

$$\varepsilon_{\theta\theta}^0 = \frac{1}{R_c}\left(\frac{1}{\sin\phi}\frac{\partial u_\theta}{\partial \theta} + \cot\phi u_\phi + w\right) \tag{2.3.1.6}$$

$$2\varepsilon_{\theta\phi}^0 = \frac{1}{R_c}\left(\frac{\partial u_\theta}{\partial \phi} - \cot\phi u_\theta + \frac{1}{\sin\phi}\frac{\partial u_\phi}{\partial \theta}\right) \tag{2.3.1.7}$$

$$\varepsilon_{\phi\phi}^1 = \frac{1}{R_c{}^2}\left(\frac{\partial u_\phi}{\partial \phi} - \frac{\partial^2 w}{\partial \phi^2}\right) \tag{2.3.1.8}$$

$$\varepsilon_{\theta\theta}^1 = \frac{1}{R_c{}^2}\left(\frac{1}{\sin\phi}\frac{\partial u_\theta}{\partial \theta} - \frac{1}{\sin^2\phi}\frac{\partial^2 w}{\partial \theta^2} + \cot\phi u_\phi - \cot\phi\frac{\partial w}{\partial \phi}\right) \tag{2.3.1.9}$$

$$2\varepsilon_{\theta\phi}^1 = \frac{1}{R_c{}^2}\left[\frac{\partial u_\theta}{\partial \phi} - \cot\phi u_\theta - \frac{2}{\sin\phi}\frac{\partial^2 w}{\partial\theta\partial\phi} + \frac{2\cos\phi}{\sin^2\phi}\frac{\partial w}{\partial \theta} + \frac{1}{\sin\phi}\frac{\partial u_\phi}{\partial \theta}\right] \tag{2.3.1.10}$$

2.3.2. Constitutive Equations and Stress Resultants

The “intensive-type” (d-form) [62] of the constitutive equations for a linear piezoelectric medium may be written as

$$\varepsilon_{ij} = s_{ijkl}^E \sigma_{kl} + d_{kij} E_k \tag{2.3.2.1}$$

where d_{kij} is the piezoelectric constant, E_k is the electric field, s_{ijkl} is the elastic compliance, ε_{ij} is the strain tensor and σ_{kl} is the stress tensor. From this point we present the piezoelectric constant, electric field, elastic compliance, strain, and stress, into the lumped 2D matrix form, i.e. $\varepsilon_A = s_{AB}\ \sigma_B + d_{CA}\ E_C$ and use spherical coordinate system where θ and ϕ are the lateral components and ζ is the radial component.

In the following derivations, we are assuming that the transverse normal and shear strains would still be negligible. Also the effect of d_{36} piezoelectric constant on the tangential shear strain (i.e. $\varepsilon_{\phi\theta}$) is neglected due to its nominal effect on the desired mode shape according to the boundary condition, hence, on dynamic equations of motion. Thus, the tangential stress components of a curved unimorph piezoelectric thin shell with constant radius of curvature having clamped boundary condition can be expressed as the following

$$\sigma_{\phi\phi} = \frac{Y_0}{1-v^2}\left[\varepsilon_{\phi\phi} + v\varepsilon_{\theta\theta} - (1+v)d_{31}E_{\zeta}\right] \tag{2.3.2.2}$$

$$\sigma_{\theta\theta} = \frac{Y_0}{1-v^2}\left[\varepsilon_{\theta\theta} + v\varepsilon_{\phi\phi} - (1+v)d_{31}E_{\zeta}\right] \tag{2.3.2.3}$$

$$\sigma_{\phi\theta} = \frac{Y_0}{1+v}\varepsilon_{\phi\theta} \tag{2.3.2.4}$$

Now we can express the stress resultants in terms of the strains, the voltage difference between the inner and outer surfaces of the shell, V_r, and the material properties of the shell such as the bending stiffness, $D= Y_0h^3/12(1- v^2)$, shell thickness, h, shell radius of curvature, R_c, Young's module, Y_0, and Poisson's ratio, v as

$$\begin{Bmatrix} N_{\phi\phi} \\ N_{\theta\theta} \\ N_{\theta\phi} \end{Bmatrix} = \int_{bottom}^{top} \begin{Bmatrix} \sigma_{11} \\ \sigma_{22} \\ \sigma_{21} \end{Bmatrix} \left(1+\frac{\zeta}{R_c}\right) d\zeta = \frac{Y_0 h}{1-v^2} \begin{bmatrix} 1 & v & 0 \\ v & 1 & 0 \\ 0 & 0 & \frac{(1-v)}{2} \end{bmatrix} \begin{Bmatrix} \varepsilon^0_{\phi\phi} \\ \varepsilon^0_{\theta\theta} \\ 2\varepsilon^0_{\theta\phi} \end{Bmatrix} - \frac{Y_0 d_{31} V_{\zeta}}{1-v} \begin{Bmatrix} 1 \\ 1 \\ 0 \end{Bmatrix} \tag{2.3.2.5}$$

$$\begin{Bmatrix} M_{\phi\phi} \\ M_{\theta\theta} \\ M_{\theta\phi} \end{Bmatrix} = \int_{bottom}^{top} \begin{Bmatrix} \sigma_{11} \\ \sigma_{22} \\ \sigma_{21} \end{Bmatrix} \left(1+\frac{\zeta}{R_c}\right) \zeta d\zeta = D \begin{bmatrix} 1 & v & 0 \\ v & 1 & 0 \\ 0 & 0 & \frac{(1-v)}{2} \end{bmatrix} \begin{Bmatrix} \varepsilon^1_{\phi\phi} \\ \varepsilon^1_{\theta\theta} \\ 2\varepsilon^1_{\theta\phi} \end{Bmatrix} \tag{2.3.2.6}$$

2.3.3. Equations of Motion

The dynamic equations of motion of a thin piezoelectric elastic shell with constant radius of curvature was derived as the following

$$\frac{\partial}{\partial\phi}\left(\sin\phi N^{'}_{\phi}\right) + \frac{\partial}{\partial\theta}\left(N_{\phi\theta}\right) - \cos\phi N^{'}_{\theta} + \sin\phi Q_{\phi} = \rho h R_c \sin\phi \frac{\partial^2 u_{\phi}}{\partial t^2} \tag{2.3.3.1}$$

$$\frac{\partial}{\partial\theta}\left(N_{\theta}^{'}\right)+\frac{\partial}{\partial\phi}\left(\sin\phi N_{\phi\theta}\right)+\cos\phi N_{\theta\phi}+\sin\phi Q_{\theta}=\rho h R_c\sin\phi\frac{\partial^2 u_{\theta}}{\partial t^2} \tag{2.3.3.2}$$

$$\frac{\partial}{\partial\phi}\left(\sin\phi Q_{\phi}\right)+\frac{\partial}{\partial\theta}\left(Q_{\theta}\right)-\sin\phi\left(N_{\theta}^{'}+N_{\phi}^{'}\right)=\rho h R_c\sin\phi\frac{\partial^2 w}{\partial t^2}-\sin\phi\frac{2Y_0 d_{31}V_{\zeta}}{1-v}-R_c\sin\phi\, p_{\zeta} \tag{2.3.3.3}$$

$$\frac{\partial}{\partial\phi}\left(\sin\phi M_{\phi}\right)+\frac{\partial}{\partial\theta}\left(M_{\theta\phi}\right)-\cos\phi M_{\theta}-R_c\sin\phi Q_{\phi}=0 \tag{2.3.3.4}$$

$$\frac{\partial}{\partial\phi}\left(\sin\phi M_{\phi\theta}\right)+\frac{\partial}{\partial\theta}\left(M_{\theta}\right)+\cos\phi M_{\theta\phi}-R_c\sin\phi Q_{\theta}=0 \tag{2.3.3.5}$$

where p_{ζ} is the pressure-induced forcing function in the ξ direction, Q_{ϕ} and Q_{θ} are the transverse shear stress resultants, and $N_{\phi}^{'}$ and $N_{\theta}^{'}$ are defined as $N_{\phi}^{'}\equiv Y_0 h/(1-v^2)\left[\varepsilon_{\phi}^{0}+v\varepsilon_{\theta}^{0}\right]$ and $N_{\theta}^{'}\equiv Y_0 h/(1-v^2)\left[\varepsilon_{\theta}^{0}+v\varepsilon_{\phi}^{0}\right]$. Also in this notation we have compressed $\phi\phi$, $\theta\theta$ to ϕ and θ respectively. It is interesting to note that equations (2.3.3.1), (2.3.3.2), (2.3.3.3) and (2.3.3.5) are exactly the same as the equations of motion of an elastic spherical shell in the absence of surface load [44]. In fact, the only equation that is changed due to the piezoelectric effect and the external pressure is Eq. (2.3.3.3) which is the dynamic equation in the radial direction.

2.3.4. Solutions for the Differential Equations of Motions

To solve the differential equations of motion we consider the model to be axisymmetric, thus, $\partial/\partial\theta=0$. The compatibility equation, Eq. (2.3.4.1), can be derived by the elimination of $u_{\phi,\phi}$ from Eq. (2.3.2.5) and Eq. (2.3.2.6) where the i index denotes derivation with respect to i and substitution of strains with stress resultants (i.e. $N_{\phi}^{'}$ and $N_{\theta}^{'}$).

$$\tan\phi\left(N_{\theta}^{'}-vN_{\phi}^{'}\right)_{,\phi}+\left(\sec^2\phi+v\right)N_{\theta}^{'}-\left(v\sec^2\phi+1\right)N_{\phi}^{'}=\frac{Y_0 h}{R_c}\tan\phi\left[w_{,\phi}+w\tan\phi\right] \tag{2.3.4.1}$$

Now, as suggested by [44] we define a new function, $F(\phi,t)$, called the stress function, so that

$$N_{\phi}^{'}=\cot\phi F_{,\phi}+F-\frac{\rho(1+v)R_c^{\,2}}{Y_0}\frac{\partial^2 F}{\partial t^2}+\frac{D}{R_c}\left(\nabla^2+\frac{2}{R_c^{\,2}}\right)w \tag{2.3.4.2}$$

$$N_{\theta}^{'}=F_{,\phi\phi}+F-\frac{\rho(1+v)R_c^{\,2}}{Y_0}\frac{\partial^2 F}{\partial t^2}+\frac{D}{R_c}\left(\nabla^2+\frac{2}{R_c^{\,2}}\right)w \tag{2.3.4.3}$$

By expressing u_ϕ in terms of $N_\phi^{'}$ and $N_\theta^{'}$, and substituting for $N_\phi^{'}$ and $N_\theta^{'}$ in Eq. (2.3.3.1) using Eq. (2.3.4.2) and Eq. (2.3.4.3), it is found that $\partial^2\Gamma/\partial t^2 = 0$ where Γ is defined as

$$\Gamma = R_c{}^2\nabla^2 F + (1-v)F - \frac{\rho(1-v^2)R_c{}^2}{Y_0}\frac{\partial^2 F}{\partial t^2} + (1-v)\frac{D}{R_c}\left(\nabla^2 w + \frac{2}{R_c{}^2}w\right) - \frac{Y_0 h}{R_c}w \tag{2.3.4.4}$$

The first differential equation can be derived by substitution of $N_\phi^{'}$ and $N_\theta^{'}$ into the compatibility equation which leads to

$$\tan\phi\Gamma + \Gamma_{,\phi} = 0 \tag{2.3.4.5}$$

Without loss in generality, Γ can be set to zero and the first differential equation can be expressed as:

$$R_c{}^2\nabla^2 F + (1-v)F - \frac{\rho(1-v^2)R_c{}^2}{Y_0}\frac{\partial^2 F}{\partial t^2} + (1-v)\frac{D}{R_c}\left(\nabla^2 w + \frac{2}{R_c{}^2}w\right) - \frac{Y_0 h}{R_c}w = 0 \tag{2.3.4.6}$$

To obtain the second differential equation, first we combine Eq. (2.3.3.1) and Eq. (2.3.3.4) which results in the following expression for Q_ϕ

$$Q_\phi = \frac{\rho(1-v^2)}{R_c}\frac{D}{Y_0}\frac{\partial^2 u_\phi}{\partial t^2} - \frac{D}{R_c}\left(\nabla^2 w + \frac{2}{R_c{}^2}w\right)_{,\phi} \tag{2.3.4.7}$$

Furthermore, by substituting Eq. (2.3.4.7), Eq. (2.3.4.2) and Eq. (2.3.4.3) into Eq. (2.3.3.3), the second differential equation can be obtained:

$$\begin{aligned} &R_c{}^2\nabla^2 F + 2F - 2\frac{\rho(1+v)R_c{}^2}{Y_0}\frac{\partial^2 F}{\partial t^2} + \frac{R_c{}^2}{Y_0}\frac{h^2}{12}\rho(1+v)\frac{\partial^2\nabla^2 F}{\partial t^2} + DR_c\nabla^2\left(\nabla^2 w + \frac{2}{R_c{}^2}w\right) \\ &+2\frac{D}{R_c}\left(\nabla^2 w + \frac{2}{R_c{}^2}w\right) + \rho h R_c\frac{\partial^2 w}{\partial t^2} = R_c p_\zeta + \frac{2Y_0 d_{31}V_\zeta}{1-v} \end{aligned} \tag{2.3.4.8}$$

2.3.5. Harmonic Forced Vibration

The harmonic solution of the two system differential equations (i.e. Eq. (2.3.4.6) and EQ. (2.3.4.8)) is

$$\begin{Bmatrix} w \\ F \end{Bmatrix} = \mathrm{Re}\begin{Bmatrix} w^* e^{j\omega t} \\ F^* e^{j\omega t} \end{Bmatrix} \tag{2.3.5.1}$$

By eliminating F^* from the differential equations, the most general form of the forced vibration equation of a unimorph pMUT thin shell can be derived

$$\nabla^6 w^* + d_2 \nabla^4 w^* + d_3 \nabla^2 w^* + d_4 w^* = -d_5 R_c p_\zeta - d_5 \frac{2Y_0 d_{31} V_\zeta^*}{(1-v)} \tag{2.3.5.2}$$

where $d_2 = \frac{1}{R_c^{\,2}}\left[4+(1-v^2)\Omega^2\right]$, $d_3 = \frac{12(1-v^2)}{h^2 R_c^{\,2}}(1-\Omega^2) = \frac{hY_0}{R_c^{\,2} D}(1-\Omega^2)$,

$d_4 = \frac{hY_0}{DR_c^{\,4}}\left[2+(1+3v)\Omega^2+(v^2-1)\Omega^4\right]$, $d_5 = \frac{1}{DR_c^{\,3}}\left[(1-v)+(1-v^2)\Omega^2\right]$ and $\Omega^2 = \frac{\rho\omega^2 R_c^{\,2}}{Y_0}$

Equation (2.3.5.2) is a more general form of the differential equation for the forced vibration of a thin spherical shell obtained previously in [44], but with additional forcing terms due to the external pressure and the piezoelectric effect. The general solution for the free vibration of Eq. (2.3.5.2), i.e. p_ζ =0 and V_ζ^* =0, is

$$w_\alpha^* = A_\alpha P_{l_\alpha}(\cos\phi) + B_\alpha Q_{l_\alpha}(\cos\phi), \quad \alpha=1,2,3 \tag{2.3.5.3}$$

where P_l and Q_l are the Legendre functions of the first and second kind of order of l, respectively, where

$$l_\alpha = \left(\lambda_\alpha + \frac{1}{4}\right)^{1/2} - \frac{1}{2} \qquad \alpha = 1,2,3 \tag{2.3.5.4}$$

and λ_α are the roots of the equation

$$\begin{aligned} &\lambda^3 - \left[4+(1-v^2)\Omega^2\right]\lambda^2 + 12(1-v^2)\left(\frac{R_c}{h}\right)^2 (1-\Omega^2)\lambda \\ &-12(1-v^2)\left(\frac{R_c}{h}\right)^2 \left[2+(1+3v)\Omega^2+(v^2-1)\Omega^4\right] = 0 \end{aligned} \tag{2.3.5.5}$$

And the particular solution of Eq. (2.3.5.2) is

$$w_s^* = -\frac{(1-v)+(1-v^2)\Omega^2}{\left[2+(1+3v)\Omega^2+(v^2-1)\Omega^4\right]}\left(\frac{R_c}{h}\right)\frac{1}{Y_0}\left[R_c p_\zeta + \frac{2Y_0 d_{31} V_\zeta^*}{(1-v)}\right] \tag{2.3.5.6}$$

The final solution is the superposition of the general and particular solutions in the following form

$$w^* = w_1^* + w_2^* + w_3^* + w_s^* \tag{2.3.5.7}$$

2.3.6. Boundary Conditions

For a clamped PMUT shell, the boundary conditions are:

$$w^*\big|_{\phi=\phi_0} = 0\,,\ dw^*/d\phi\big|_{\phi=\phi_0} = 0 \text{ and } u_\phi^*\big|_{\phi=\phi_0} = 0, \qquad \left(\phi_0 = sin^{-1}\left[\frac{r}{R_c}\right]\right) \tag{2.3.6.1}$$

which result in the following system of three equations that can be solved for A_α[2]

$$\sum_{\alpha=1}^{3} A_\alpha P_{l_\alpha}(\cos\phi_0) = -w_s^* \tag{2.3.6.2}$$

$$\sum_{\alpha=1}^{3} A_\alpha \left(l_\alpha + 1\right)\left[\csc\phi_0 P_{l_\alpha+1}(\cos\phi_0) - \cot\phi_0 P_{l_\alpha}(\cos\phi_0)\right] = 0 \tag{2.3.6.3}$$

$$\sum_{\alpha=1}^{3} A_\alpha \frac{\left[\dfrac{\lambda_\alpha - 2}{12(1+v)}\left(\dfrac{h}{R_c}\right)^2 + 1\right]}{\left[-\lambda_\alpha + (1-v) + (1-v^2)\Omega^2\right]}\left(l_\alpha + 1\right)\left[\csc\phi_0 P_{l_\alpha+1}(\cos\phi_0) - \cot\phi_0 P_{l_\alpha}(\cos\phi_0)\right] = 0 \tag{2.3.6.4}$$

In order to derive Eq. (2.3.6.4), it is noted that u_ϕ can be expressed as a function of $F_{,\phi}$ as:

$$u_\phi = -(1+v)\frac{R_c}{Y_0 h} F_{,\phi} \tag{2.3.6.5}$$

and F can be related to w using Eq. (2.3.4.6) and Eq. (2.3.4.8).

The normalized first mode-shape function in terms of the angular position ϕ and center displacement versus frequency for a 2 µm thick curved AlN PMUT with 70 µm nominal radius and 1168 µm radius of curvature are plotted in Fig. 2.3.6.1a and Fig. 2.3.6.1b respectively for both simulation in COMSOL Multiphysics v4.3 and theoretical analyses data which show excellent agreement between the FEA simulation and the analytical model.

---

[2] Since $Q_{l_\alpha}(\cos(\phi = 0)) \to \infty$, B_α=0

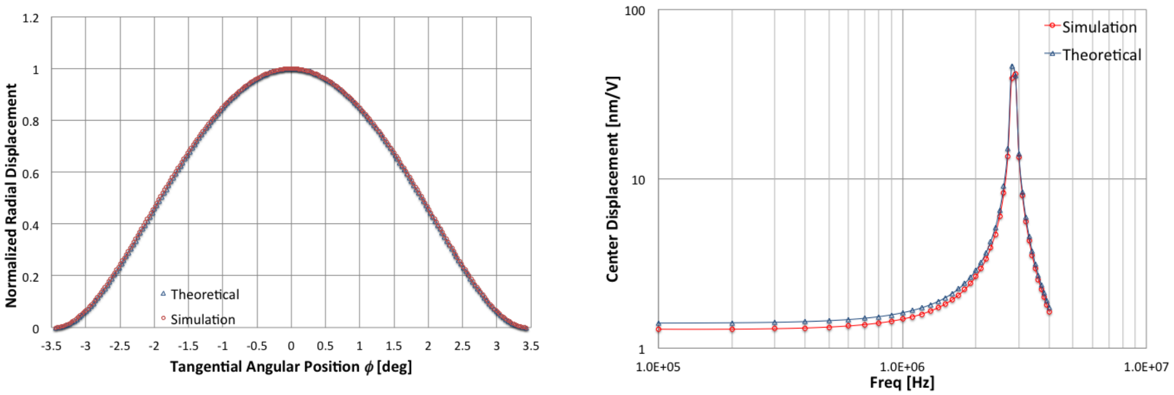

Fig. 2.3.6.1. Comparison of the mode-shape function as predicted by the developed model and simulated by FEM. The normalized radial displacement $w(\phi)$ for the curved pMUT is plotted as a function of the tangential angular position ϕ (a, left). Comparison of the model-predicted and simulated displacement at the center of the clamped curved pMUT per unit input voltage vs. the frequency of operation; (b, right). The curved pMUT is composed of a 2 µm thick AlN and the nominal radius r and the radius of curvature R_c are 70 µm and 1168 µm, respectively.

2.4. Circuit Model for Single-element Curved PMUT

This section demonstrates the derivations of the electromechanical parameters of a curved pMUT while the parameters for a flat pMUT are previously reported [36]. Figure 2.4.1 shows the 3D cross-sectional view of a curved pMUT. The transducer has a curved-shape diaphragm consisting of a piezoelectric layer sandwiched between two electrodes as both the structural layer and the transducer. By setting the input voltage and/or the incident acoustic pressure as independent variables, volumetric displacements and the electrical charges are derived analytically. Afterwards, the equivalent circuit parameters including the electrical capacitance, electromechanical transduction ratio, and mechanical admittance are extracted in the following sections.

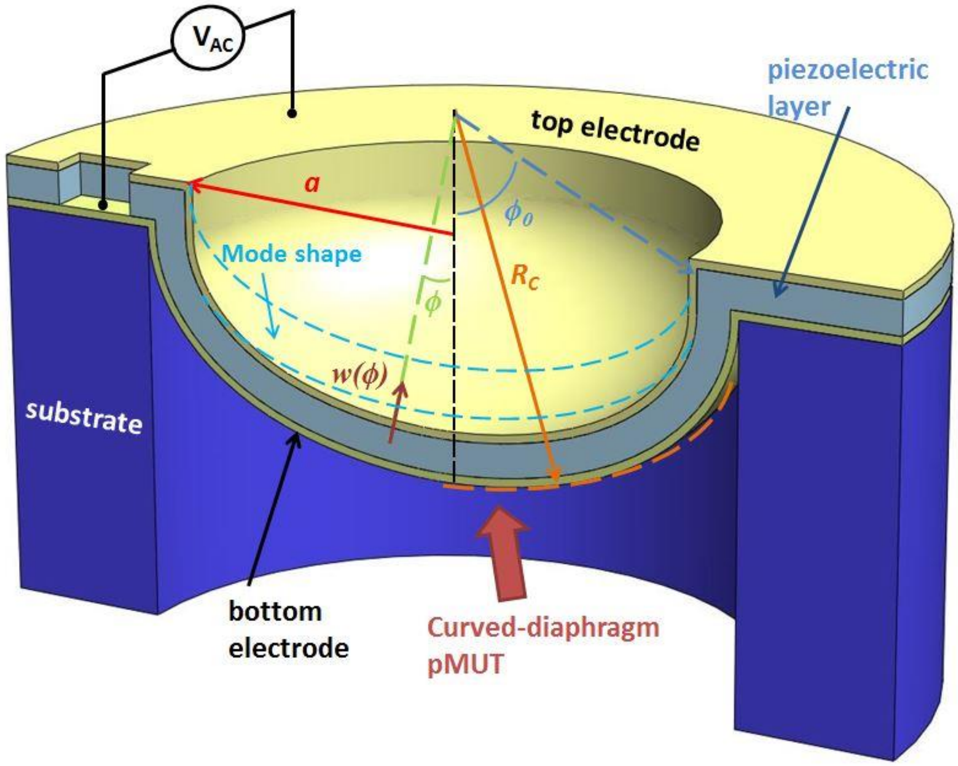

Fig. 2.4.1 3D schematic of a curved pMUT with nominal radius of *a* and radius of curvature of R_c.

2.4.1. Volumetric Displacement

In section 2.3. the equations for the harmonic deflections of a curved pMUT have been derived analytically in the time domain. The volumetric displacement is the amount of the volume that the transducer sweeps from its static equilibrium position to its maximum position. For a spherical-shape shell, the volumetric displacement can be calculated as [23-24]:

$$\bar{w} = R_c^2 \int_0^{2\pi} \int_0^{\phi_0} w(\phi) \sin\phi d\phi d\theta = 2\pi R_c^2 \int_0^{\phi_0} w(\phi) \sin\phi d\phi \tag{2.4.1.1}$$

where $w(\phi)$ is the radial displacement on the middle surface of the transducer, and ϕ_0 is the azimuthal angle at the edge of the spherical shell. The harmonic radial displacement depends on the transducer characteristics such as, geometry, material properties, boundary conditions, frequency of operation, and excitation parameters such as applied voltage and incident acoustic pressure. The summation of the homogenous solution, w_α (the natural vibration), and the particular solution or the forced vibration, w_s, can be rearranged from the 2.3.5 section as:

$$w^* = w_\alpha^* + w_s^* \tag{2.4.1.2}$$

$$w_\alpha^* = \sum_{\alpha=1}^{3} A_\alpha P_{l_\alpha}(\cos\phi) \tag{2.4.1.3}$$

$$w_s^* = \frac{(1-v)+(1-v^2)\Omega^2}{\left[2+(1+3v)\Omega^2+(v^2-1)\Omega^4\right]}\left(\frac{R_c^2}{hY_0}\right)\left[p_\zeta + \frac{2Y_0 d_{31} V_\xi}{R_c(1-v)}\right] \tag{2.4.1.4}$$

The value of A_α can be derived from the particular boundary conditions. By applying the clamped boundary conditions, the following equation can be solved for A_α.

$$\begin{bmatrix} P_{l_1}(\cos\phi_0) & P_{l_2}(\cos\phi_0) & P_{l_3}(\cos\phi_0) \\ f(l_1) & f(l_2) & f(l_3) \\ g(\lambda_1)f(l_1) & g(\lambda_2)f(l_2) & g(\lambda_3)f(l_3) \end{bmatrix} \begin{bmatrix} A_1 \\ A_2 \\ A_3 \end{bmatrix} = \begin{bmatrix} -w_s^* \\ 0 \\ 0 \end{bmatrix} \tag{2.4.1.5}$$

where *f* and *g* are functions expressed in Table I along with the other parameters, and λ_α are the solutions of the characteristic equation, Eq. (2.2.5.5).

Table 2.4.1.1. List of the Parameters and Functions

Parameter	Expression
$f(x)$	$(x+1)[\csc\phi_0 P_{x+1}(\cos\phi_0) - \cot\phi_0 P_x(\cos\phi_0)]$
$g(x)$	$\frac{\left[(x-2)/12(1+v)\left(h/R_c\right)^2+1\right]}{\left[-x+(1-v)+(1-v^2)\Omega^2\right]}$
l_α	$\left(\lambda_\alpha+\frac{1}{4}\right)^{1/2}-\frac{1}{2} \quad \alpha=1,2,3$
a_{1j}	$P_{l_j}(\cos\phi_0)$
a_{2j}	$f(l_j)$
a_{3j}	$g(\lambda_j)f(l_j)$
m_1	$(a_{22}a_{33}-a_{32}a_{23})$
m_2	$(a_{21}a_{33}-a_{31}a_{23})$
m_3	$(a_{21}a_{32}-a_{31}a_{22})$
n	$a_{11}m_1-a_{12}m_2+a_{13}m_3$

Finally, the displacement equation can be rearranged for convenience in the integration:

$$w^{*} = \left[1 + A_{1}^{'}(\omega,\phi_{0})P_{l_{1}}(\cos\phi) + A_{2}^{'}(\omega,\phi_{0})P_{l_{2}}(\cos\phi) + A_{3}^{'}(\omega,\phi_{0})P_{l_{3}}(\cos\phi)\right] \times \left[p_{\zeta} + \frac{2Y_{0}d_{31}V_{\zeta}}{R_{c}(1-\nu)}\right] b(\omega) \quad (2.4.1.6)$$

where A_i' and $b(\omega)$ are functions of the operation frequency, the material properties, and the geometry of the transducer, $b(\omega)$ is a frequency gain term as derived below, and A_i' depends on the frequency as well as the boundary conditions as the mode shape or the shaping function of the vibrating transducer.

$$b(\omega) = \frac{(1-\nu) + (1-\nu^{2})\Omega^{2}}{\left[2 + (1+3\nu)\Omega^{2} + (\nu^{2}-1)\Omega^{4}\right]}\left(\frac{R_{c}^{2}}{hY_{0}}\right) \quad (2.4.1.7)$$

$$A_{j}^{'} = (-1)^{j} m_{j} / n \quad (2.4.1.8)$$

By integrating Eq. (2.4.1.6) over the surface area of the shell using Eq. (2.4.1.1), the total volumetric displacement is derived as:

$$\overline{w}^{*} = 2\pi R_{c}^{2}\left[\left(1-\cos\phi_{0}\right) + A_{1}^{'}H(l_{1}) + A_{2}^{'}H(l_{2}) + A_{3}^{'}H(l_{3})\right]\left[p_{\zeta} + \frac{2Y_{0}d_{31}V_{\zeta}}{R_{c}(1-\nu)}\right] b(\omega) \quad (2.4.1.9)$$

$$H(l_{\alpha}) = \left[P_{l_{\alpha}-1}(\cos\phi_{0}) - P_{l_{\alpha}+1}(\cos\phi_{0})\right] / \left[1 + 2l_{\alpha}\right] \quad (2.4.1.10)$$

Upon rearrangement, Eq. (2.4.1.9) can be further represented into the system equations as functions of p_ζ and V_ζ:

$$\overline{w}^{*} = Y_{m} p_{\zeta} + b_{me} V_{\zeta} \quad (2.4.1.11)$$

$$Y_{m} = 2\pi R_{c}^{2} X(\omega) \quad (2.4.1.12)$$

$$b_{me} = \left[4\pi Y_{0} d_{31} R_{c} / (1-\nu)\right] X(\omega) \quad (2.4.1.13)$$

$$X(\omega) = \left[\left(1-\cos\phi_{0}\right) + A_{1}^{'}H(l_{1}) + A_{2}^{'}H(l_{2}) + A_{3}^{'}H(l_{3})\right] b(\omega) \quad (2.4.1.14)$$

where Y_m is the mechanical admittance and b_{me} is the electrical to mechanical transduction coefficient.

2.4.2. Electrical Responses

The electric displacement field in the radial direction for a spherical piezoelectric shell can be written as the following form:

$$D_{\zeta} = d_{31}(\sigma_{\phi\phi} + \sigma_{\theta\theta}) + \varepsilon_{\zeta} E_{\zeta} \quad (2.4.2.1)$$

where $\sigma_{\theta\theta}$ and $\sigma_{\phi\phi}$ are the transverse stresses in the θ and ϕ directions respectively, ε_ζ is the permittivity, and E_ζ is the applied electric field in the radial direction. By expressing $\sigma_{\theta\theta}$ and $\sigma_{\phi\phi}$ in terms of strains using the piezoelectric constitutive equations, followed by the substitution of the strains by the displacements in the spherical coordinate system, the radial electrical displacement can be derived as [23-24]:

$$D_{\zeta} = \frac{Y_0 d_{31}}{(1-v)R_c}\left(\cot\phi u_{\phi} + \frac{\partial u_{\phi}}{\partial \phi} + 2w\right) + \varepsilon_{\zeta}(1-k_e{}^2)E_{\zeta} \qquad (2.4.2.2)$$

where $k_e{}^2 = \frac{2Y_0^{'}\left(d_{31}^{'}\right)^2}{(1+v)\varepsilon_{\zeta}}$ is the electromechanical coupling factor.

In order to calculate the total electric charge, D_{ζ} must be integrated over the surface area of the transducer (i.e. $Q = \oint_A D_{\zeta} dA$). By integrating Eq. (2.4.2.2), the second system equation can be derived:

$$\begin{aligned} Q = {} & 4\pi Y_0^{'} d_{31}^{'} R_c \left[\left(1-\cos\phi_0\right) + A_1^{'}H(l_1) + A_2^{'}H(l_2) + A_3^{'}H(l_3)\right]\left[p_{\zeta} + \frac{2Y_0 d_{31} V_{\zeta}}{R_c(1-v)}\right]b(\omega) \\ & + \left[2\pi\left(1-\cos\phi_0\right)R_c^2 \varepsilon_{\zeta}(1-k_e{}^2)/h\right]V_{\zeta} \end{aligned} \qquad (2.4.2.3)$$

where $Y_0{}'$ is the modified Young's modulus and $d_{31}{}'$ is the modified transverse piezoelectric strain constant as: $Y_0^{'} \equiv \frac{Y_0}{1-v^2}$, and $d_{31}^{'} \equiv d_{31}(1+v)$.

After further rearrangements, the system equations for electrical charges are represented as functions of p_{ζ} and V_{ζ}:

$$Q = b_{em} p_{\zeta} + C_{em} V_{\zeta} + C_0 V_{\zeta} \qquad (2.4.2.4)$$

$$b_{em} = \left[4\pi Y_0 d_{31} R_c / (1-v)\right] X(\omega) \qquad (2.4.2.5)$$

$$C_{em} = \left[(8\pi Y_0^2 d_{31}^2)/(1-v)^2\right] X(\omega) \qquad (2.4.2.6)$$

$$C_0 = 2\pi\left(1-\cos\phi_0\right) R_c^2 \varepsilon_{\zeta}(1-k_e{}^2)/h \qquad (2.4.2.7)$$

where b_{em} is the mechanical to electrical transduction coefficient, C_{em} is the induced capacitance due to mechanical motion, and C_0 is the blocked capacitance. It is important to note that b_{me} and b_{em} turned out to be equal ($b_{me} = b_{em} = b_t$), thus, the reciprocity of the system is verified and an equivalent circuit representation of such transducers is appropriate.

2.4.3. Equivalent Electrical Circuit

Solving the system equations (Eqs. (2.4.1.11) and (2.4.2.4)) with explicit expressions for the equivalent circuit parameters, the equivalent circuit model for the transducer can be derived to relate the electrical, mechanical, and acoustical domains [23, 24, & 64]. The equivalent circuit model shown in Fig. 2.4.3.1 is one way to represent the transducer model, where electrical and mechano-acoustical domains interact with each another through a transformer. In the circuit representation, Z_e is the electrical feedthrough impedance, Z_m is the mechanical impedance, Z_a is the acoustical impedance which will be defined in 2.5, and η is the electromechanical transformer ratio defined as:

$$Z_e = \frac{1}{j\omega C_0},\ Z_m = \frac{1}{j\omega Y_m},\ \text{and}\ \eta = \frac{b_t}{Y_m} \tag{2.4.3.1}$$

In order to evaluate the transducer response using the equivalent circuit model presented in Fig. 2.4.3.1, one can: 1) derive the value of C_0 from Eq. (2.4.2.7), which is a constant and is independent of the operation frequency; 2) calculate Z_m from Eq. (2.4.3.1) by substituting for the mechanical admittance, Y_m, from Eq. (2.4.1.12); 3) calculate the transformer ratio η, which also is a constant, from Eq. (2.4.3.1) by substituting for Y_m and b_t from Eq. (2.4.1.12) and Eq. (2.4.1.13) respectively; and 4) substitute for the acoustical impedance Z_a from one of the equations presented in the following sections, according to the medium of operation.

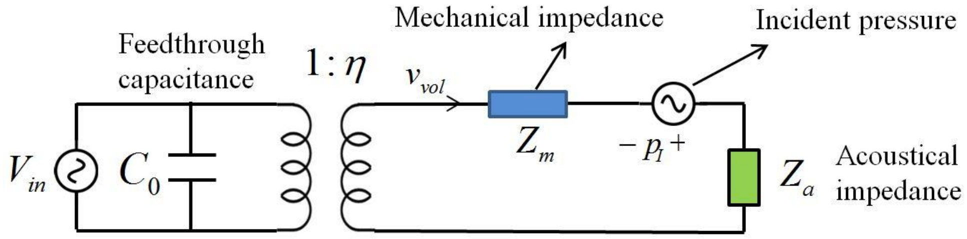

Fig. 2.4.3.1. The equivalent circuit model of the transducer.

2.4.4. Equivalent Circuit Results and Discussions

The analytical analysis is compared with FEM simulation results using a specific example: an air-backed, 2-µm thick aluminum nitride curved pMUT with 80 µm in nominal radius, 880 µm in radius of curvature, and either air or water as the front side media. COMSOL Multiphysics v4.3 (acoustic-piezoelectric interaction) is used to simulate the frequency response of the transducer, while the theoretical analysis is coded in MATLAB R2014b (The MathWorks Inc., Natick, MA, USA).

The specific material properties of the single-element curved pMUT are listed in Table 4.3.1 The derived circuit explicit expressions can be used to extract the lumped-element parameters for any given pMUTin the case of the curved pMUT example, we have C_0 = 0.864 pF and η = 2597 Pa/V. On the other hand, Z_m, which is a function of the geometry, boundary conditions, material properties, and the frequency of operation of the pMUT, can be approximated to the first order as a series LC for the ideal case where L_m represents the pMUT mass and C_m represents its compliance. Both L_m and C_m can be estimated from the Z_m (or Y_m) asymptotic values at high and low frequencies, respectively. For the curved pMUT example, $L_m = 6.073 \times 10^5$ Pa.s/m^3 and $C_m = 4.407 \times 10^{-21}$ m^3.s/Pa, and their transferred values to the electrical domain are $L_{m\_el} = L_m/\eta^2$ = 90 mH and $C_{m\_el} = C_m\,\eta^2$ =29.7 fF. The acoustic impedance, Z_a is also calculated using Eq. (4.2.1.2) for air and water loadings. Figure 2.4.4.1 shows the volumetric displacement frequency responses in air and water with good consistency between the theory model and FEA simulation for the example model. One essential advantage of the MEMS ultrasonic transducers is their low mechanical impedance (i.e. Z_m) which can be matched well to the acoustic impedance of the medium to eliminate the necessity of using a matching layer (the expressions used for acoustic impedance is shown in the following sections). It is observed in Fig. 2.4.4.1 that the -3dB bandwidth in water for this prototype transducer is estimated as 134 and 130 kHz while the resonant frequency is predicted as 1.04 and 1.0 MHz from the proposed model and simulation results, respectively.

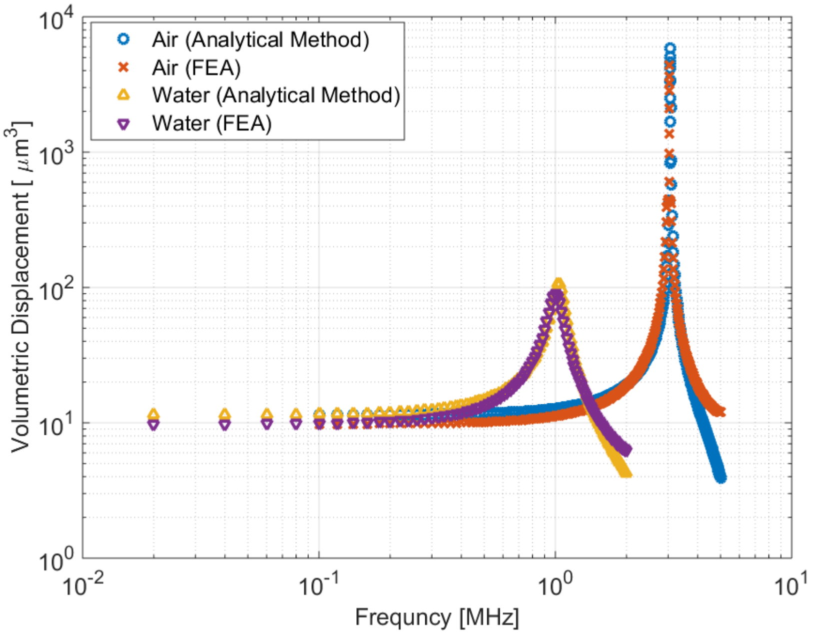

Fig. 2.4.4.1. Volumetric displacement responses of a 2-µm thick AlN pMUT with 80µm nominal radius and 880µm radius of curvature in air and water.

Figures 2.4.4.2(a) and (b) show the comparison between the theory and the simulation results of the input impedance in air and water, respectively. It can be seen that the theory and the simulation results have good consistency in terms of the overall trend, value, and predictions of the resonant and anti-resonant frequencies.

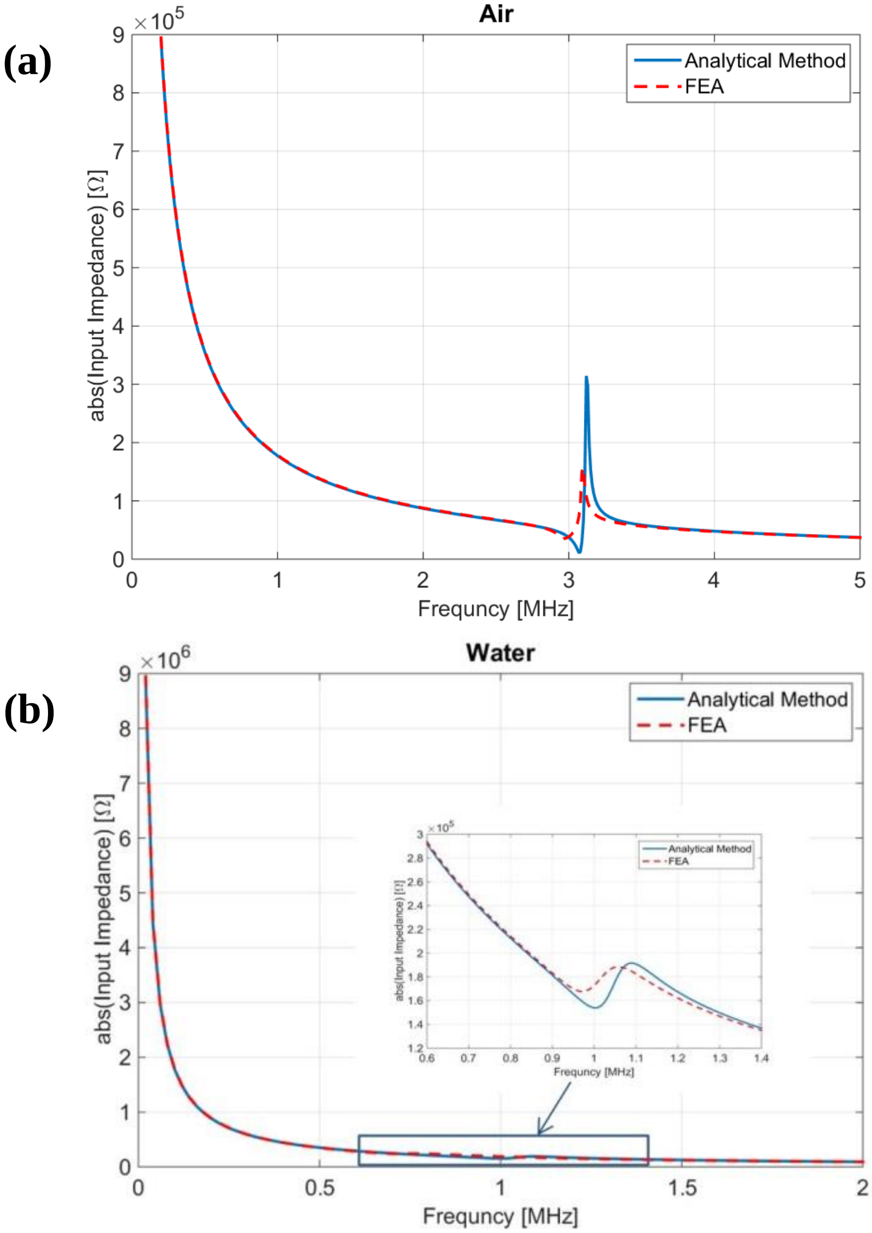

Fig. 2.4.4.2. Comparison between the theoretical and simulated values of the input impedance of the example transducer in (a) air and (b) water.

The electromechanical coupling factor (k_{eff}^2) is a good indicator for the electromechanical conversion efficiency. For piezoelectric transducers, the maximum possible value depends on the material properties and the operation mode. In the case of curved pMUTs, the expression for maximum k_{eff}^2 is the same as k_e^2 and for a clamped AlN diaphragm operating in flexural mode is about 5.5% [23-24]. The actual value of k_{eff}^2 can be calculated from the input impedance versus frequency curves of the transducer operating in vacuum using [65]:

$$k_{eff}{}^2 = \frac{f_a{}^2 - f_r{}^2}{f_r{}^2} \qquad (2.4.4.1)$$

where f_r and f_a are the resonant and anti-resonant frequencies respectively.

Figure 2.4.4.3 shows the electromechanical coupling factor versus the radius of curvature for curved AlN pMUTs with identical thicknesses (2µm) and nominal radii (80 µm). It is observed from both theory and simulation that as the radius of curvature increases, the electrochemical coupling factor increases to reach a maximum value and decreases afterwards (Fig. 2.4.4.3).

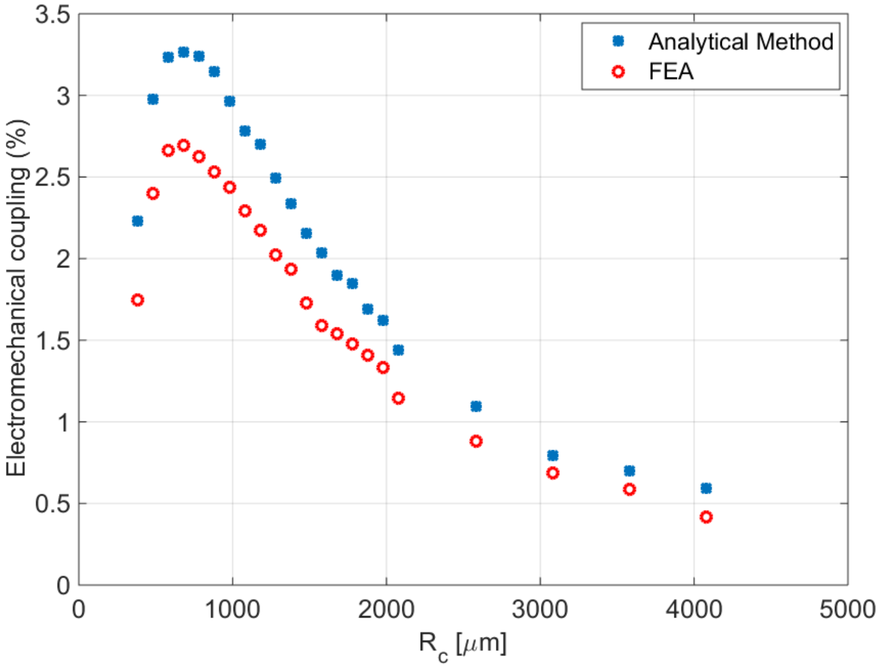

Fig. 2.4.4.3. Electromechanical coupling factor versus the radius of curvature of a 2-µm thick AlN pMUT with 80 µm nominal radius.

The maximum electromechanical coupling factor for this specific curved pMUT is predicted as 3.3%, which shows curved pMUT can potentially reach 60% of material limit of 5.5%.

This result shows that a curved pMUT is much more responsive than a conventional flat AlN pMUT (maximum electromechanical coupling factor is predicted to be 0.5% [23-24]). The corresponding optimum value for the radius of curvature is 680 µm in this case. Using such analysis, we can predict the optimum design for curved pMUT, based on the desired operation frequency and application. The displacement per input voltage is proportional to the piezo-induced force divided by the stiffness of the diaphragm. Intuitively, the curved diaphragm can convert part of the lateral piezoelectric deformation into vertical displacement, causing the electromechanical conversion efficiency to improve as the radius of curvature of the diaphragm reduces from infinity (flat) to smaller values. This effect is countered by the fact that as the radius of curvature decreases, the stiffness of the diaphragm increases. The net effect of these competing phenomena results an optimal radius of curvature where the maximum electromechanical conversion efficiency is achieved, as shown in Figure 2.4.4.3.

2.5. Acoustic Radiation and Acoustic Impedance for Single-element Curved PMUT

In order to model the acoustic radiation patterns of the transducers, the acoustic impedance and radiation for diaphragms operating in the flextentional mode should be derived. The mode shape and the displacement function of the transducer are first derived from the modal analysis of clamped piezoelectric elastic shells with spherical-shape diaphragms. The normalized mode shape of the transducer is approximated by a sixth order polynomial as:

$$\frac{w_0(r')}{w_{\max}} = \left(-0.30\left(\frac{r'}{a}\right)^6 + 0.34\left(\frac{r'}{a}\right)^5 + 1.13\left(\frac{r'}{a}\right)^4 - 0.10\left(\frac{r'}{a}\right)^3 - 2.04\left(\frac{r'}{a}\right)^2 - 0.02\left(\frac{r'}{a}\right) + 1 \right) \tag{2.5.1}$$

where a is the nominal radius of the transducer and r' is the radial distance from the center of the transducer. Eq. (2.5.1) is a good approximation for the first mode of operation for clamped shells where $h<<a<<R_c$. Here, a sixth order polynomial is used to estimate the clamped spherical shell first mode shape since the equation of motion of such a transducer was shown in [23-24] to be a sixth order differential equation.

The geometrical parameters as well as the mode shape and stress profile of a spherically-curved clamped diaphragm is shown in Fig. 2.5.1. To evaluate the acoustic radiation, it is assumed that the acoustic radiation from each individual point on the transducer surface will initially follow the geometrical path normal to the surface of the transducer at that point to the plane of the baffle [5]. Thus, we can find the equivalent displacement at the plane of the baffle using the ray optic methods (Fig. 2.5.1).

$$w_{z\_eq}(r') = w_0(r') \frac{(R_c - g)^2}{(R_c - g)^2 + r'^2} \times \frac{R_c}{\sqrt{R_c - a^2}} \times \exp(-kj(R_c - \sqrt{(R_c - g)^2 + r'^2}) \tag{2.5.2}$$

where g is the distance from the transducer center from the baffle plane, and k is the wave number. The amplitude modulation comes from the geometrical optics and energy conservation principals, while the exponential term comes from the phase delay of each point on the baffle plane, which is associated with the beam path distance from the transducer surface.

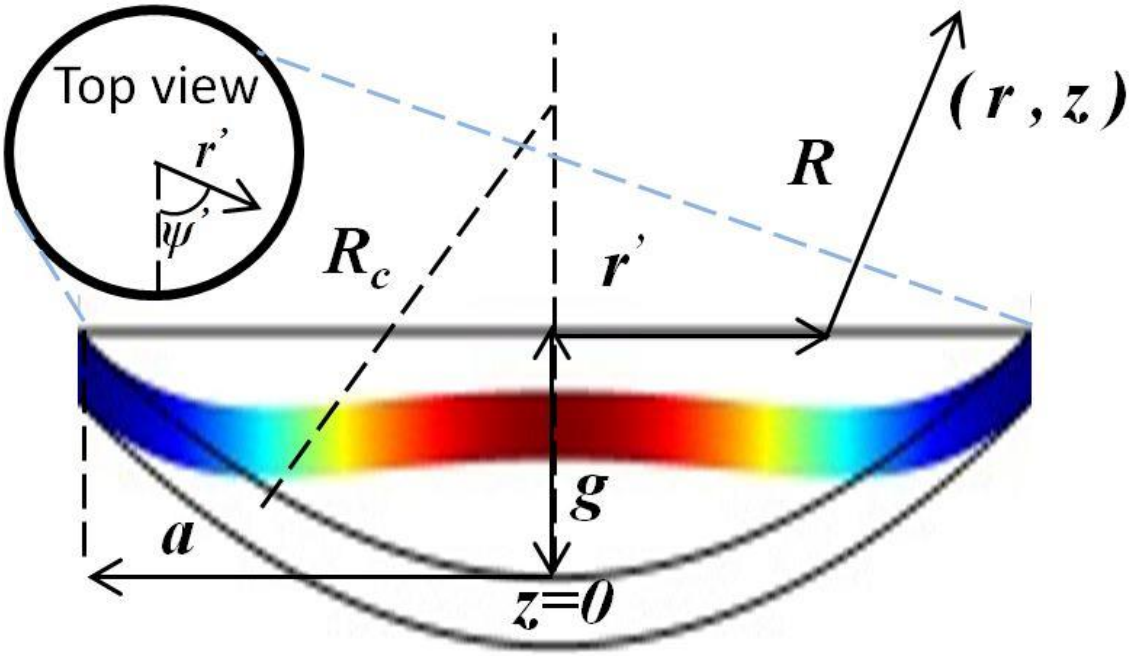

Fig. 2.5.1. The 2D cross-sectional view of a curved pMUT showing the geometrical parameters and operation mode.

The theory of a moving transducer in a flat rigid baffle is utilized in this section. We also assume that the medium of interest is an inviscid fluid, so that we have no shear stress, and the pressure is isotropic, equal to the negative of the longitudinal stresses, and is proportional to velocity potential [5]. Using the above assumptions, the acoustic pressure at an arbitrary point (r,z) in the medium is derived as [4, 5]:

$$p_s(r,z) = -\frac{\rho\omega^2}{2\pi}\iint \frac{u_{z\_eq}(r')}{R}e^{-jkR}r'dr'd\psi' \tag{2.5.3}$$

where ρ is the medium density and R is the distance from an arbitrary point on the transducer (r',ψ') to (r,z). Furthermore, the acoustic impedance or the acoustic load on the transducer is calculated using the power-based definition of radiation impedance of transducers with non-uniform velocity distribution [4]:

$$Z_s = \frac{1}{v_{vol\_eq}v_{vol\_eq}^{*}}\iint p_s(r',g)u_{z\_eq}(r')^{*}r'dr'd\psi' \tag{2.5.4}$$

where $u_{z\_eq}(r') = j\omega \times w_{z\_eq}(r')$ is the equivalent transducer velocity at the plane of the baffle and v_{vol_eq} is the equivalent volumetric velocity calculated by integrating u_{z_eq} over the projected transducer area at the plane of the baffle.

The pressure field of a curved pMUT with a spherical-shape diaphragm of 100 μm in nominal radius, 2 μm in thickness, and 700 μm in radius of curvature operating at its resonant frequency of 1 MHz in water is plotted in Fig. 2.5.2. In Figs. 2.5.2 & 2.5.3, the following Fresnel approximation, which is valid for $z^2 >> a^2$, was used to simplify Eq. (2.5.3) by integrating over ψ' [5]:

$$p_s(r,z) = -\rho\omega^2 \frac{-e^{-jk(z+r^2/2z)}}{\sqrt{(z-g)^2+r^2}} \int u_{z\_eq}(r') J_0\left(\frac{krr'}{z}\right) e^{(-jkr'^2/2)(1/z-1/R_c)} r'dr' \qquad (2.5.5)$$

It is found that in this example model, at about 0.3 of a wavelength away from the center of the transducer in the lateral and vertical directions, the acoustic pressure drops to about 20% of the highest pressure (at the center of the diaphragm). In this case, the dimensions of the transducer is much smaller than the wavelength ($ka << 1$) such that the transducer is approximately realized as a point source with spherical acoustic radiation field in the far field (where $\lambda z/a^2 > 1$ [5]).

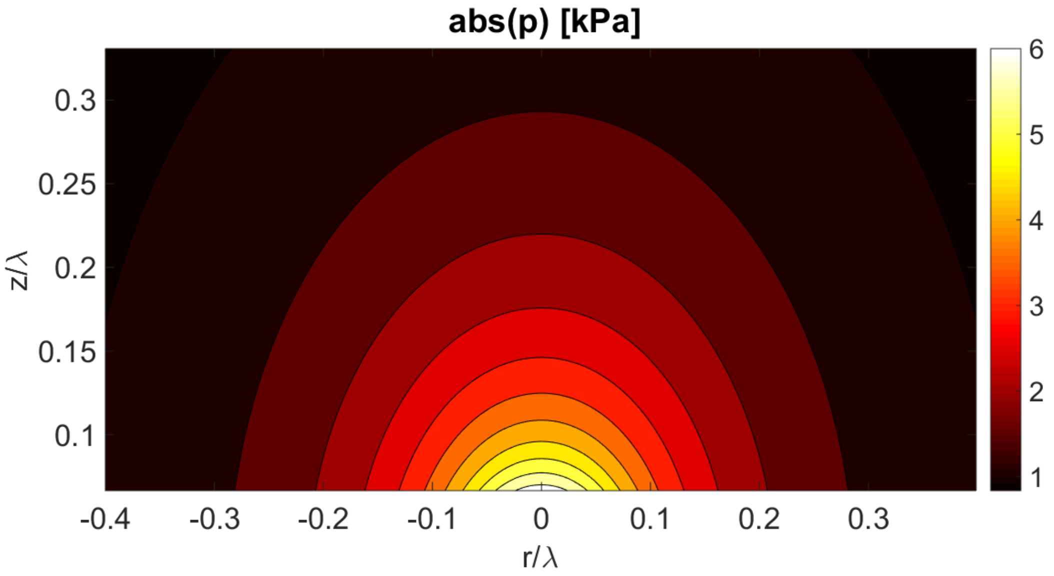

Fig. 2.5.2 Pressure field of a curved pMUT.

Finite element simulation results from COMSOL Multiphysics v.4.3 (Acoustic-Piezoelectric Interaction module) are used for further comparisons. Figures 2.5.3a.2.5.3c show the analytical method and FEA simulation results for the absolute, imaginary, and real axial pressure, respectively, as a function of the normalized axial distance of the model curved pMUT driven at 1 MHz with 1 V_{ac}. Figure 2.5.3d shows the lateral pressure of the model curved pMUT under the same driving conditions as a function of the normalized lateral distance at $z/\lambda=0.27$. The results show very good consistency between the analytical model and the FEA simulation results. The small divergence of the real pressure for $z/\lambda<0.25$ in Fig. 2.5.3c is due to the Fresnel approximation which is only valid for $z^2>>a^2$. The consistency of the pressure value and radiation profile between theory and finite element simulation reveals that the acoustic pressure field of a curved pMUT can be well. predicted by the analytical model and can be further used in combination with the electromechanical equivalent circuit model.

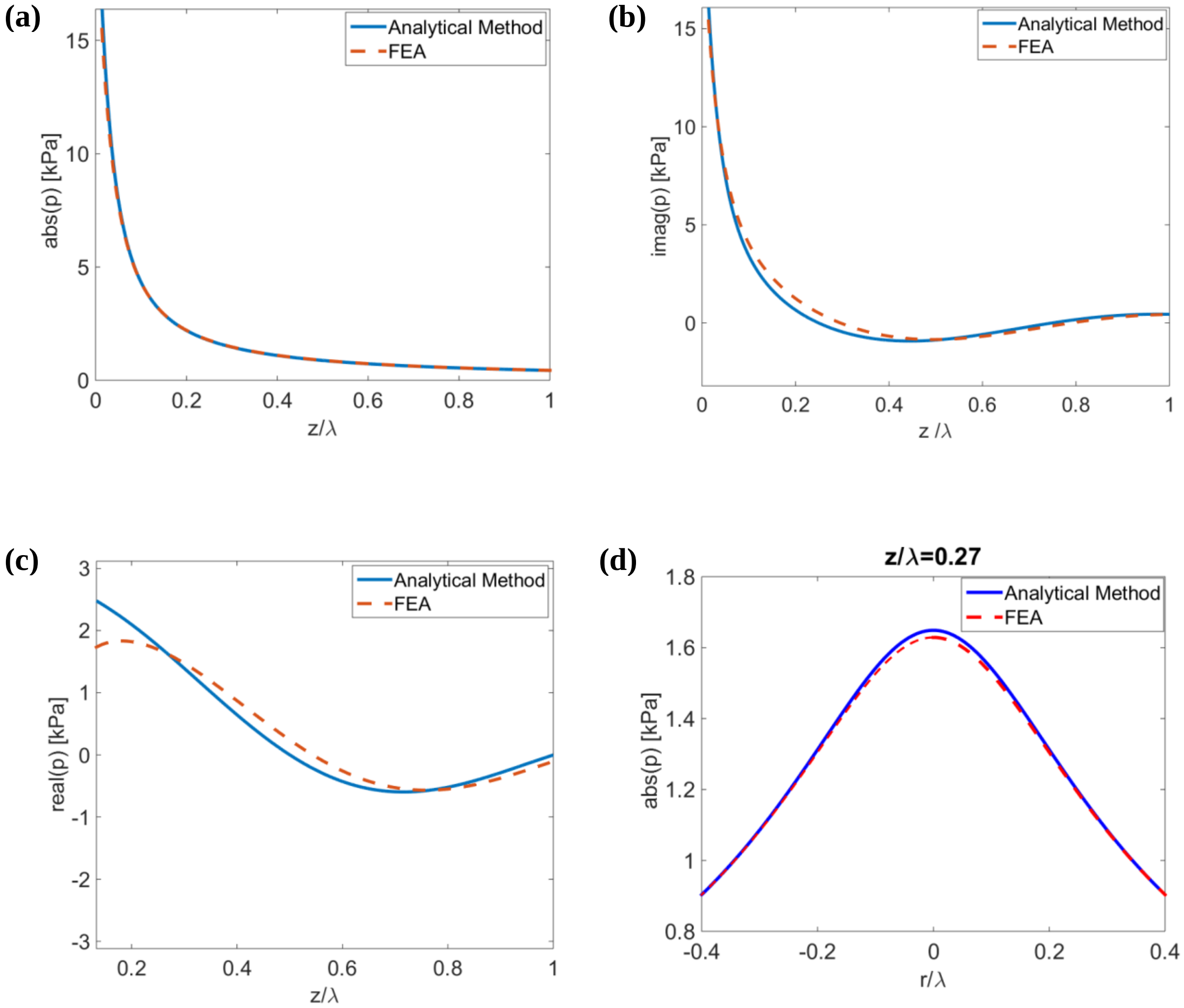

Fig. 2.5.3. Comparison between the theoretical model and COMSOL FEA model of the (a) absolute, (b) imaginary, and (c) real axial acoustic pressure of the model spherically curved pMUT as a function of the normalized axial distance when the pMUT is driven with 1 V_{ac} input voltage at 1 MHz; (d) shows the comparison of the lateral acoustic pressure between the analytical model and COMSOL FEA model at *z/λ=0.27*.

The axial and lateral pressure profiles of a curved pMUT that is 100 µm in nominal radius, 2 µm in thickness, and 700 µm in radius of curvature operating at its resonant frequency of 1 MHz in water are compared with a flat pMUT with the similar lateral geometry and resonant frequency when both pMUTs are driven with 1 V_{ac}. The flat pMUT has 70% areal top electrode coverage, with silicon and aluminum nitride thicknesses of 4.4 µm and 1 µm, respectively. The piezoelectric layer for both transducers is aluminum nitride. It is noted that a flat pMUT requires a structural layer like silicon in order to form a bending moment about the diaphragm neutral axis due to the stress gradient in the whole stack. Figure 2.5.4a shows the comparison of axial pressures between the curved and flat transducers, and Fig. 2.5.4b shows the lateral pressures. It can be seen that the acoustic pressure at *r*=0 is approximately 2.7 times higher for the curved pMUT than that of a flat pMUT.

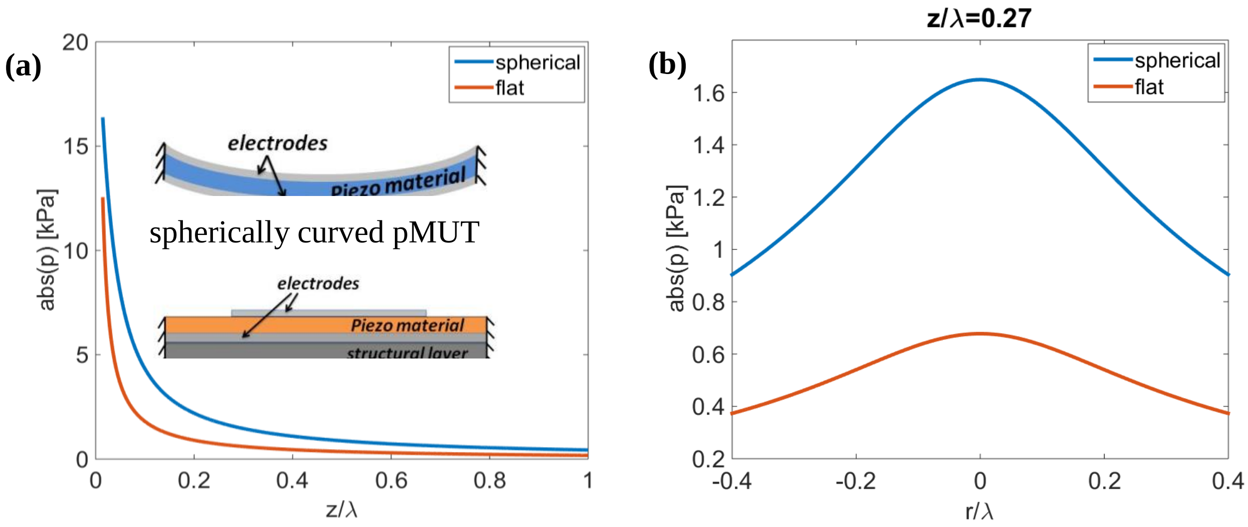

Fig. 2.5.4 Comparison between the (a) axial and (b) lateral pressure of a spherically curved pMUT and a flat pMUT with the same diameter and resonant frequency when both driven with the same input voltage ($1V_{ac}$) at their resonant frequency of 1 MHz, showing superior performance of the curved device.

2.6. Fabrication

2.6.1. Process Flow

The fabrication process flow begins with silicon wet etching using HNA (hydrofluoric, nitric, acetic acids) to form the curved device structural base using a 1.2 µm low stress LPCVD nitride as a hard mask (Fig 2.6.1a). A 1.1 µm thick LPCVD low temperature oxide (LTO) is then grown to form the backside etching stop layer as shown in Fig. 2.6.1b, this is followed by the sputtering of the active stack of Mo/AlN/Mo with thicknesses of 100 nm, 2 µm and 100 nm, respectively. The Molybdenum layers constitute the top and bottom electrodes, while the AlN layer serves the purpose of the piezoelectric and main structural layer, simultaneously.

Figure 2.6.1c shows the via opening to the bottom electrode, which is made by SF_6 plasma etching of the top Mo and followed by a combination of plasma dry etching in chlorine based gases and MF.319 developer wet etching of AlN.

The last process step is to release the diaphragm using backside deep reactive ion etching (DRIE), with the nominal diameter of the released membrane defined by the backside etch opening process, as illustrated in Fig. 2.6.1d. In order to target medical imaging frequency for deep structures (e.g. kidneys, liver, etc.), curved pMUTs with controlled radii of curvature within 400~2000 µm have been fabricated with nominal diameters of 120 µm to 190 µm in the prototype devices for characterizations and investigations. These yield devices with resonant frequencies between 1 to 4 MHz in water.

2.6.2. Fabrication Results

An SEM cross-sectional view micrograph showing a curved pMUT is shown in Fig. 2.6.2a, where the cavity opening is 320µm in diameter and the curved pMUT diaphragm is 190µm in diameter. Figure 2.6.2b is the close-up view of Fig. 2.6.2a near the anchor area where the undercut phenomenon during the DRIE process is clearly observed.

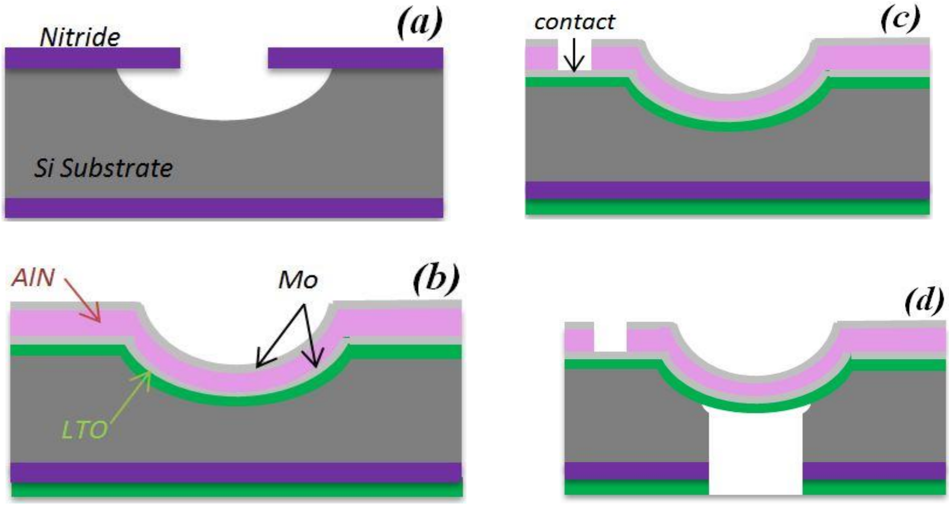

Fig. 2.6.1. Process flow for the curved pMUT: (a) silicon wet etching using nitride as the mask for cavity formation; (b) LTO deposition as the stop layer and Mo/ALN/Mo deposition as the piezoelectric structure layer; (c) contact opening; (d) backside DRIE silicon etching.

Figure 2.6.2c is a high resolution SEM photo revealing that the desirable polarization direction of AlN has been achieved to be perpendicular to the curvature of the diaphragm. Figure 2.6.3 is a top-view optical image of an array of the same curved pMUT shown in Fig 2.6.2a with the reflection of light from the smooth concave surface of the curved pMUT and the via contact opening to the bottom electrode.

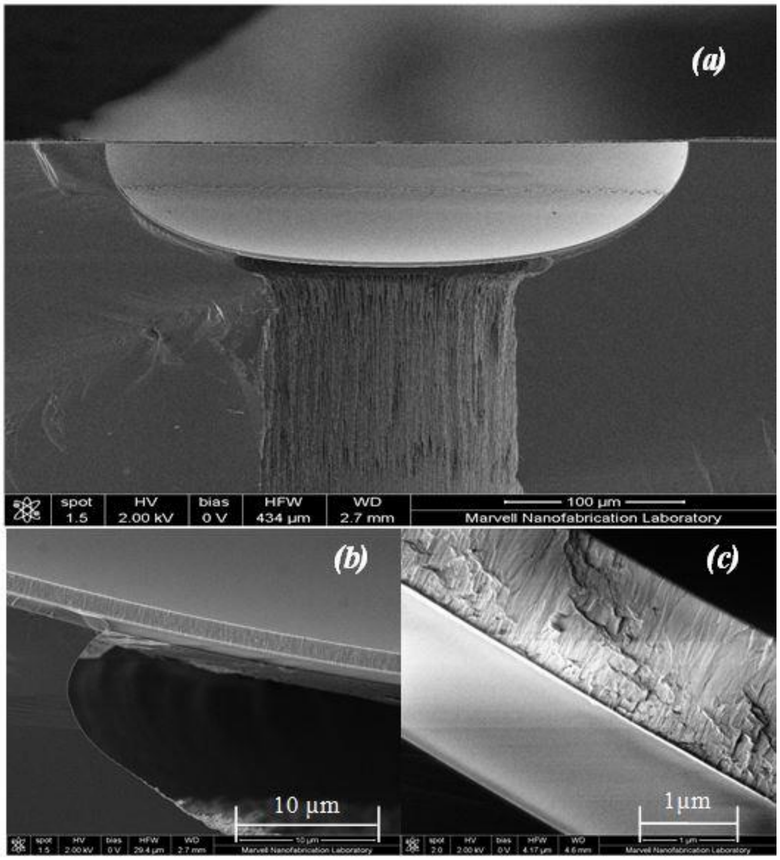

Fig. 2.6.2. SEM micrographs: (a) a cleaved device showing the cross sectional view of a fabricated pMUT; (b) close-up view of (a) showing the undercut due to excessive DRIE etching; (c) the close view SEM photo showing that the polarization direction of the AlN crystalline structure is perpendicular to the curvature of the diaphragm.

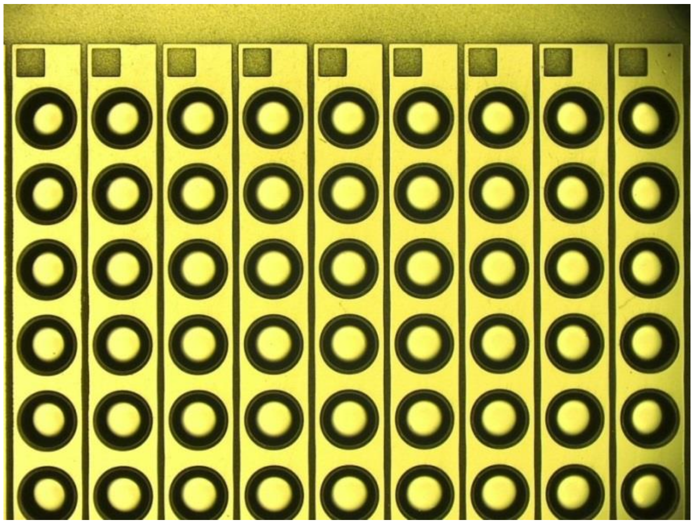

Fig. 2.6.3. a top view optical image of an array of curved pMUTs.

2.7. Results and Discussions

In order to investigate the effect of the curvature of the structure, both an analytical model and finite element analyses using COMSOL Multiphysics have been built with good consistency. The solid curve in Fig. 2.7.1b is the predicted DC displacement of a curved pMUT with 2-µm thick AlN, 140µm in nominal diameter with respect to different radii of curvature. It is noted that the DC displacement starts to increase as the radius of curvature increases; reaches a maximum; and starts to decrease with further increase of the curvature. Clearly, a curved pMUT has a higher resonant frequency than a flat pMUT with the same nominal diameter. As a result the curved pMUT will have a higher volumetric velocity (the product of higher frequency and higher displacement) than a flat pMUT, and so it will generate a higher acoustic pressure. The symbols in Fig. 2.7.1b are the experimental data measured from the prototype devices with different radii of curvature. The data from a flat pMUT is from a similar process run with 1 µm-thick AlN, 3 µm-thick silicon as the structural layer and 70% top electrode coverage. The experimental results for curved pMUTs show good consistency with the simulation results both in terms of the center displacement and resonant frequency. It is noted that more than one order of magnitude higher DC displacement is achieved from the curved pMUT as compared with the flat pMUT.

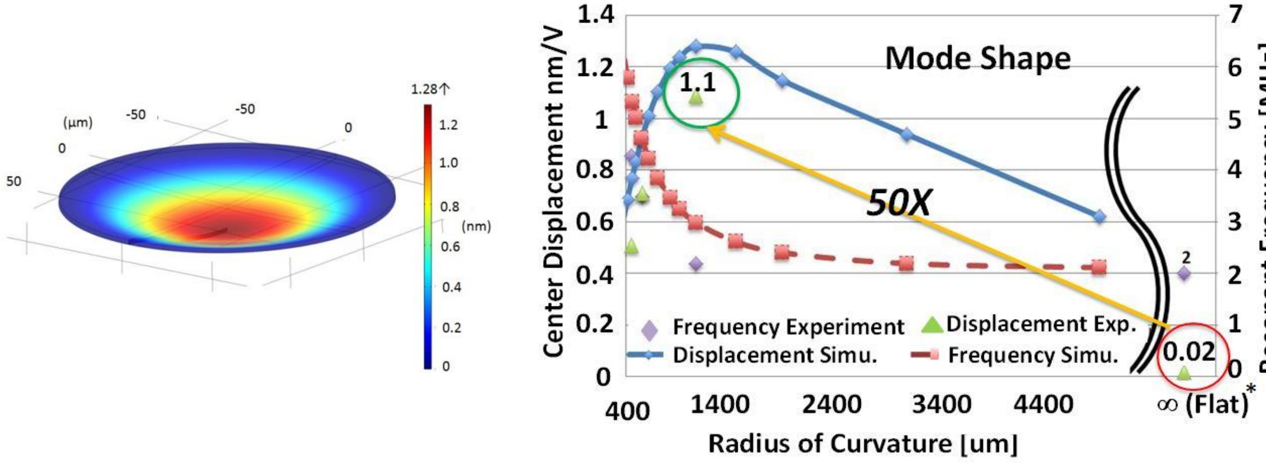

Fig. 2.7.1. (a, left) Simulated operation mode shape and DC displacement of a curved pMUT. (b, right) Good consistency between simulations (line) and experiments (symbols) with 140µm in diameters curved PMUT and different radii of curvature. Experimental results from a flat PMUT are also plotted.

Acoustic-piezoelectric frequency domain simulations have also been conducted in COMSOL Multiphysics to estimate the frequency response of the curved diaphragms. Figure 2.7.2a shows center displacement (nm/V) versus frequency plot for a curved AlN pMUT with total thickness of 2.5 µm (including the metal electrode and bottom oxide layer), 190 µm nominal diameter and 1065 µm in radius of curvature operated in air. The simulated center DC displacement is 1.4 nm/V and the displacement at its resonance is 75 nm/V at 2.45 MHz.

The displacement measurements of this device conducted using a Laser Doppler Vibrometer (LDV) in air are shown in Fig. 2.7.2b. It has measured resonant frequency at 2.19 MHz, 1.1nm/V DC vertical displacement and 45 nm/V of center displacement at resonance. It is noted that LDV can only measure the velocity/displacement when the target is under motion so the DC displacement is measured at very low frequencies away from the resonance.

These results show good consistency between the simulation and the experiment. Experimental results show slightly lower displacement per volt and lower resonant frequency probably due to geometry mismatches (e.g. the fabricated diaphragm might not be perfect spherical shape), mass loading in the medium, and additional loss mechanisms in air damping and anchor.

Fig. 2.7.3 shows the impedance measurement in air for another curved pMUT which is 120 µm in nominal diameter and 550 µm in radius of curvature, and has a resonant frequency of 3.86MHz. The effective electromechanical coupling coefficient is calculated to be 2.1% in air from Fig. 2.7.3 using resonant and anti-resonant frequencies using Eq. (2.4.4.1). This value is in fact 40 times higher than the reported value for a state-of-art flat AlN pMUT operated in air, which was 0.056% [63]. We also calculated that the electromechanical coupling can in theory go as high as 3.3%. It must be noted that the maximum electromechanical coupling in vacuum that can be achieved with a circular, flat AlN diaphragm in this mode of operation is 5.5% and can be calculated as the following:

$$k_P{}^2 = \frac{2\left(d_{31}\right)^2 Y_0}{\varepsilon_r (1-\nu)} \tag{2.7.2}$$

Hence, such curved design can potentially reach 60% of material limit for the electromechanical coupling efficiency as opposed to the flat AlN pMUT which can only achieve 10% at its best [63].

Fig. 2.7.4 shows excellent measured linearity response between center displacement and the input voltage from a curved pMUT operated at 500 kHz – another desirable characteristic especially for medical imaging devices using harmonic imaging technique. As such, curved pMUTs could provide high sensitivity, miniaturization, and low manufacturing cost for broad applications.

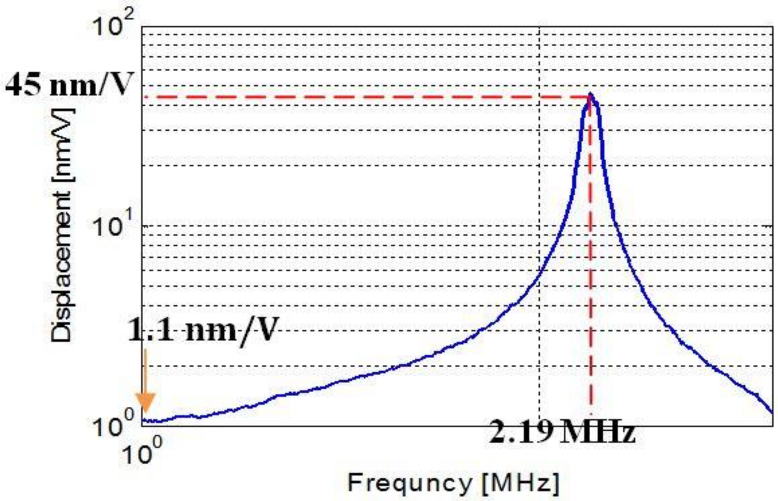

Fig. 2.7.2. FEA simulation Displacement versus frequency plots of a curved pMUT with 190µm in diameter and 1065µm in radius of curvature.

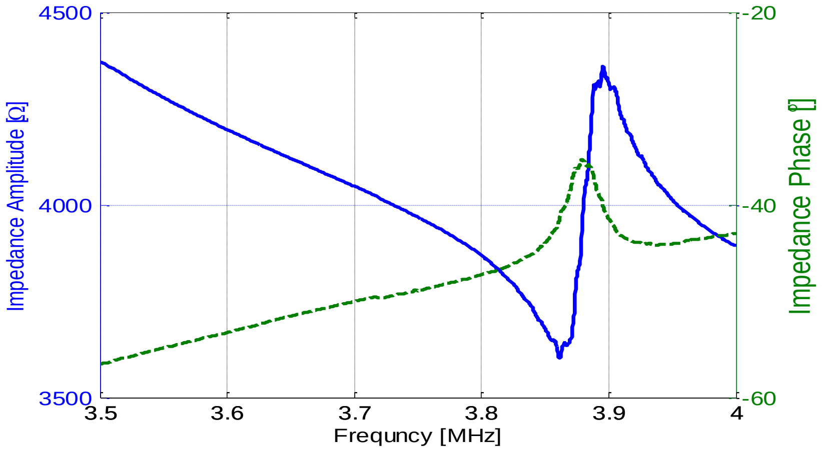

Fig. 2.7.3. Impedance versus frequency measurements (in air) of another curved pMUT with 120 µm in diameter and 550µm in radius of curvature.

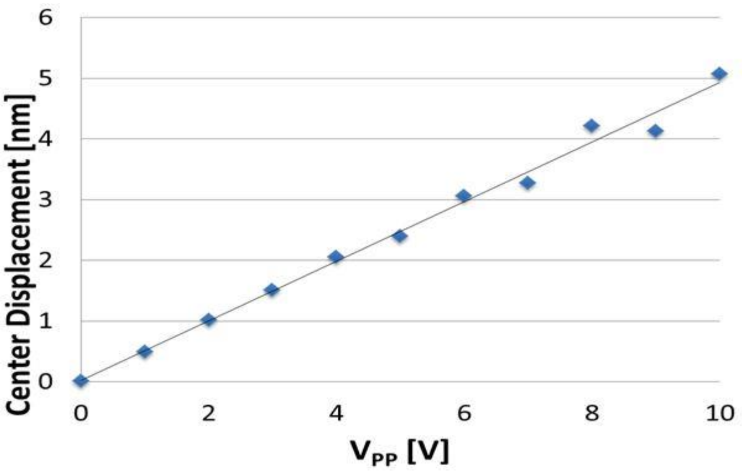

Fig. 2.7.4. Center displacement vs. the input voltage of a curved pMUT with 140µm in diameter and 1065µm in radius of curvature operated at 500 kHz.

2.8. Self-Curved Diaphragms by Stress Engineering for Curved PMUT

Up to this point we have shown the curved pMUT prototypes fabricated using HNA wet etching. Such wet etching process might be difficult to control in a foundry-based process, especially if high yield needs to be achieved for fabrication of arrays of the transducer. In addition, HNA wet etching results in formation of concave-shape dead areas around the diaphragm caused by lateral wet etching of silicon. This section presents the concept of self-curved diaphragms by stress engineering instead of the wet etching process as a new possible future approach for formation of curved diaphragms with a controllable profile for curved pMUT fabrication. In summary, this section presents: (1) fabrication of self-curved diaphragms without the wet etching process; (2) controllable designs of diaphragm curvature by the combination of residual stresses in thin films and their sizes; and (3) high fill-factor to construct self-curved pMUT arrays.

Figure 2.8.1 shows the 3D schematic diagram of the stress engineered, self-curved pMUT. The curved structure is realized by a piezoelectric AlN layer sandwiched between a bottom and a top metal electrode on top of a silicon diaphragm with a self-generated curvature due to residual stresses in the films. Specifically, the silicon nitride and silicon oxide layers with known tensile and compressive stress, respectively, are introduced on top of the device layer on a SOI wafer to induce the targeted concave-shape structure. The final curvature of the diaphragm is caused by the balance of stresses in various thin films and can be adjusted by the size and properties of the thin films. In the prototype demonstrations, suspended diaphragms can bend downward as illustrated without unutilized portions as those fabricated previously by the wet etching process. As such, a high fill factor can be achieved.

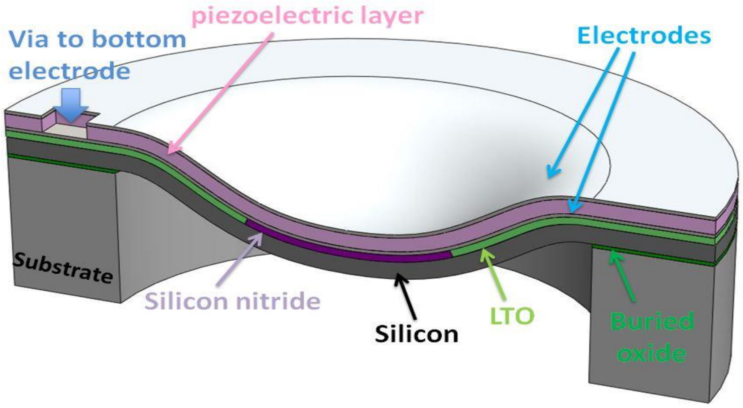

Fig. 2.8.1. 3D cross-sectional view of a stress engineered curved pMUT fabricated in a CMOS-compatible process.

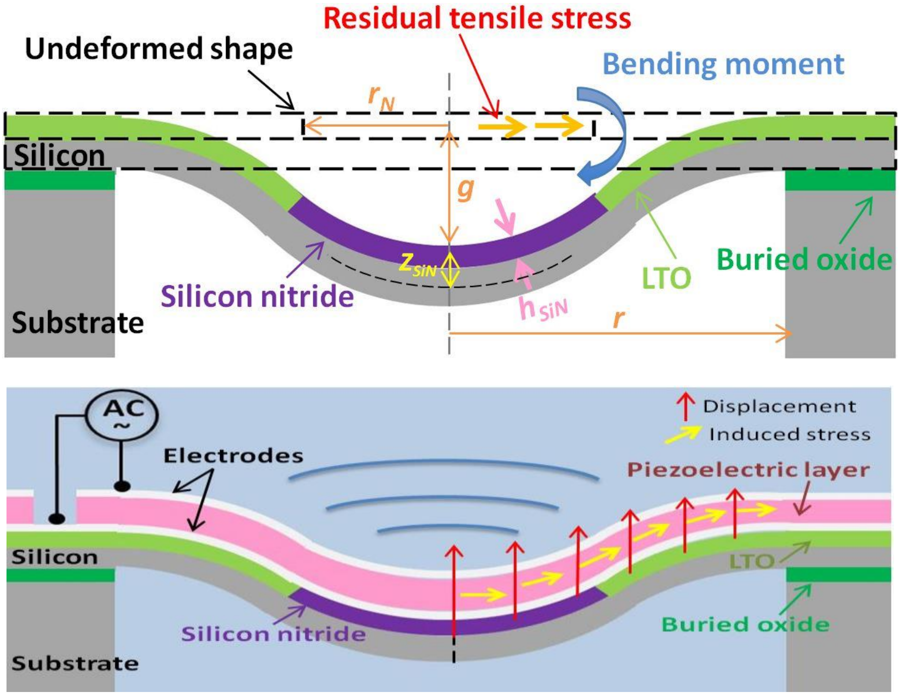

Fig. 2.8.2. (a, top) Cross-sectional view of the concave-shape diaphragm by the stress engineering process due to the SiN and LTO films with tensile and compressive residual stresses, respectively; (b, bottom) After adding the bottom and top electrodes and the AlN layer to complete the stress engineered curved pMUT fabrication.

The cross-sectional diagram in Figure 2.8.2a details the stress engineering design. The combination of tensile stressed silicon nitride layer (partially covering the central region of the circular diaphragm) and the compressive stressed LTO (covering the rest of the diaphragm) results in the concave-shape structure. Analytically, if a flat, stress-free, clamped diaphragm is deflected downward, lateral tensile stress is formed at the outer portion and radial compressive stress is established at the inner portion of the top surface of the diaphragm. The stress neutral line (zero stress) or the inflection circle is located at ~0.65r position, where r is the radius of the diaphragm. Therefore, the stress-free concave-shape diaphragm as illustrated in Fig. 2.8.2a can be achieved by placing a thin film with tensile residual stress at the inner portion and compressive stress in the outer portion of a flat diaphragm. Once the structure is released, a curved downward diaphragm results.

The curvature of the self-curved diaphragm can be designed to achieve a desirable center deflection, *g*, by tuning the silicon nitride and oxide residual stresses σ_{SiN} & σ_{Ox}, the silicon nitride and oxide thickness h_{SiN} & h_{Ox}, their distances from neutral axes Z_{SiN} & Z_{Ox}, Poisson's ratios v_{SiN} & v_{Ox}, and the coverage radius r_N. The radial force per unit length due to the residual stress in the nitride film is simplified as $\sigma_{SiN}h_{SiN}$, and the moment per unit length generated by the nitride layer about the neutral axis of the diaphragm stack is $\sigma_{SiN}h_{SiN}Z_{SiN}$. The residual stresses in the thin films can generate sufficeint moments to bend the released diaphragm after the backside silicon is etched away [35]. The deformation profile, $W_s(r)$, is:

$$W_s(r) = \frac{\pi\sigma_{SiN}h_{SiN}Z_{SiN}}{rD(1-\upsilon_{SiN})}\sum_k \frac{\mathrm{O}_k(r_N)}{\Lambda_k\Gamma_k}\Psi_k(r) - \frac{\pi\sigma_{Ox}h_{Ox}Z_{Ox}}{rD(1-\upsilon_{Ox})}\sum_k \frac{\mathrm{O}_k(r_N)}{\Lambda_k\Gamma_k}\Psi_k(r) \tag{2.8.2}$$

where *r* and *D* are the diaphragm nominal radius and flexural rigidity, respectively and O_k, Ψ_k, Λ_k, and Γ_k are functions defined in [35].

By adding the bottom and top electrodes and the AlN layer to complete the fabrication process after Fig. 2.8.2a, the stress engineered curved pMUT can operate as shown in Fig. 2.8.2b in the transmission mode under an AC voltage. The induced stress in the piezoelectric layer due to the d_{31} effect stretches and compresses the diaphragm, such that it resonates in the flexural mode to emit acoustic waves. The induced stress due to d_{31} has a vertical component in the desired vertical motion to enhance electromechanical coupling of the device.

2.8.1. Fabrication Process Flow and Results

Figure 2.8.1.1 shows the process flow of the stress engineered self-curved pMUT. The process starts with the deposition and pattering of a 650 nm-thick silicon nitride layer with naturally inherent tensile residual stress (650MPa in our lab) on a SOI wafer with a 4 μm-thick device layer and a 1 μm-thick BOX layer (Fig. 2.8.1.1a). The next step is LTO deposition followed by chemical mechanical polishing (CMP) (Fig. 2.8.1.1b). There are two purposes for LTO deposition and CMP: (1) to smooth out the surfaces for the future Mo/AlN/Mo sputtering on the diaphragm area, and (2) to further help the curvature formation by using the LTO residual compressive stress, which in our case is 180 MPa (compressive). Backside deep reactive ion etching (DRIE) is then used to release the self-curved diaphragm (Fig. 2.8.1.1c). After the BOX layer under the diaphragm is removed, the diaphragm bends in a concave form due to the residual stresses of the nitride and oxide thin films before the depositions of electrode layers and AlN piezoelectric layer using active sputtering of Mo/AlN/Mo as bottom electrode, piezoelectric layer, and top electrode with 150nm, 2μm, and 150nm in thickness, respectively. The via to the bottom electrode is opened using a combination of dry and wet AlN etching steps by chlorine based plasma and the MF-319 developer, respectively (Fig. 2.8.1.1d) in order to reduce the damage to the Mo bottom electrode layer. The top Mo layer is patterned before the SF_6 plasma etching.

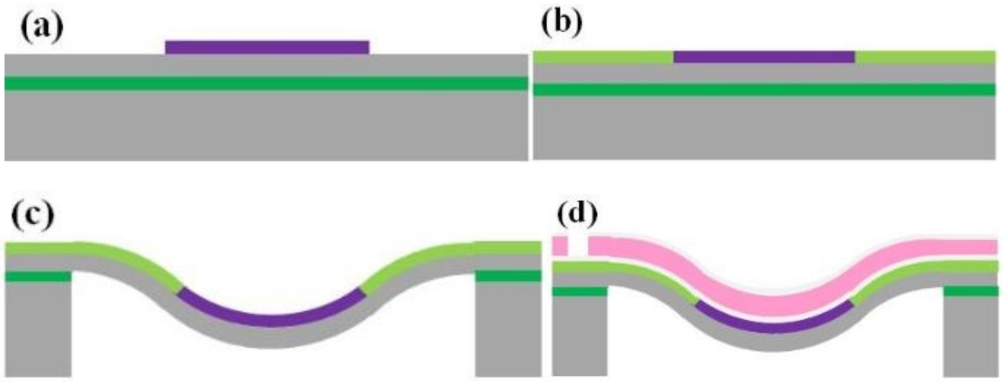

Fig. 2.8.1.1. Process flow for the stress-engineered curved pMUT: (a) silicon nitride deposition and patterning; (b) LTO deposition and CMP; (c) backside DRIE to form the concave-shape diaphragm; (d) Mo/AlN/Mo sputtering and via opening to the bottom electrode.

Figure 2.8.1.2 shows confocal laser scanned images captured using Olympus LEXT OLS4000 3D Confocal Laser Microscope of a fabricated, self-curved pMUT with 400µm in diameter, 50% nitride coverage, and measured center deflection of 2.7µm.

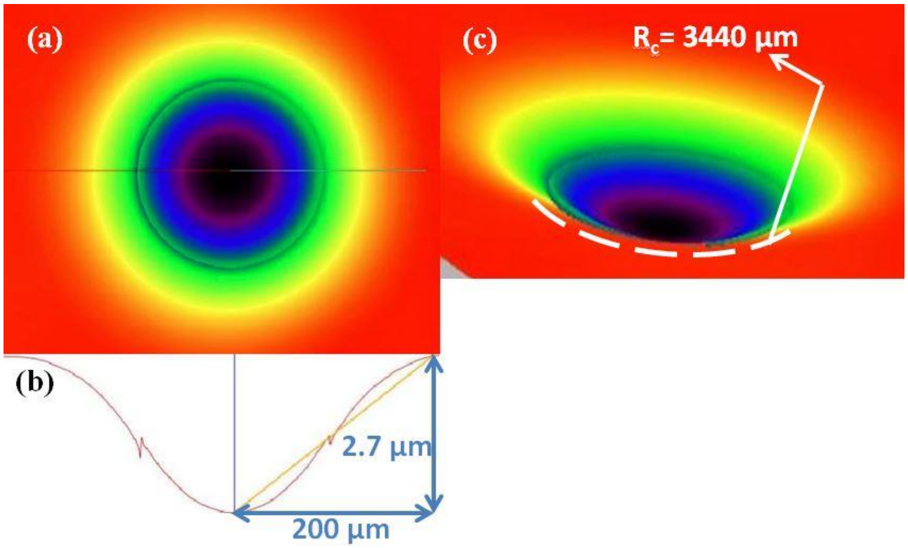

Fig. 2.8.1.2. Confocal laser scanned image of a fabricated curved pMUT (a) top view; (b) measured curvature profile; (c) 3D tilted view and the radius of curvature.

Figures 2.8.1.3a & 2.8.1.3b are SEM micrographs of two self-curved pMUTs portraying the clamped and curved diaphragm. Figure 2.8.1.3c shows a cross-sectional view of the diaphragm stack composed of - from bottom to top, the buried oxide, silicon device, silicon nitride, and LTO layers as well as the Mo bottom electrode, AlN layer, and the top Mo electrode, respectively. Figure 2.8.1.3d is a close-up view on the AlN illustrating good crystal orientation.

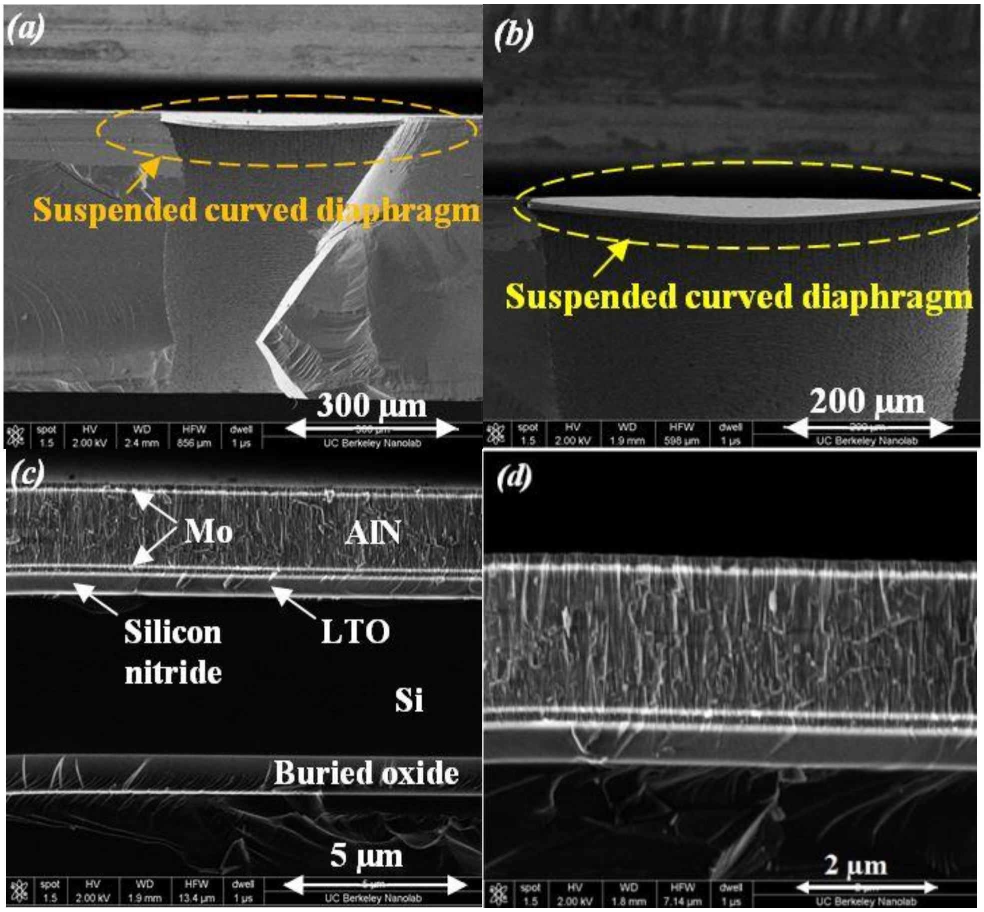

Fig. 2.8.1.3 (a, b) Tilted and front view SEM micrographs of two self-curved pMUTs after the devices are cleaved; (c) a released diaphragm showing the stack of the pMUT layers, and (d) close-up view showing good crystal alignment of AlN on the curved diaphragm.

2.8.2. Results and Discussions

The center diaphragm deflection, g, versus the silicon nitride radial coverage percentage, r_N, is shown in Figure 2.8.2.1 for a diaphragm with a nominal radius of 200 µm and silicon thickness of 4 µm. The 650 nm–thick SiN has a tensile residual stress of 650 MPa and the LTO has a compressive residual stress of 180 MPa. Results show good consistency between theory (coded in Matlab^{TM}), simulation (COMSOL), and experimental data. It is observed that the higher nitride coverage results in higher center deflection for the range of nitride coverages between 40%-55%. Since the curvature of the diaphragm can affect both the resonant frequency and the excited deformation of the devices, the SiN radial coverage ratio can be used in the design process to optimize the device performance. If the coverage percentage increases to be above the inflection circle (roughly 65%-70% of the radius of the diaphragm), the center deflection will start to reduce as compressive regions of the diaphragm can start to reduce the bending moment. The optimal design values can be analyzed or simulated with known properties and parameters of the thin films.

The dynamic responses of a fabricated curved pMUT without (blue) and with (red) the bottom silicon layer are measured using Laser Doppler Vibrometer (LDV) and presented in Figure 2.8.2.2. Resonant frequency reduces from 646.7 to 520 kHz while low frequency displacement remains at 0.58 nm/V after the removal of the silicon layer. It is expected from Finite Element Modeling (FEM) that the released diaphragm without silicon would have lower resonant frequency of 381 kHz and higher low-frequency displacement of 8.5 nm/V as compared to the measured values. The discrepancy between the theoretical and experimental data is attributed to the excessive residual stress in the as-deposited AlN layer (tensile 170 MPa).

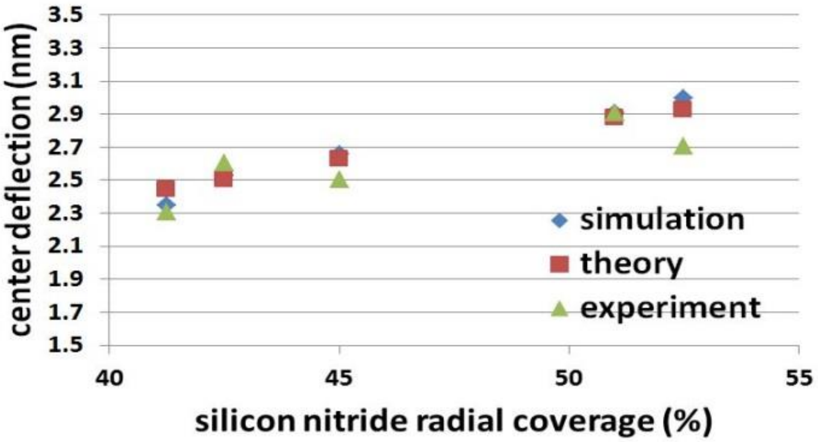

Fig. 2.8.2.1. Center deflection versus nitride radial coverage (%) for devices with 200μm in nominal radii using a 650nm-thick nitride layer. Results show good consistency among simulation, theory, and experimental data.

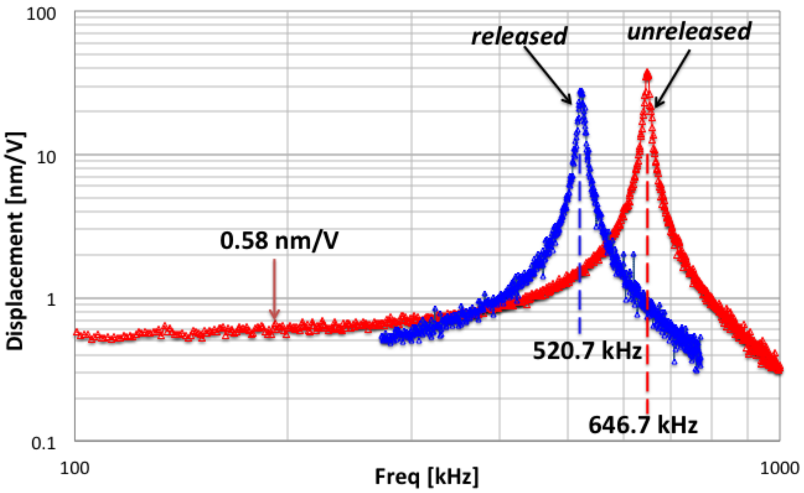

Fig. 2.8.2.2. Measured dynamic responses of stress-engineered curved pMUTs without (blue) and with (red) the bottom silicon layer. The pMUTs have 200μm in nominal radius and 2.7μm center deflection before release. The AlN, Si, and BOX layer thicknesses are 2μm, 4μm, and 1μm, respectively.

Figure 2.8.2.3 shows the effects of residual stress in AlN on the dynamic responses of stress engineered curved pMUT devices. As the residual stress in the AlN increases, the low-frequency displacement per unit input voltage drops and the resonant frequency increases. It is expected that the device performance would match with the simulated values when the stress in the sputtered AlN is controlled to be within 30 MPa.

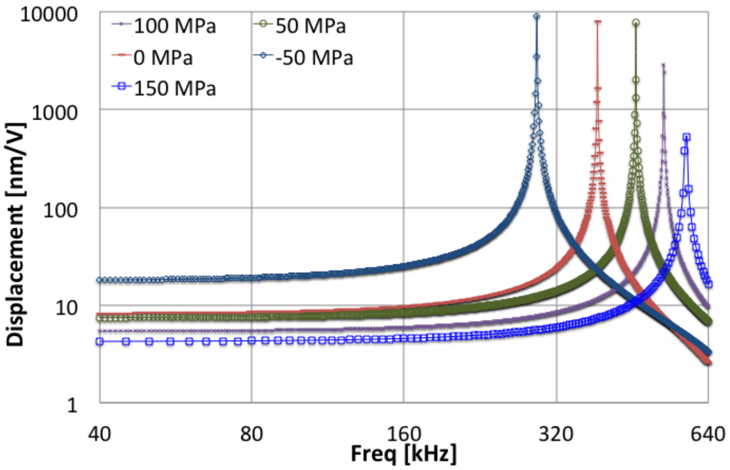

Fig. 2.8.2.3. Simulated dynamic responses of a stressed engineered curved pMUT with 200 μm in nominal radius and 2.34 μm center diaphragm displacement for -50, 0, 50, 100, and 150 MPa residual stress in the AlN layer.

2.9. Conclusion and Summary of Results

Theoretical as well as simulation analysis has been done for curved pMUTs in order to extract the optimum design for displacement electromechanical coupling enhancement. We successfully fabricated curved AlN pMUTs in a CMOS-compatible fabrication process for a targeted frequency range of 1 to 4 MHz, suitable for imaging of deep organs inside the body. More than an order of magnitude in response improved over flat pMUT was predicted in theory and measured in experiment. Table 2.9.1 shows a comparison between the obtained results for curved AlN pMUT and the state-of-art flat AlN pMUT.

Table 2.9.1. Results comparison between the curved and flat AlN pMUTs.

	Flat pMUT	**Curved pMUT**	**Enhancement**
DC Displacement (nm/V)	**0.02**	**1.1**	**x50**
Electromechanical coupling (theory/simulation)	**0.5%**	**3.3%**	**x6**
Electromechanical coupling (experiment)	**0.056%**	**2.1%**	**x40**

Chapter 3

Bimorph PMUT

3.1. Introduction and Device Concept

This chapter describes the design, fabrication and testing of the dual-electrode bimorph (DEB) pMUT structure, where bimorph refers to a device with two active piezoelectric layers as opposed to the unimorph structure with one active layer. Both analytical and experimental results show that that the device has sensitivity 4 times higher than that of the state-of-the-art flat pMUT with similar geometry, resonant frequency and material. As such, DEB pMUT may find potential air- and liquid-coupled applications.

Figure 3.1.1 shows the 3D schematic of a DEB pMUT (cross-sectional view). The device consists of two active piezoelectric layers and four electrodes: top, inner circular (middle layer), outer annular (middle layer), and bottom electrodes. Via etches are used to expose the buried middle and bottom electrodes for electrical connections. The backside etch-through hole is formed to release the diaphragm and to define the circular-shaped clamped boundaries. A thin inactive AlN layer, which is nearly impervious to the backside etch chemistry, is used as an etch-stop at the bottom of the diaphragm. The inner and outer electrodes are separated by a small gap and are driven differentially, while the top and bottom electrodes are grounded. The piezoelectric-induced strain gradient in the active layers causes the diaphragm to deform and move in flexural mode, launching acoustic waves into the contact medium.

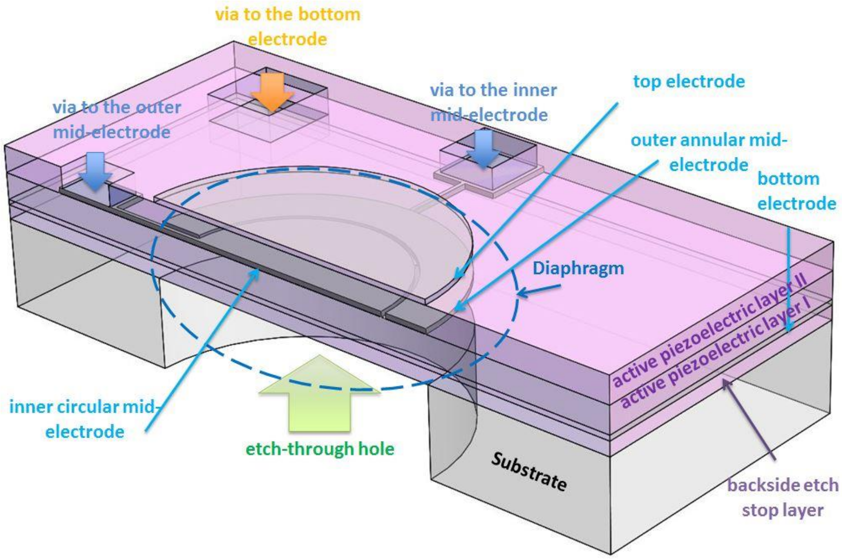

Fig. 3.1.1. The 3D schematic diagram showing the cross-sectional view of a bimorph pMUT with two active piezoelectric layers and the dual-electrode configuration: inner circular and outer annular electrodes (middle layer) with top and bottom electrodes.

In order to illustrate the operation of a DEB pMUT, we first start with explaining the working principle of a conventional unimorph pMUT followed by that of a dual-electrode unimorph pMUT. Next, we compare their performances using a simple model, showing that the displacement per input voltage of a DEB pMUT can theoretically be 4X that of a state-of-the-art unimorph pMUT.

Figure 3.1.2a shows a 2D axisymmetric view of a conventional unimorph pMUT, which consists of a single active piezoelectric layer, a structural layer, a bottom electrode and a circular top electrode. By applying an electric field between the top and bottom electrodes, an in-plane electromechanical strain is induced in the portion of the piezoelectric film that is covered by the top electrode due to the d_{31} effect. The stress gradient along the thickness of the diaphragm in the electrode-covered area generates a bending moment about the neutral axis of the diaphragm, which forces the diaphragm to move out-of-plane in a flexural mode. The moving device is an energy source for the medium in the transmission mode, as it transforms electrical energy to acoustic energy and radiates acoustic waves. The piezoelectrically induced moment resultant, i.e. the induced bending moment per unit transverse length for a single-electrode unimorph is [39, 40]:

$$M_p = \sigma_p h_p Z_p \tag{3.1.1}$$

where σ_p is the piezoelectrically induced biaxial stress in the piezoelectric layer, h_p is the piezoelectric layer thickness, and Z_p is the distance from the middle of the piezoelectric layer to the neutral axis of the diaphragm. The strain-stress and the transverse piezoelectric constitutive equations are:

$$\sigma_p = \left[Y/(1-\nu)\right]\varepsilon_p = Y_b \varepsilon_p \tag{3.1.2}$$

$$\varepsilon_p = d_{31} E_p \tag{3.1.3}$$

where Y and ν are the Young's modulus and Poisson's ratio of the piezoelectric layer, respectively, Y_b is the biaxial Young's modulus ($Y_b=Y/(1-\nu)$) of the piezoelectric layer, ε_p is the piezoelectrically induced biaxial strain, and E_p is the applied electric field in the piezoelectric layer. Substituting Eqs. (3.1.2) and (3.1.3) in Eq. (3.1.1):

$$M_p = Y_b d_{31} Z_p V_p \tag{3.1.4}$$

where V_p is the applied voltage between the two electrodes, i.e. $V_p=E_p h_p$. As expected, the induced forcing function is proportional to the applied voltage and the piezoelectric constant. In addition, the center displacement of the device in its first mode of operation is proportional to the induced moment resultant, M_p [35].

Here we define UM_p as the unit of induced bending moment resultant per unit input voltage. For a conventional unimorph pMUT with certain material properties and geometry, it is assumed, for the purpose of comparison, that the bending moment resultant has the value of $1UM_p$.

Figure 3.1.2d shows a clamped circular diaphragm of radius, *a*, operating at its first mode. When the top inner portion (the inflection point is ~0.7a from the center [13]) is under tensile stress, the top outer portion is under compressive stress. If the dual-electrode unimorph pMUT (as shown in Fig. 3.1.2b) is driven differentially with the same voltage magnitude but opposite polarity to the inner and outer electrodes, the top inner (outer) portion of the diaphragm will be under expansion, while the outer (inner) portion of the diaphragm will be under contraction. Thus, for a dual-electrode unimorph pMUT with the same geometry and material properties as the conventional unimorph pMUT, the overall generated moment resultant is $2UM_p$, and therefore, the displacement per input voltage is twice that of a single-electrode unimorph pMUT.

The bimorph pMUT with dual electrodes as shown in Fig. 3.1.2c are inspired by the well-known cantilever-type piezoelectric bimorph structures (e.g., [66]) with two active piezoelectric layers, both of which directly contribute to the transformation of electrical energy into mechanical energy. The device has three layers of electrodes, where the top and bottom electrodes are grounded and the middle electrode is patterned similarly to the top electrode of the dual-electrode unimorph pMUT. In order to better understand the operation of a DEB pMUT it must be noted that: a) the two active layers have similar piezoelectric polarity but the induced electric fields have opposite directions due to the electrode configuration, thus, the induced stresses have opposite signs in the piezoelectric layers at every radial position; b) As shown in Fig. 3.1.2d, the in-plane stresses on the top and bottom portions at each radial position of a bending diaphragm have opposite signs. As a result, the top and bottom active layers of a DEB pMUT with the same mechanical properties as the conventional unimorph pMUT each generate bending moment of $2UM_p$. As a consequence, when the middle electrodes are driven differentially, the generated moments from each portion contribute constructively to the diaphragm deformation and the overall moment resultant will be equivalent to $4UM_p$. As such, the proposed DEB pMUT offers 4X the drive sensitivity when compared with a unimorph pMUT with similar lateral geometry, stiffness, and material properties.

The energy efficiency of the devices is calculated from the ratio of the output mechanical energy to input electrical energy with the following assumptions: The diaphragm area is A_p; the inner electrode and outer electrode areas are both equal to $0.5A_p$ (the ring-gap area between the electrodes is negligible); the piezoelectric layer thickness and permittivity are h_p and ε_p respectively; the effective mechanical stiffness at the center is k_{mc}; and the center displacement for a single-electrode unimorph pMUT driven by V_p is x_c. The electrical and mechanical energy equations for the single-electrode unimorph pMUT are:

$$E_{e\_SU} = \frac{1}{2}\left(\frac{0.5A_p\varepsilon_p}{h_p}\right)V_p^2 = \frac{1}{4}\left(\frac{A_p\varepsilon_p}{h_p}\right)V_p^2 \tag{3.1.5}$$

$$E_{m\_SU} = \frac{1}{2}k_{mc}x_c^2 \tag{3.1.6}$$

thus, the electromechanical efficiency is:

$$\eta_{E\_SU}=\frac{E_{m\_SU}}{E_{e\_SU}}=2\left(\frac{h_p k_{mc}}{A_p\varepsilon_p}\right)\left(\frac{x_c}{V_p}\right)^2 \tag{3.1.7}$$

For the dual electrode unimorph pMUT:

$$E_{e\_DU}=\frac{1}{2}\left(\frac{0.5A_p\varepsilon_p}{h_p}\right)V_p^2+\frac{1}{2}\left(\frac{0.5A_p\varepsilon_p}{h_p}\right)V_p^2=\frac{1}{2}\left(\frac{A_p\varepsilon_p}{h_p}\right)V_p^2=2E_{e\_SU} \tag{3.1.8}$$

$$E_{m\_DU}=\frac{1}{2}k_{mc}(2x_c)^2=2k_{mc}x_c{}^2=4E_{m\_SU} \tag{3.1.9}$$

$$\eta_{E\_DU}=\frac{E_{m\_DU}}{E_{e\_DU}}=4\left(\frac{h_p k_{mc}}{A_p\varepsilon_p}\right)\left(\frac{x_c}{V_p}\right)^2=2\eta_{E\_SU} \tag{3.1.10}$$

It must be noted that due to the actuation of two electrodes, the input energy is twice as that of a single-electrode unimorph if we use the same input voltage, however, the output mechanical energy is 4X higher, therefore, the electromechanical efficiency is 2X greater. Furthermore, the energy equations for the DEB pMUT are:

$$E_{e\_DB}=2\times\frac{1}{2}\left(\frac{0.5A_p\varepsilon_p}{h_p}\right)V_p^2+2\times\frac{1}{2}\left(\frac{0.5A_p\varepsilon_p}{h_p}\right)V_p^2=\left(\frac{A_p\varepsilon_p}{h_p}\right)V_p^2=4E_{e\_SU} \tag{3.1.11}$$

$$E_{m\_DB}=\frac{1}{2}k_{mc}(4x_c)^2=8k_{mc}x_c{}^2=16E_{m\_SU} \tag{3.1.12}$$

$$\eta_{E\_DB}=\frac{E_{m\_DB}}{E_{e\_DB}}=8\left(\frac{h_p k_{mc}}{A_p\varepsilon_p}\right)\left(\frac{x_c}{V_p}\right)^2=4\eta_{E\_SU} \tag{3.1.13}$$

It is found from Eq. (3.1.13) that the energy efficiency of the DEB pMUT is 4X that of a single-electrode unimorph pMUT. In conclusion, both the drive sensitivity and energy efficiency of the DEB pMUT are 4X those of a single-electrode unimorph pMUT with similar geometry and mechanical properties.

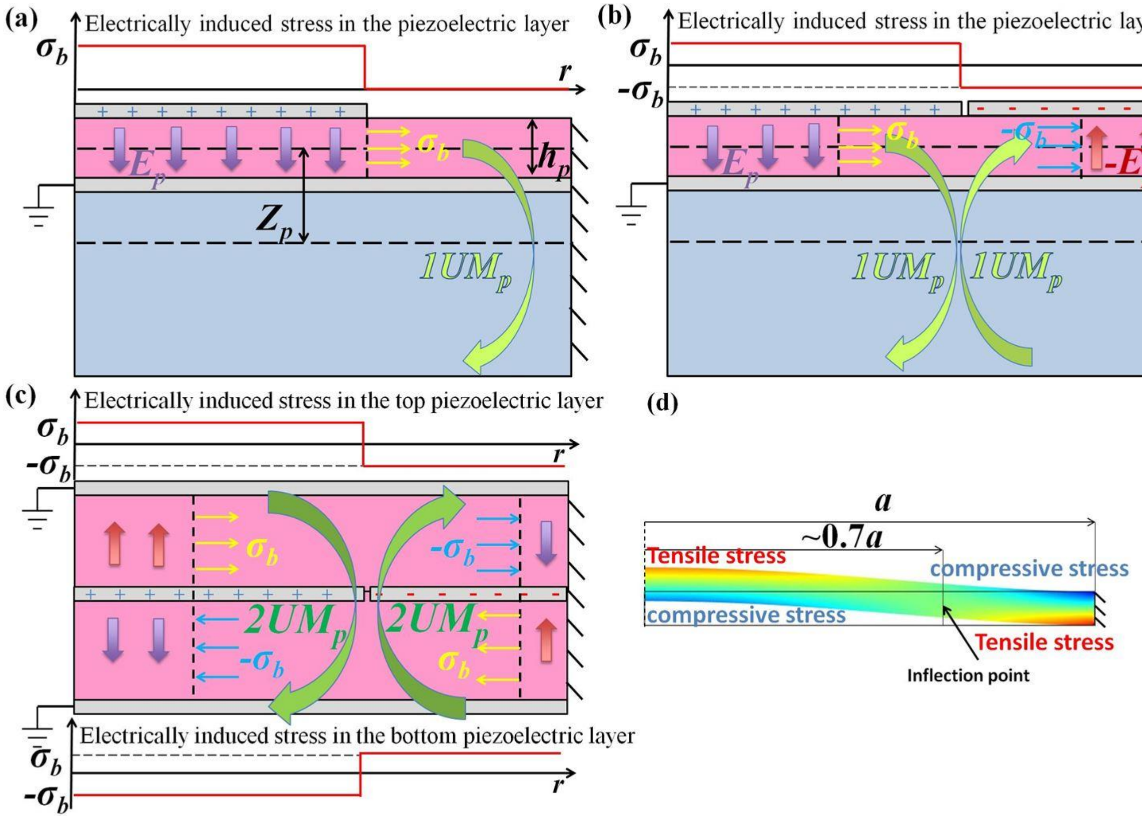

Fig. 3.1.2. The 2D axisymmetric views of (a) the conventional single-electrode unimorph pMUT with one active layer; (b) the dual-electrode unimorph pMUT with one active layer and inner and outer electrodes driven differentially; (c) the DEB pMUT to be driven differentially, which is expected to have 4X the drive sensitivity comparing to (a); (d) the normal radial stress profile of a clamped diaphragm at its first mode of operation.

3.2. Fabrication Process and Results

3.2.1. Process Flow

Figure 3.2.1.1 shows the CMOS-compatible fabrication process flow for the DEB pMUT. The process starts with sputtering of an AlN/Mo/AlN stack with thicknesses of 210 nm, 130 nm, 715-950 nm (different AlN thickness for liquid- or air-coupled operations$^{)}$, respectively (Fig 3.2.1.1a). The first AlN layer serves as the backside deep reactive ion etching (DRIE) stop layer, while the Mo layer is the bottom electrode and the second AlN layer is the bottom active layer for the DEB pMUT. Figure 3.2.1.1b shows the PECVD deposition of a thin (60 nm) SiO_2 layer, followed by sputter deposition of the second Mo layer (130 nm) for the middle electrode (Fig. 3.2.1.1c). The SiO_2 layer helps increase the breakdown voltage and device stability, and also decrease the power consumption in case of inevitable AlN crystal defects that would otherwise result in current leakage. The SiO_2 barrier layer prevents the diffusion of the middle Mo electrode through the bottom AlN active layer along the crystal grain boundaries during the sputtering of the second AlN active layer, which occurs due to the possible stress mismatch between the first and the second AlN active layers and thermal effects. Such diffusion is more rapid and prominent at higher temperatures due to the following facts: a) the bottom active AlN layer expands, so the molecular voids or the lattice defects along the grain boundaries turn into a more susceptible diffusion path for Mo, b) diffusion pace is naturally faster at higher temperatures. The silicon dioxide layer acts as a uniform barrier that prevents the Mo layer from diffusing through the AlN layer. Diffusion of the Mo layer introduces two detrimental effects for the device: 1) the effective distance between the two electrodes sandwiching the AlN layer at some locations become much smaller than the AlN thickness, thus the induced electric field in the AlN layer becomes much higher than the expected value of V_{mb}/h_{AlN1}, where V_{mb} is the applied voltage between the middle and bottom electrodes and the h_{AlN1} is the first AlN active layer thickness. Such phenomenon results in reduction of the breakdown voltage of the device. 2) The AlN resistance reduces which makes it more difficult for the AlN capacitor to charge and perform electromechanical energy transformation. In addition, the device pulls more current from the power source due to finite resistance of AlN, therefore, the power consumption increases.

Figure 3.2.1.1d shows patterning of the middle Mo electrode and the silicon dioxide barrier layers using SF_6 and O_2 plasma etching. Figures 3.2.1.1e and 3.2.1.1f depict the sputter deposition of the second 715-950 nm-thick AlN active layer, and the second 60nm-thick SiO_2 barrier layer, which prevents the diffusion of metal via crystalline defects at the sharp edges of the patterned middle Mo electrode or other inherent crystalline defects in the second AlN active layer and acts as a protective mask for the wet etching of AlN in the following steps.

Figures 3.2.1.1g and 3.2.1.1h show the sputter deposition and patterning of the top Mo electrode layer. The dry etching in this step must be time controlled so that the second SiO_2 barrier layer does not get etched in the field area. Afterwards, via etching to the bottom and middle Mo electrodes is conducted in a two-step process. First, via etching to the bottom electrode is performed halfway using SF_6-O_2 plasma etching for SiO_2 and chlorine-based reactive ion etching (RIE) for AlN (Fig. 3.2.1.1i). The targeted etch depth is equal to the first AlN active layer thickness and is time controlled so that the remaining AlN height in the bottom and middle via become almost equal. Second, via etching to the bottom and middle electrodes are conducted simultaneously by the same chlorine-based RIE as in the previous step (Fig 3.2.1.1j). The via etching ends with a final wet etching of AlN using MF-319 developer at 40° C. The Mo is highly impervious to developer etching, so there is no risk of damaging the electrodes in case of over etching. The final step is the release of the diaphragm using a through-wafer backside DRIE process (Fig 3.2.1.1k). AlN is an excellent stop layer for the chemistry of SF_6 in the DRIE process since it is highly resistant to Fluorine-based plasma etching. Diffusion of the bottom Mo through the thin AlN stop layer could occur in the previous steps which makes the AlN stop layer moderately conductive. This slightly conductive etching stop layer reduces the accumulated electric charges on the bottom diaphragm surface that would repel the incoming ions during the DRIE process, thereby reducing the undercutting phenomenon around the edges of the diaphragm.

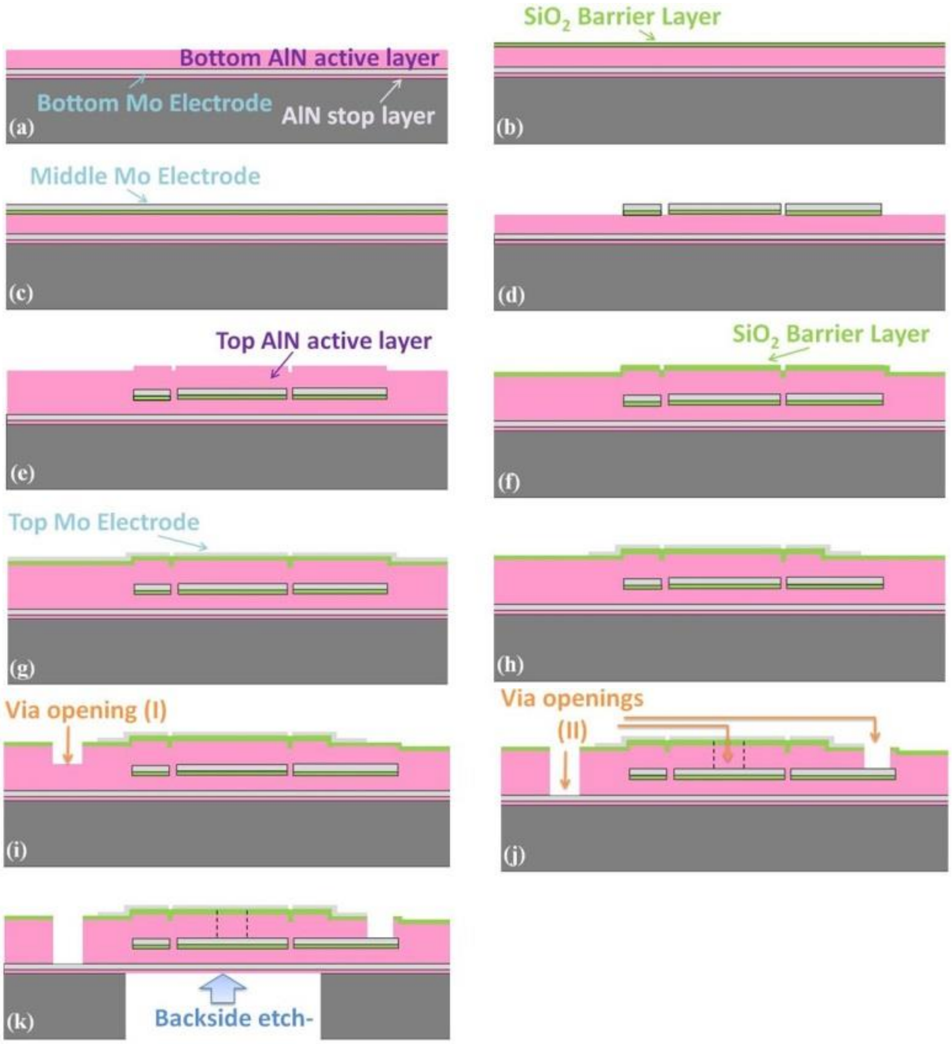

Fig. 3.2.1.1. The process flow of the DEB pMUT: (a) sputtering of AlN/Mo/AlN stack; (b) PECVD SiO2 deposition; (c) middle Mo Electrode sputtering; (d) patterning of the middle Mo electrode and SiO2; (e) second AlN active layer sputtering; (f) second PECVD SiO2 deposition; (g) top Mo electrode sputtering; (h) top Mo patterning; (i) via dry etching half-way down to the bottom electrode; (j) via dry and wet etching to expose the middle and bottom electrodes; (k) backside DRIE.

3.2.2. Fabrication Results

Prototype DEB pMUTs have been fabricated with radii of 100-230 μm in the form of single transducers and rectilinear arrays in form of single-, five-, and ten-element (channel)[3] devices, for both liquid-coupled and air-coupled applications. Figure 3.2.2.1a shows a diced, 10-element, 1D array of DEB pMUTs attached and wire bonded to a customized PCB. Every element is formed of an array of 6×60 DEB pMUTs and the pMUTs have radii of 115

---

[3] An array consists of multiple elements (channels) that can be driven separately, with multiple pMUTs comprising each element

μm. Figure 3.2.2.1b shows a close-up top-view microscopic image of the portion of an element of Fig 3.2.2.1a close to the bond-pads and connection areas. The top electrode and the vias to the middle and the bottom electrodes can be seen in Fig 3.2.2.1b. In addition, the patterned middle electrodes are visible because their edge pattern is transferred to the top layers.

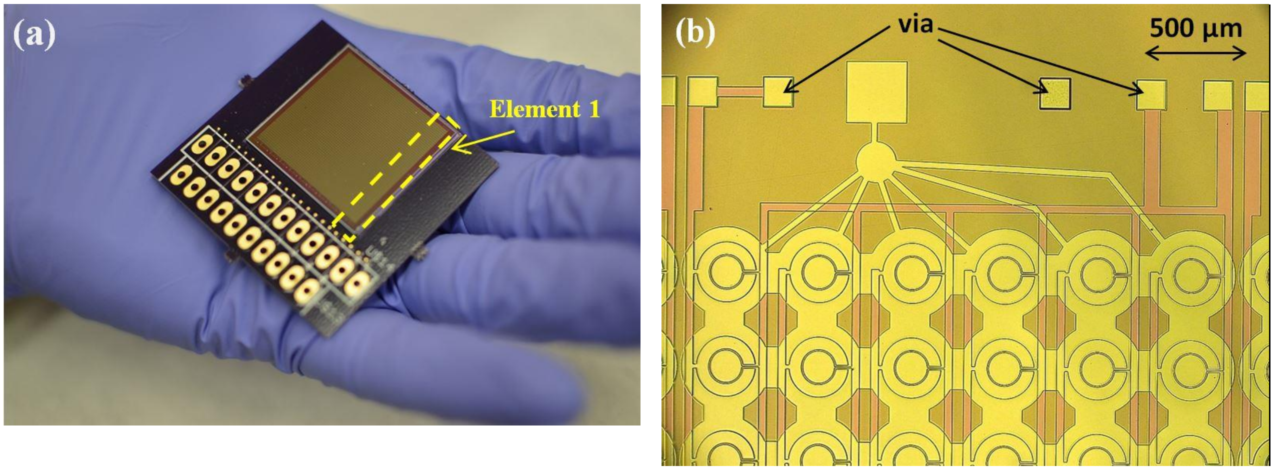

Fig. 3.2.2.1. (a) A 10-element array with 60×60 DEB pMUT attached to a PCB; (b) Top view optical image of the top edge of an element of the array shown in (a).

Figure 3.2.2.2a is a cross-sectional SEM micrograph of an array of cleaved DEB pMUTs showing the suspended diaphragms as well as the backside etch-through holes made by DRIE.

Figure 3.2.2.2b is a close-up view of a cleaved DEB diaphragm near the separation between the inner and outer middle electrodes showing the AlN and Mo layers. Apparent in this figure is the vertical orientation of the AlN crystal grains, which is critical to the success of the device because good crystallinity is required for good piezoelectricity in AlN.

Figure 3.2.2.2c is a suspended diaphragm near its clamped edge, showing the residual silicon (dark region) on the diaphragm backside close to the sidewall due to under-etching of silicon in the DRIE process. Figure 3.2.2.2d is a close-up SEM micrograph of a bottom-electrode via structure before the AlN wet etching has been completed, as evidenced by the residual AlN grains on top of the bottom electrode.

In order to investigate the crystalline quality of the deposited AlN layers, X-ray diffractometer (XRD) measurements have been conducted as shown in Figure 3.2.2.3 The first AlN layer can be directly measured after its sputtering. However, after the deposition of the second AlN layer, the XRD data only exhibits combined information regarding the overall quality of the first and the second AlN layers and do not reveal explicit data about the second layer. By comparing the data after different steps and from different locations, corresponding to three different film stacks of (a) AlN/Mo/AlN, (b) AlN/Mo/AlN/Mo/AlN/Mo, and (c) AlN/Mo/AlN/AlN/Mo, it is found that stack (b) in the (002) crystalline direction has higher amplitude and slightly narrower FWHM as compared to those of stack (a), indicating good quality of both the first and the second AlN layers. The FWHM has the measured value about 1.7°-1.8° from the Rocking Curve as another indication of good quality of AlN layers. The difference between the angle values at the intensity peaks among the stacks is due to the stage calibration error.

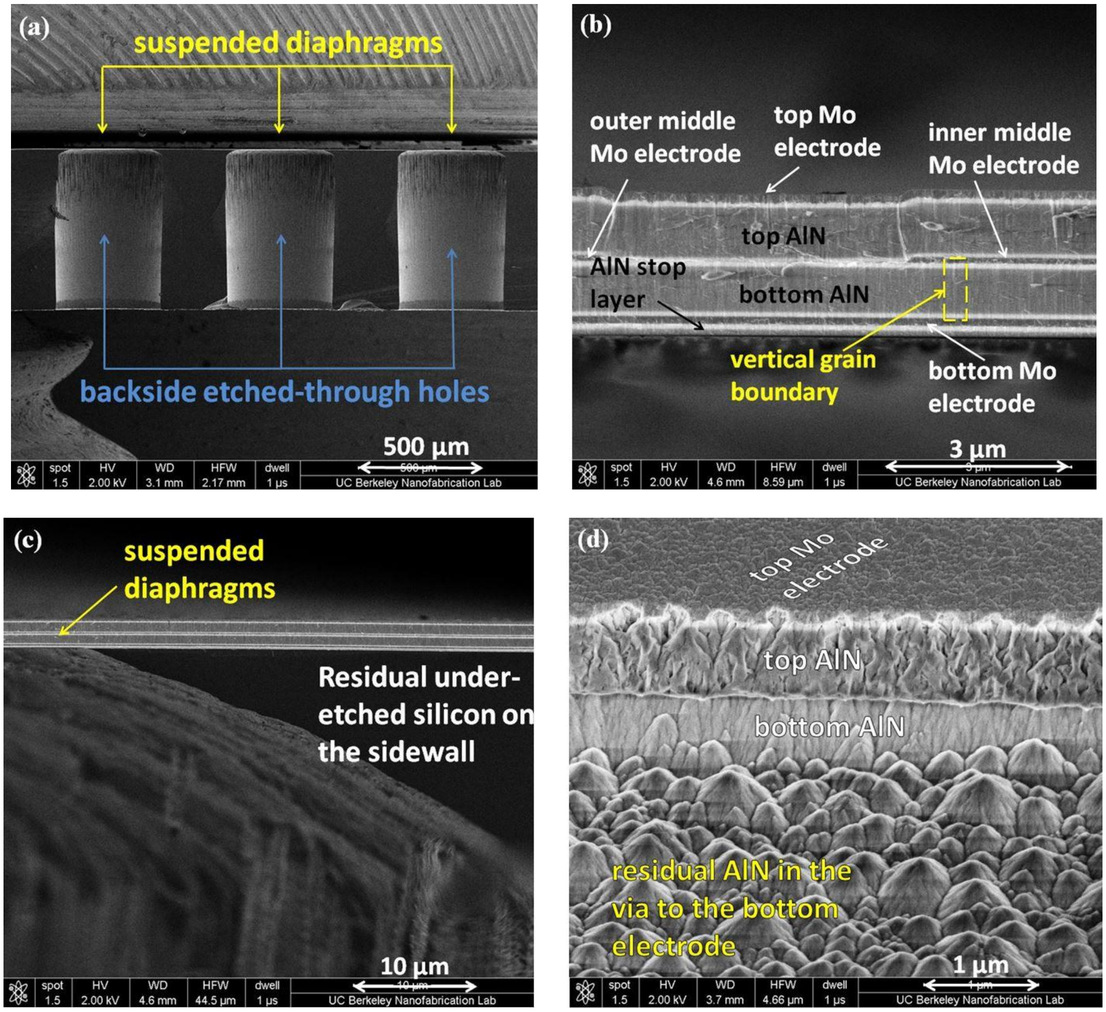

Fig. 3.2.2.2. (a) sideview SEM image of DEB pMUT, cleaved after the backside DRIE process; (b) close-up view of a DEB pMUT near the gap region between the inner circular and outer annular middle electrodes; (c) cross-sectional view SEM image of DEB pMUT of the suspended diaphragm showing the residual silicon around the edge of the diaphragm due to under-etching of backside silicon; (d) close-up SEM image of a via to the bottom electrode before the completion of the AlN etching process showing residual AlN grains on top of the bottom electrode.

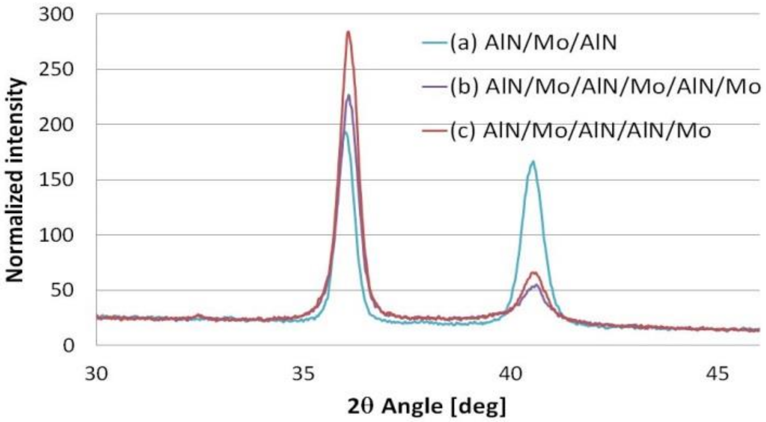

Fig. 3.2.2.3. XRD measurements of a DEB pMUT wafer on the AlN layers showing good crystallinity of the AlN layers. The first and second peaks are due to existence of AlN and Mo in the stacks, respectively.

3.3. Displacement Measurements Results

3.3.1. Drive Sensitivity of a Single DEB PMUT

In order to evaluate the operation of DEB pMUTs under different driving configurations, low frequency drive sensitivity of an air-coupled pMUT has been measured using a Laser Doppler Vibrometer (LDV). Low frequency displacement is equal to the product of fractional bandwidth and the resonant displacement, both of which need to be as high as possible for the best performance of the pMUT. Figure 3.3.1.1a shows the low frequency center displacement per input voltage of a prototype DEB pMUT with radius of 230 μm, total stack thickness of 2.4 μm, and the inner circular electrode radius of 70% of the diaphragm radius. When the inner electrode is driven while the outer electrode is grounded, the low frequency displacement is theoretically predicted as 7.50 nm/V, simulated by finite element analysis as 8.91 nm/V, and experimentally measured as 7.26 nm/V. When the outer electrode is driven with grounded inner electrode, the low frequency displacement is theoretically predicted as 7.27 nm/V, simulated as 6.65 nm/V, and experimentally measured as 5.75 nm/V. If the areas of the inner and outer electrode are equal, the theoretical actuation displacement by the individual inner and outer electrode should be equal. The discrepancy in the calculated and measured values comes mostly from the backside etching defects especially on the edges of the diaphragm, such as: over/under etching, residual silicon grass on the backside, and other fabrication uncertainties which change the effective shape, size, and mass distribution of the transducers. Under the differential drive, the measured low frequency displacement is 13.01 nm/V, only about 11.9% and 16% lower than the theoretical and simulated values of 14.76 nm/V and 15.54 nm/V, respectively. The differential drive mode produced 1.96x drive sensitivity, which is very close to the 2x improvement predicted by the analysis in Section II. On the other hand, the in-phase actuation resulted in negligible low frequency displacements as shown.

The center displacement frequency responses of two prototype-DEB pMUTs with radii of 230 and 170 μm have been characterized using LDV as shown in Figs. 3.3.1.1b and 3.3.1.1c, respectively. The frequency response matches well with the simulated data for both cases. The slight reductions in the displacement per input voltage values in experiments comparing to the simulation results are likely due to the residual stress in the structural layers (especially in the metal layers) and possible defects in the AlN crystalline structures with reduced piezoelectricity. Nevertheless, the value of 452 nm/V at the center resonant frequency of 345 kHz is 4.3X and 2.4X higher than those from the single-electrode (at 104 nm/V) and dual-electrode (at 188 nm/V) unimorph pMUT at a resonant frequency of 291 kHz [14]. As a result, the DEB pMUT can generate higher acoustic pressure (which is proportional to volumetric displacement-frequency product, i.e. volumetric velocity [5]). Another reason that the bimorph pMUT exhibits improved performance that also agrees more accurately with simulation results compared to reported unimorph pMUTs is that the sputtering of the films are done separately, thus, there is more margin for stress tuning at each step to achieve low stress in each layer in addition to tuning the average stress in the whole stack.

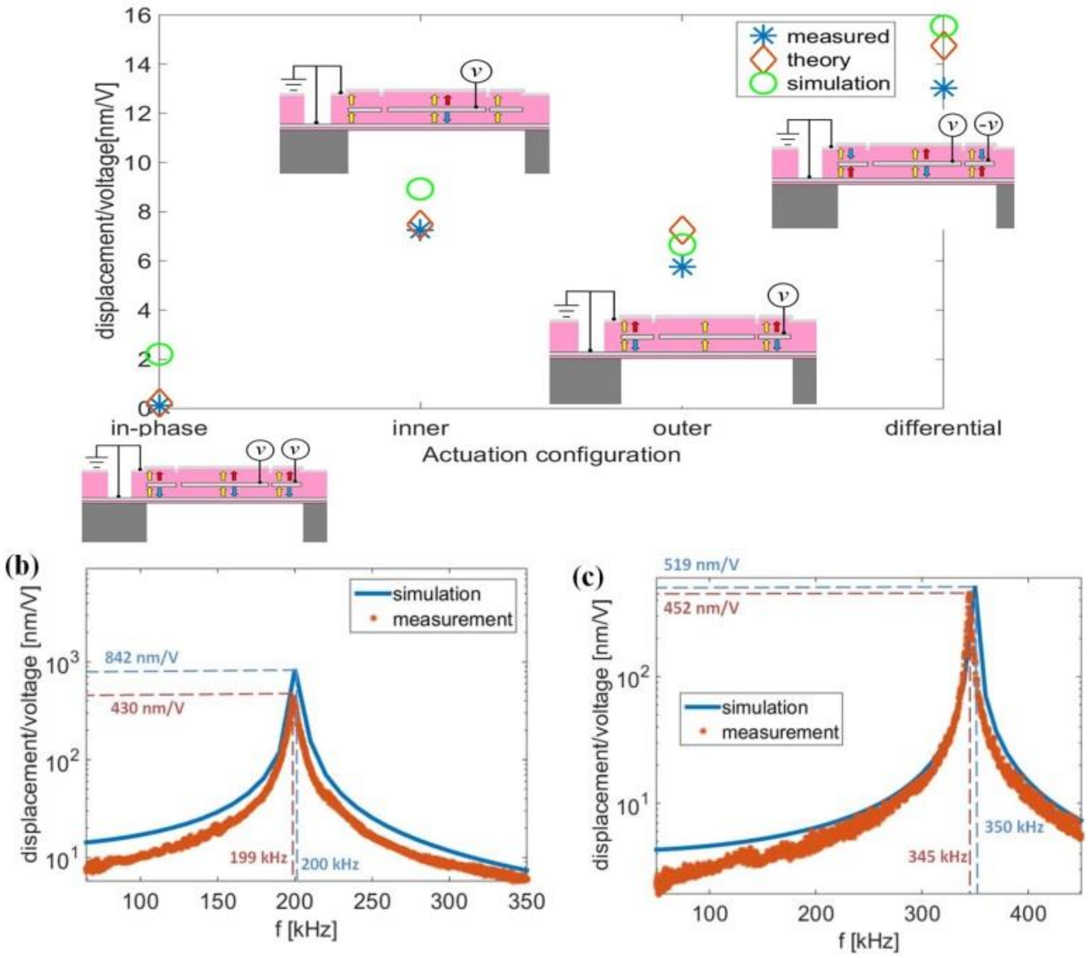

Fig. 3.3.1.1. (a) Low frequency center displacement/voltage results under different driving configurations from a prototype air-coupled DEB pMUT; (b,c) measured and simulated center displacement per input voltage frequency response of two prototype pMUTs with radii of 230 μm and 170 μm, respectively.

Table 3.3.1.1 compares the performances of previously reported unimorph pMUTs [14] with the same frequency ranges and the bimorph pMUT prototype of Fig. 3.3.1.1c. The table reveals that the bimorph pMUT with dual electrodes has superior performance because it has higher displacements per input voltage at higher resonant frequencies. The generated acoustic pressure is proportional to the combination of operation frequency and volumetric displacement. Thus, bimorph pMUTs are expected to generate higher pressure at higher frequency for high acoustic power transmission.

Table 3.3.1.1. Resonant displacement and resonant frequency of unimorph and bimorph pMUTs.

	Resonant Disp. [nm/V]	Center Freq. [kHz]
Unimorph w/ annular electrode	**86**	**291**
Unimorph w/ central electrode	**104**	**291**
Unimorph w/ two port diff. drv	**188**	**291**
Bimorph (this work)	**452**	**345**

3.3.2. Drive Sensitivity of a Single-Element DEB PMUT Array

The drive sensitivity measurements have also been conducted for individual transducers in an array structure. Figure 3.3.2.1a and 3.3.2.1b show the measured magnitude and phase of the center displacement with respect to frequency for a DEB pMUT located in row 5 and column 1 (5,1) of a 27×6 single-element array of DEB pMUT with a diaphragm radius of 100 μm and total stack (AlN/Mo/AlN/Mo/AlN/Mo) thickness of 2150 nm. The solid green lines show the response under the actuation of the inner circular electrode and the orange dashed lines are the responses under the actuation of the outer annular electrode. The blue dashed line in Fig 3.3.2.1a shows the response under the differential drive. The center displacement magnitudes have similar trend and value in both driving methods with 15.4% and 16.5% difference between their values at low frequency and resonance respectively (Fig. 3.3.2.1a). As discussed previously, the magnitude responses under the actuation of inner and outer electrode should be similar if the electrode areas are equal to half of the whole diaphragm area, but the difference here is likely due to the difference between the effective electrode areas as a result of various fabrication uncertainties, such as the outer electrode area change from the designed dimensions due to under/over backside etching and the non-symmetric shape of the annular electrode due to the inner electrode connection path passage gap. The center displacement magnitude under differential drive was measured to be 1.92X and 1.66X the center displacement magnitude under inner and outer electrode drive respectively. The deviation from the ideal case (expected 100% higher displacement in differential drive mode as opposed to 92% and 66%), can be due to the inequality of the electrode sizes after fabrication and the parasitic input electrical impedances of the inner and outer electrodes, which can cause the induced displacements from either port not to be completely in phase with the other.

On the other hand, as shown in Fig 3.3.2.1b, the measured displacement phases from inner and outer electrode actuation have almost opposite polarities (177^o phase offset on average) because inner- and outer-electrode drive induces motion in opposite directions. In other words, if the input harmonic voltage V on the inner electrode bends the diaphragm downward at time τ after the initial excitation, the same voltage on the outer electrode will bend the diaphragm upward (the opposite direction of motion) at time τ after the initial excitation, with the same displacement magnitude. Hence, if both of the inner and outer electrodes are driven with the same voltages simultaneously in phase, the diaphragm will have nearly zero flexural motion, while the differential drive mechanism gives twice higher amplitude as compared with results from the single-electrode drive. The reason why the phase offset is not exactly 180^o can be attributed to the parasitic impedances of the inner and the outer channels.

Figure 3.3.2.2a and 3.3.2.2b show the radial LDV scan results of pMUT (1,1) of the prototype single-element DEB pMUT array with 27×6 pMUTs where the outer electrode is driven by an AC voltage. Figure 3.3.2.2a shows the frequency response of various points along the radius of DEB pMUT (1,1) where p_1 is the center point, p_9 is a point on the rim anchor of the pMUT, and the rest of the points are placed between these two points. As the points are further away from the center location, the displacement amplitude becomes smaller until reaching zero at the clamped edge as predicted from the first mode of oscillation. Figure 3.3.2.2b shows the measured low frequency displacement per input voltage for points p_1 to p_9, demonstrating that the mode shape of the device follows the equation $\frac{\mathrm{w}}{\mathrm{w}_{\mathrm{max}}} = (1 - 1.25(\frac{\mathrm{r}}{\mathrm{a}})^2)^2$ with 0.99 R-Square value, where w is the normal displacement, r is the radial distance from the center, and a is the nominal radius of the diaphragm.[4] The fitted equation matches well to the equation $\frac{\mathrm{w}}{\mathrm{w}_{\mathrm{max}}} = (1 - (\frac{\mathrm{r}}{\mathrm{a}})^2)^2$ which is typically used to approximate the first mode shape of a clamped circular diaphragm [67]. The coefficient 1.25 in the fitted curve can be attributed to geometric imperfection due to backside under-etching creating an effective radius of (4/5)a during the backside DRIE process.

---

[4] It must be noted that in this fitting, the nominal radius, a=125 μm, is larger than the actual radius, and the fitting is valid for 0<r/a<0.8.

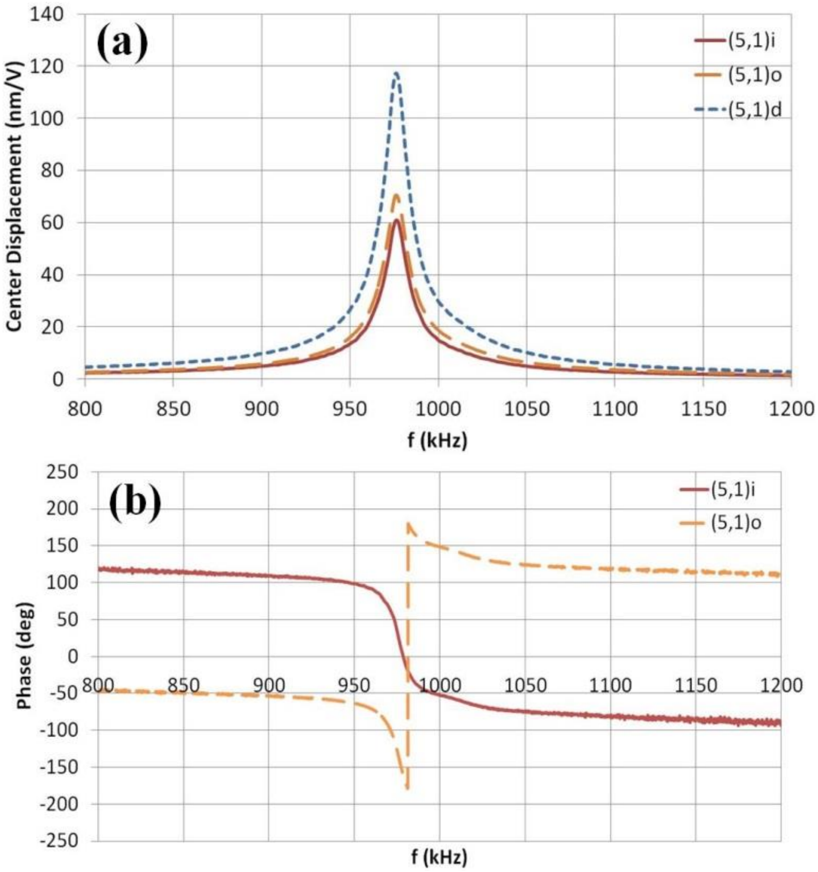

Fig. 3.3.2.1. Measured center displacement magnitude (a) and phase (b) versus frequency of DEB pMUT (5,1) of a single-element array of 27×6 pMUTs, measured using LDV under inner electrode (i), outer electrode (o) and differential drive (d) actuation schemes. As expected, the displacement responses under the inner and outer electrode actuation schemes have nearly the same magnitude with opposite polarities.

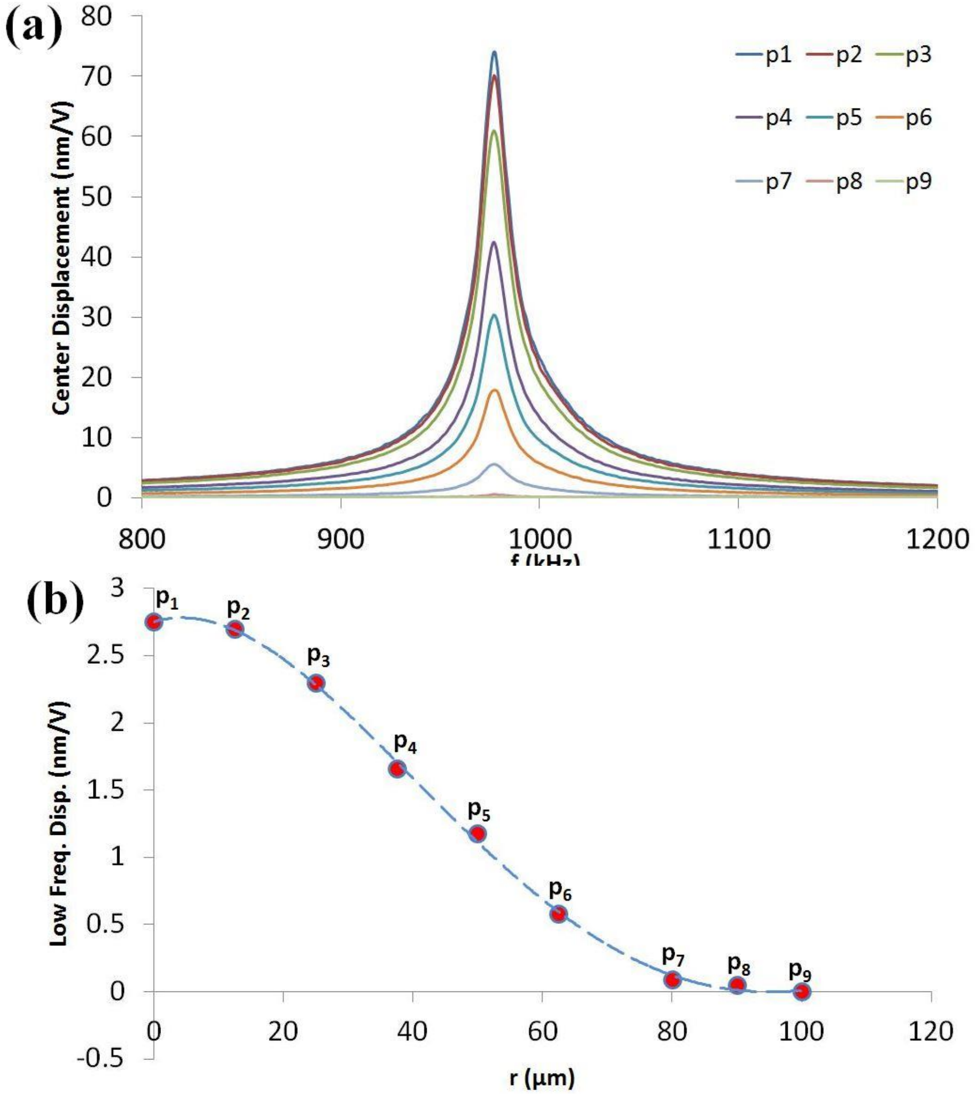

Fig. 3.3.2.2. (a) Displacement magnitude frequency responses of various points located along the radius of pMUT (1,1) of the array described in Fig. 3.3.2.1, where p_1 is at the center and p_9 is at the clamped edge of the diaphragm and the rest of the points lay in between sequentially; (b) low frequency displacement of points p_1 to p_9 described in (a) demonstrating the first mode shape of pMUT (1,1).

Experiments have also been conducted to record the drive sensitivity versus frequency for various DEB pMUT in the single-element array (the same array used for Fig. 3.3.2.1a) driven simultaneously via the inner electrodes and grounded outer electrodes. Figure 3.3.2.3a shows results of ten transducers with an average center frequency of 974.85 kHz and a standard deviation of 2.46 kHz. The average resonant displacement is 59.8 nm/V with a standard deviation of 4.5 nm/V, while the average low frequency displacement is 2.7 nm/V with a standard deviation of 0.7 nm/V. These results show very good consistency between the frequency responses of different transducers with only very small variations across the array.

Figure 3.3.2.3b shows that the phase angle responses of the same transducers in Fig. 3.3.2.3a are very close to each other and have similar phase shift frequencies. It can be noticed that as pMUTs are located further away from the bond pad with longer metal connecting path in between, their phase angles become smaller, i.e. shift toward negative. This is due to the larger stray capacitance caused by longer metal connector lengths from the bond pads to the pMUTs. To avoid this, connector areas can be designed to be equal by varying the connector width to compensate for the conductor length variations.

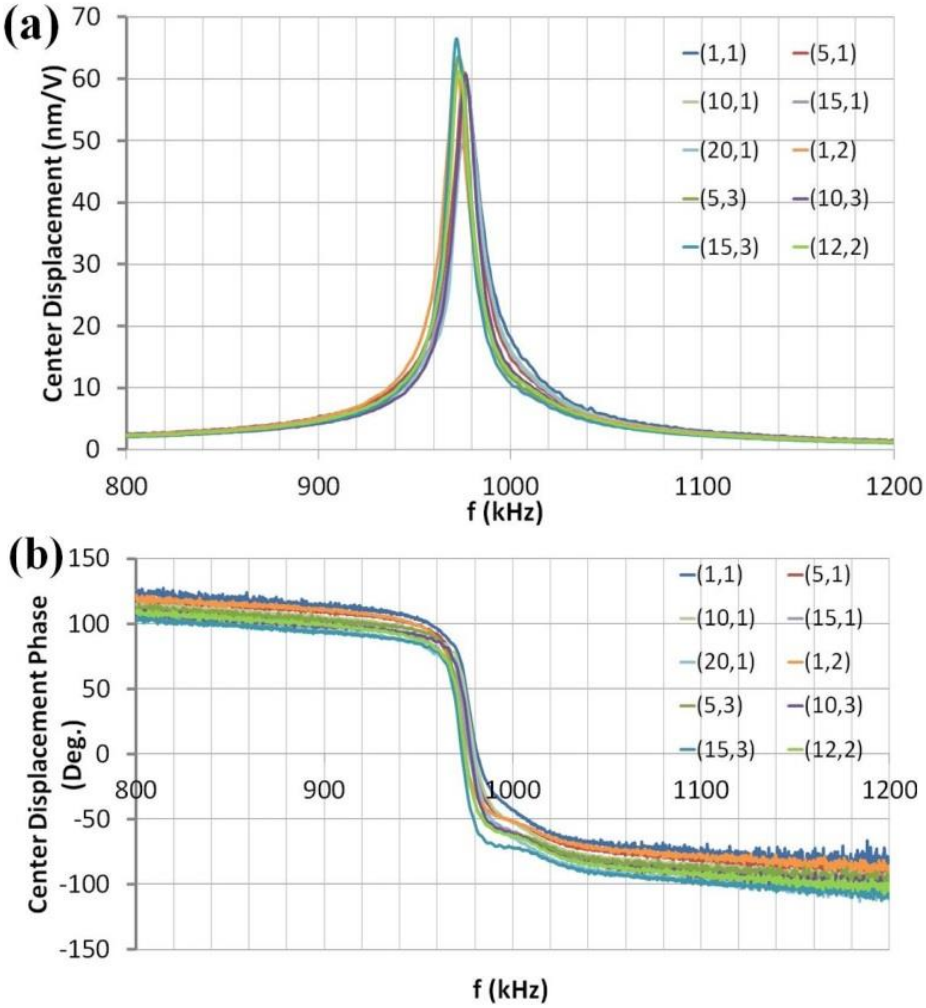

Fig. 3.3.2.3. Center displacement magnitude (a) and phase (b) with respect o to frequency of various DEB pMUT of a single-channel array from the prototype 27×6 DEB pMUT structure, measured using LDV under the inner electrode actuation scheme. The frequency response between the pMUTs from different locations of the array show very good consistency in terms of the resonant frequency, displacement magnitude, and phase angle.

3.4. Acoustic Response

3.4.1. Low-Voltage Measurements in Air and Water

The acoustic response of a single-channel 27×6 DEB pMUT array has been measured using a piezoelectric transducer (UZ250, Noliac) both in air and water. Figure 3.4.1.1a shows the axial pressure generated by the aforementioned array driven by 0.5 V_{pp} at 250 kHz in DI water as a function of the vertical distance under the inner-electrode driving scheme. The measured data is in good consistency with the theoretical model developed by our group for pMUT arrays and will be discussed in chapter 4 [24]. Data points measured at further distance are in better agreement with the theoretical model since the correct alignment between the pMUT array and the piezoelectric transducer becomes difficult as the pMUT array and piezoelectric transducer get closer to one another. Furthermore, approximations have been used in the theoretical model for the near-field region, which introduce additional estimation errors.

Figure 3.4.1.1b shows the received voltage amplitude by the piezoelectric transducer (V_{out}) as a function of the array driving voltage amplitude (V_{in}) at 250 kHz frequency in air. The distance between the array and the piezoelectric transducer is set to be 27 mm and the input voltage range is from 1.3 V_{pp} to 3.5 V_{pp}, which is suitable for battery powered handheld devices. The DEB pMUT array shows good linearity in the input voltage range of interest for such devices. Figures 3.4.1.1c and 3.4.1.1d show the measurement setups in water and air, respectively.

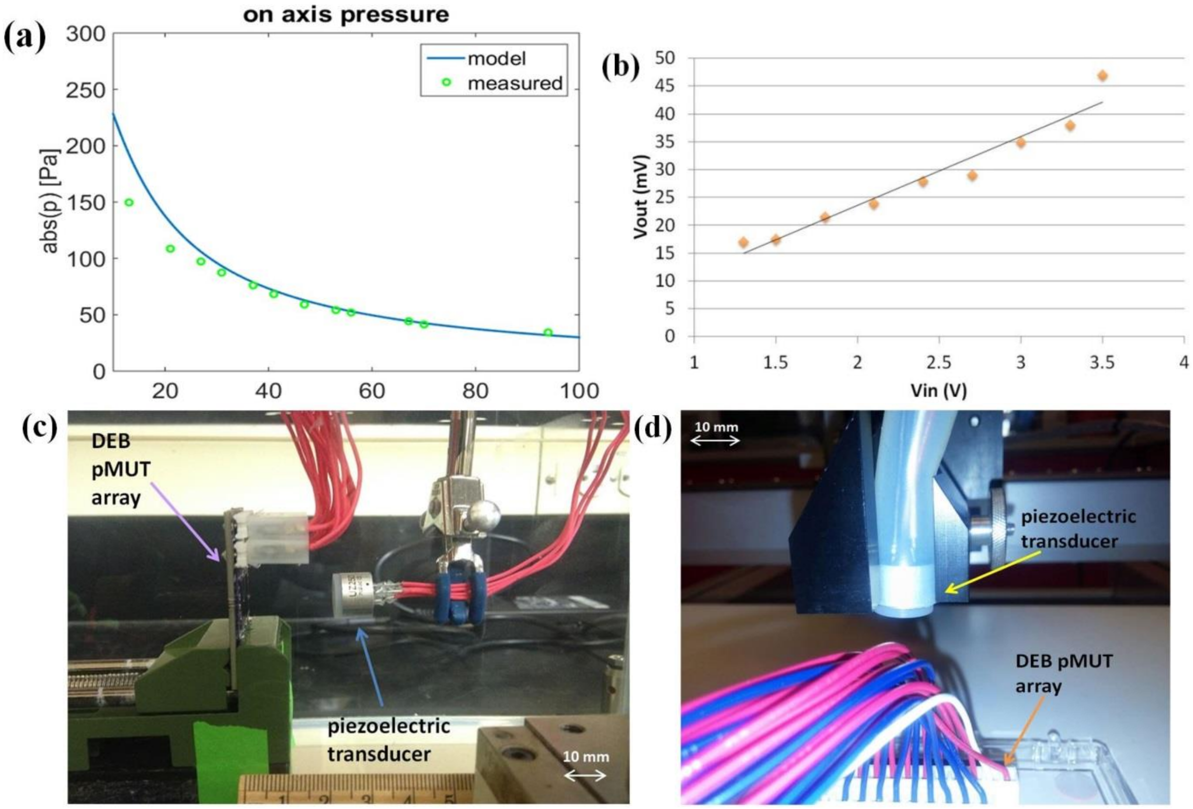

Fig. 3.4.1.1. (a) Measured axial pressure of a single-channel DEB pMUT array of 6×27 pMUTs driven with 0.5 V_{pp} at 250 kHz in water; (b) linearity of the pMUT array of (a) in air; (c) measurement setup in a water tank; (d) measurement setup in air.

3.4.2. Intensity Assessment for Therapeutic Ultrasound

Medical studies have shown that low-intensity pulsed ultrasound (LIPUS), with low acoustic intensities of less than 0.1 W/cm^2 (typically 30 mW/cm^2) can significantly increase cell differentiation and accelerate fracture healing [68-71]. For the purpose of implementation of the transducers in battery-powered handheld devices for therapeutic medical applications, the device must be capable of generating high enough acoustic intensity in the region of interest at low voltages. Here we have fabricated a single-channel 12×12 array of DEB pMUT with a total area of 7mm×7mm. Acoustic testing has been conducted in mineral oil with density of 0.8493 g/cm^3 and sound speed of 1440 m/s. The array has been driven differentially with +/- 2.5 V_{ac} on the inner and outer electrodes respectively. Figure 3.4.2.1a shows similar trends and reasonable agreement between the simulated and the measured axial pressure using a needle hydrophone (Y-120, Sonic Concepts, Inc.), and Fig. 3.4.2.1b is the simulated intensity field of the array under the same driving scheme. The discrepancy between simulation and experimental results is due to the negligence of the mutual coupling effects of the pMUTs in the simulation as well as fabrication uncertainties which are not incorporated in the model. The axial intensity of the array when driven differentially with +/- 5 V_{ac} is shown in Figure 3.4.2.1c, demonstrating that the array is capable of generating high enough acoustic intensity in the range of 30-70 mW/cm^2 up to 2.5 mm deep using voltages that are sufficiently low to be realizable in battery-powered handheld devices for therapeutic applications. The fabricated array has been measured to have the highest normalized acoustic intensity of 27 $\mu W/(\mu m^4)$ (at 1.5 mm away), as defined as $I_n = I/(VNd_{31})^2$, among all the reported pMUT arrays [72-76]. Here I is the acoustic intensity, V is the input voltage amplitude, N is the total number of pMUTs, and d_{31} is the piezoelectric charge constant. Since intensity is proportional to pressure squared, pressure is proportional to the effective volumetric velocity, and the effective volumetric velocity is proportional to VNd_{31}, such definition of normalized intensity is introduced so that pMUT arrays of different piezoelectric properties, driving voltages, and number of transducers can be compared only based on the individual pMUT design. Figure 3.4.2.1d is the measured pressure frequency response of a 6×60 DEB pMUT array in water showing extremely large bandwidth of the array. Large bandwidth is very important and is of high interest for medical applications that require various transmission operation frequencies or when the transmission and receiving frequencies of interest are far apart, such as harmonic imaging. The achieved large bandwidth here is due to the large size of the array formed of multiple pMUTs all driven simultaneously and can generate multiple resonant frequencies close to one another.

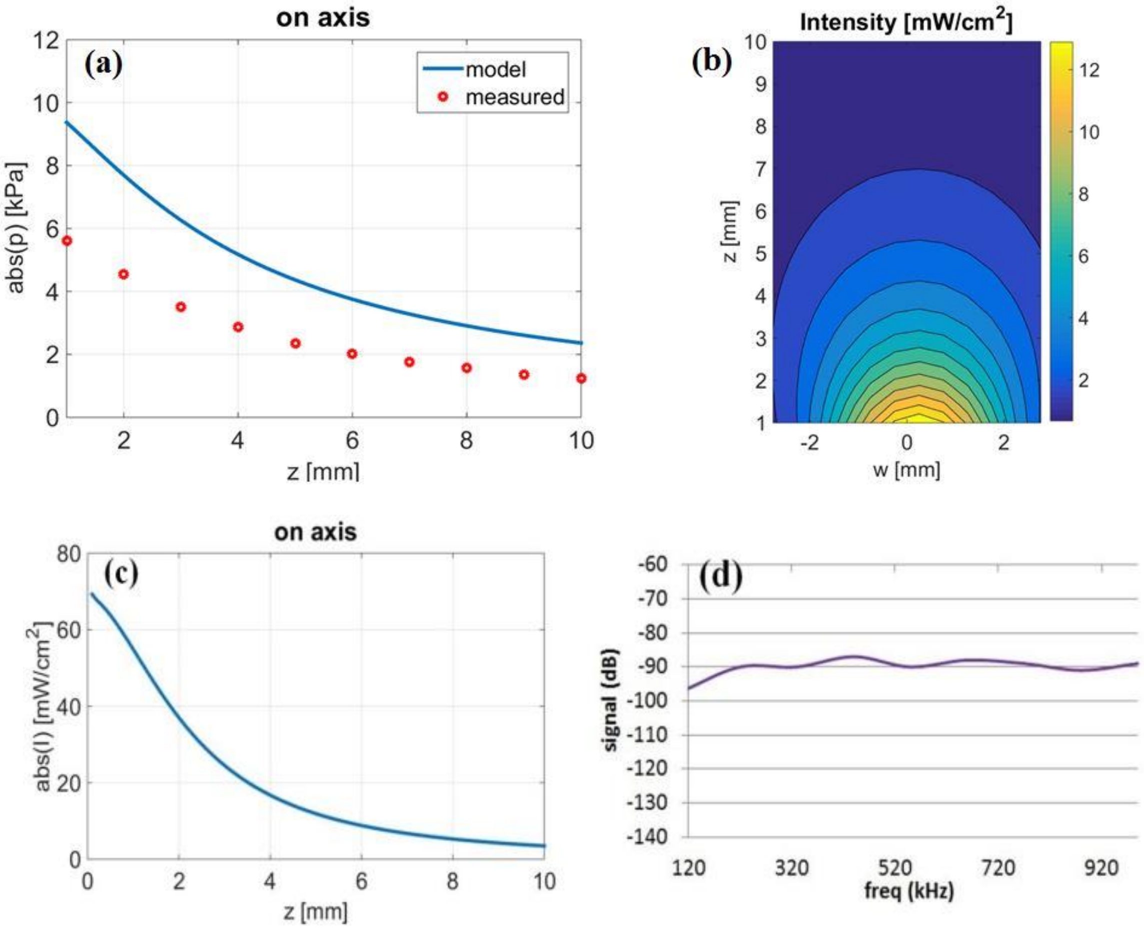

Fig. 3.4.2.1. (a) Measured and simulated axial pressure versus vertical distance and (b) 2D plot of the modeled intensity of the 12×12 array in oil tank driven under 2.5V AC differentially; (c) axial intensity driven differentially under 5Vac, showing desirable acoustic intensity up to 2.5mm penetration depth; (d) Bandwidth testing of a 6×60 single channel array, showing very high bandwidth of 1.2 MHz with a center frequency of 720 kHz.

3.5. Beamforming Using a Customized ASIC

In this section, a customized 1- to 8-ch scalable pMUT interface system designed and fabricated by our collaborator at Masdar Institute of Science and Technology, UAE, for portable 2D ultrasonic imagers is utilized for beamforming purposes. The ASIC Charge Redistribution TX can drive up ultrasonic transducers with up to 500pF/channel at a wide range from 100kHz to 5MHz while reducing the TX drive power by 30% [Ms. Judyta Tillak and Dr. Jerald Yoo, MIST, Abu Dhabi, UAE]. The on-chip adaptive beam-former supports 5 different media scans and has channel scalability as well as on-chip aberration compensation. This 8-ch system occupies and area of 700×1500µm with TX drives up to 6V while consuming 2.34µJ/scan.

3.5.1. ASIC Architecture and Results

Fig. 3.5.1.1 shows the architecture of the system which consists of an 8-ch AFE with TX, RX and a DBE where each AFE channel is equipped with a LNA and a digitally controlled

Time-Gain Compensation (TGC) amplifier. The AFE has a bandwidth from 100 kHz to 5 MHz and maximum gain of 60 dB to enable deep tissue scans (~100 mm) in high attenuation media, e.g. intracranial and transcranial imaging. Additionally, each AFE has a digitally controlled HV switch to shield LV receiver path from HV TX path from the pMUT ringing and crosstalk. The DBE performs pulse-to-echo sequence (P2E) and it supports 5 different medium types: air (343 m/s), rubber (926 m/s), alcohol (1143 m/s), water (1493 m/s) and bio-material (1533 m/s). The beam-former is capable of driving a phased-array from 1 to 8-channels with element separation of 250 μm – 5 mm (for 8-ch mode), or 1.5 cm (for 4- or 2-ch mode). The time resolution is ~20ns and the spatial resolution depends on the medium, e.g. lateral resolution = 60 μm in water. The proposed TX only occupies 300 × 300 μm per channel, which leaves room for future vertical integration of IC and pMUT. For higher frequency scan the resolution is typically higher, but at the cost of weaker acoustic power. The primary P2E sequence is designed to scan with +30°/-30° field and depth from -2.5 to 10 cm using 1 TX driver per channel. The same medium can be scanned also with 2 or 4 TX drivers per channel if more acoustic power is needed.

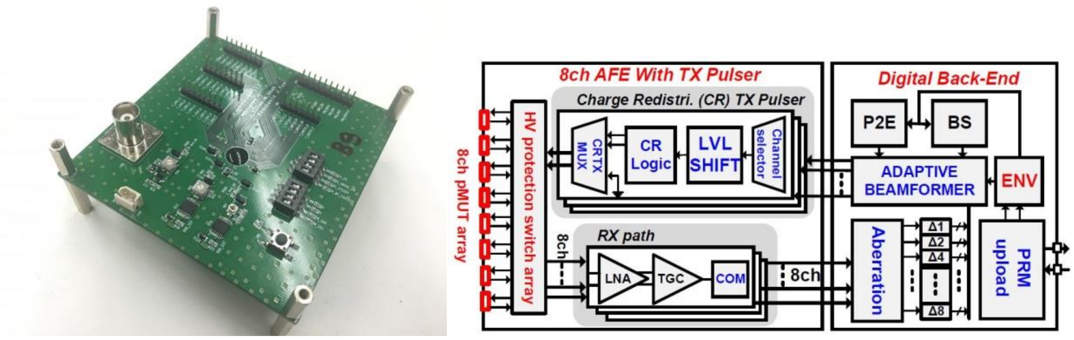

Fig. 3.5.1.1. 1- to 8-ch ASIC (a) and its block diagram (b).

A 4-channel, 1D DEB pMUT array with 180 (6×30) DEB pMUTs per channel as those presented in 3.2 has 2.3 mm in channel pitch. Figure 3.5.1.2a shows the lateral pressure profile of the DEB pMUT array captured by the ultrasonic transducer at the axial distance of 19 mm away from the DEB when the channels are driven separately (dashed curves) and when all the channels are driven altogether (solid curve). Channels 1, 2, and 4 were driven through their outer electrodes while the inner electrode was grounded and channel 3 was driven through its inner electrode while the outer electrode was grounded. Due to fabrication issues there were driving sensitivity variations among the channels. Thus, in order to achieve the same pressure level from each channel, channels 1, 2 and 4 were driven with 3 Vpp input voltage while channel 3 was driven with 1.79 Vpp input voltage all at 250 kHz. Figure 3.5.1.2b shows the measured lateral pressure of the same array under the same conditions when all the channels are driven with (dashed) and without (solid) the focusing scheme with the axial distance of 19 mm. It can be observed that the focusing scheme can suppress the side lobs and increase the peak pressure, in this case by a factor of 1.2.

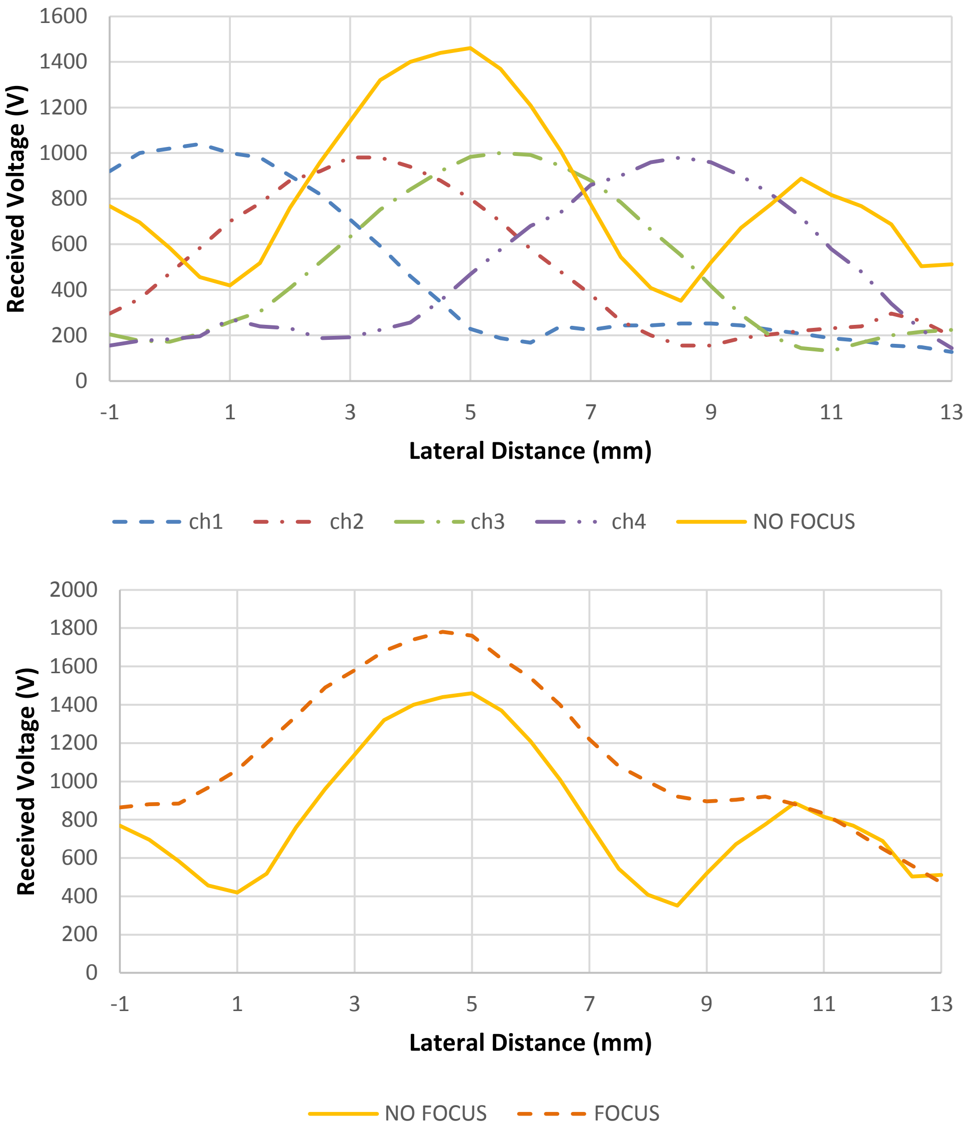

Fig. 3.5.1.2. (a, top) Measured lateral pressure profile of the DEB pMUT array at the axial distance of 19 mm when each channel is driven separately and when all the channels are driven altogether with no focusing scheme; (b, bottom) Measured lateral pressure when all 4 channels are driven with and without focusing scheme.

Asymmetries among the array elements or inhomogeneity of the media result in significant errors of the conventional method in fractional delays calculation based on the constant Time-of-Flight (ToF) assumption. Such unknown speed variance results in phase aberration that causes image blurriness, loss of contrast and reduction of resolution. The aberration compensation circuit shown in Fig. 3.5.1.3 corrects the phase inequalities related to element-to-element variations and velocity distribution in a test volume. The aberrated plot (Fig. 3.5.1.4) shows the measured acoustic pressure profile at the axial distance of 19 mm shifted with respect to the intended center of the array due to incorrect delay introduced to one of the channels (error e = +1µs for channel 1). If uncompensated (aberrated), 44% of acoustic signal is lost at the point of interest (i.e. center of the array) and a 2.5 mm offset occurs at the target focal point. After the compensation, we can observe the acoustic pressure successfully focuses at the center of the array.

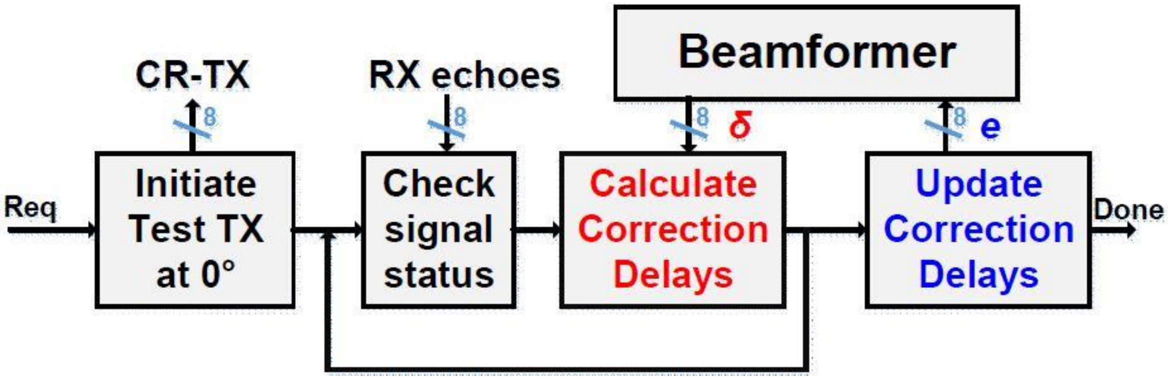

Fig. 3.5.1.3. ASIC aberration compensation block diagram.

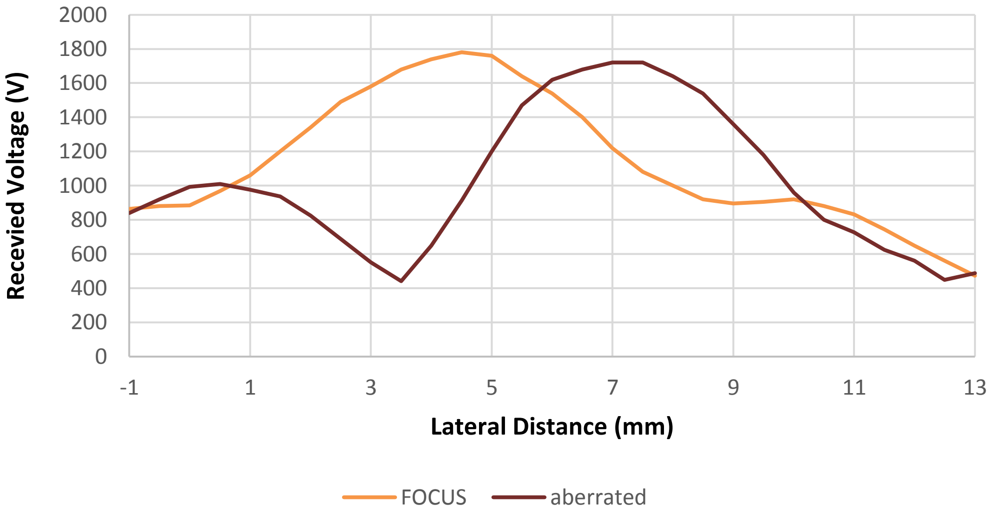

Fig. 3.5.1.4. Measured lateral pressure at the axial distance of 19 mm with and without aberration on channel 1.

In conventional TX driving, the GROUND electrode of the transducer is connected to GND, while the DRIVING electrode oscillates between ground and driving voltage or HV shaped pulse which results in significant power consumption [49], [51]. On the other hand, in the proposed CR-TX, the DRIVING electrode is primary charged with VDDH, while the GROUND electrode is connected to the GND. In the discharging mode, the DRIVING and GROUND electrodes are shorted to each other which ideally recycle half of the charge at each driving cycle. The pMUT device is represented as capacitive load. With an equal electrode size and negligible leakage, the charge redistributes quickly and causes the both electrodes to have a voltage close to VDDH/2. In the next charge mode, instead of charging up from GND to VDDH (full VDDH swing), each electrode charge/discharge by VDDH/2; therefore half of the initial charge from the load capacitance is recycled for next charge cycle. The differential voltage over DRIVING and GROUND electrodes remains the same and the CR-TX results in similar acoustic power to the conventional driving method. Note that the larger the load, the more power TX will consume. The achieved average measured power reduction was 30% comparing to the conventional driving method. In the ideal case, when both electrodes are equal size and no leakage occurs the total driving power is reduced by 49%. The discrepancy is primarily caused by unmatched pMUT elements in both electrode size and other sources of charge loss.

3.6. Conclusion

We have successfully fabricated single-transducers as well as various arrays of DEB pMUT for both air- and liquid-coupled applications. Both analytical simulations and experimental measurements have shown that the energy efficiency and drive sensitivity of the DEB transducer can be 4X those of the state-of-the-art single-electrode unimorph pMUT. New fabrication techniques have been utilized for the development of the prototype devices with excellent crystal quality of AlN layers and good manufacturing yield. Experimental results match well with analytical and simulation results. Furthermore, a liquid-coupled array have shown the highest normalized acoustic intensity, $I_n = I/(VNd_{31})^2$, and the measurement results show that the devices can be potentially used in low-voltage handheld medical ultrasonic devices.

Table 3.6.1 The material properties used in the analysis and simulations [22]

Parameter	**Description**	**Value**	**Unit**
ρ_{AlN}	AlN density	3300	Kg/m^3
$Y_{0\text{-}AlN}$	AlN Young's modulus	348	GPa
v_{AlN}	AlN Poisson's ratio	0.30	
$d_{31\text{-}AlN}$	AlN Piezoelectric charge constant	2.20	pm/V
ε_{AlN}	AlN Dielectric constant	10.26	
ρ_{Mo}	Mo density	10220	Kg/m^3
$Y_{0\text{-}Mo}$	Mo Young's modulus	329	GPa

Chapter 4

Equivalent Circuit Models for PMUT Arrays

4.1. Introduction

In the previous chapters the exact solutions for circuit parameters in the electromechanical domain, such as: mechanical admittance, input electrical impedance, and electromechanical transformer ratio were analytically derived. In this chapter, the equivalent circuit models of large arrays of curved (spherical-shape) and flat Piezoelectric Micromachined Ultrasonic Transducers (pMUTs) are derived for complex pMUT arrays design and analysis. By utilizing the array solution methods previously established for the thickness-mode piezoelectric devices and Capacitive Micromachined Ultrasonic Transducers (cMUT), single pMUT circuit model can be extended to models for array structures. The array model includes both the self- and mutual-acoustic radiation impedances of individual transducers in the acoustic medium. Volumetric displacement, induced piezoelectric current, and pressure field can be derived with respect to the input voltage matrix, material and geometrical properties of each individual transducer and the array structure. As such, the analytical models presented here can be used as a guideline for analyses and design evaluations of large arrays of curved and flat pMUTs efficiently, and can be further generalized to evaluate other pMUT architectures in the form of single-devices or arrays.

4.2. Array Analyses and Models

PMUTs are typically micron-size devices with dimensions smaller than the wavelength at the operation frequency such that they can be treated as point sources when operating individually. In general, it is necessary to have an array of transducers to create a certain beam shape with specific beam width, near field-far field crossover point, and high enough acoustic power for most practical applications. Furthermore, by performing electronic beam steering/focusing, the lateral resolution as well as the peak pressure level can be enhanced [4]. While the array structures offer substantial performance improvements, current commercial software has the following difficulties in performing pMUT array simulations: 1) some of them use an analytical approach to solve the acoustic field pattern only and are incapable of combining multi-physics of such an intricate system (i.e electrical to mechanical and to acoustical domains for pMUT arrays), and it is typically assumed that the motion of transducers can be well-defined according to the electrical input to each individual element and the displacements can be set as known boundary conditions [52, 53]; 2) some FEM software is capable of combining different physical models, but requires burdensome computation time and memory for them to solve a large array of transducers [54, 55].

Therefore, it will be very valuable to have a theoretical model and solver to address issues associated with large numbers of pMUT transducers for array design purposes.

Figure 4.2.1 shows a 3D schematic of a pMUT array illustrating the geometrical parameters of the array, where (*m*,*n*) is the index of an element located in row number *m*, and column number *n*, $\overrightarrow{d_i}(m,n)$ is the position vector of element (*m*,*n*) relative to the array central element, $\vec{r}$ is the position vector of point (r,θ,ϕ) relative to the central element of the array, and $\vec{r_i}(m,n)$ is position of an arbitrary point (r,θ,ϕ) in the medium relative to the pMUT (*m*,*n*).

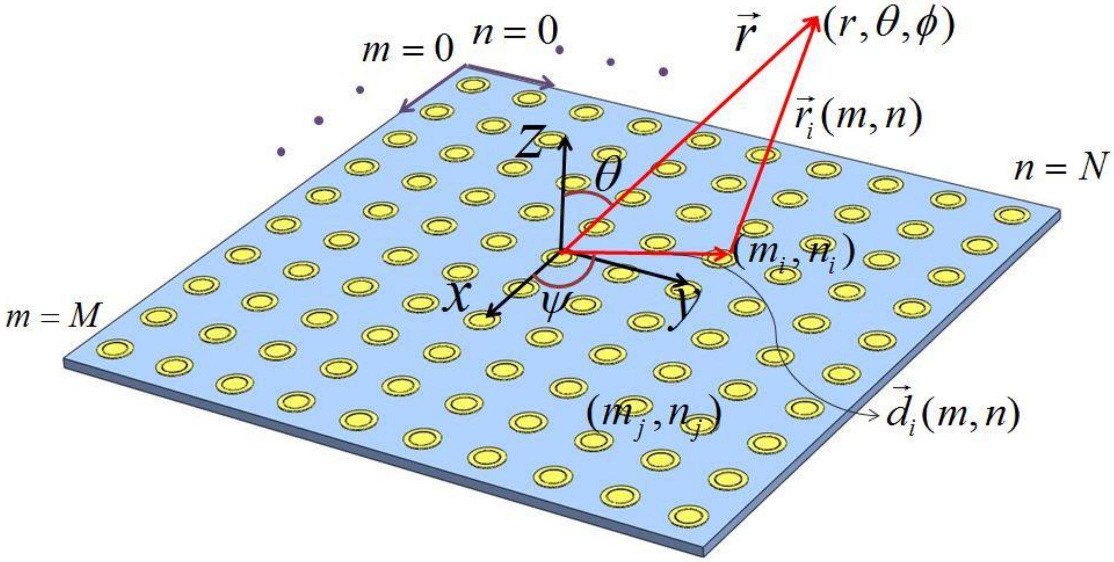

Fig. 4.2.1. 3D schematic of a pMUT array showing the geometrical parameters.

$$\vec{d}_i(m,n) = (m-m_c)L\vec{e}_x + (n-n_c)D\vec{e}_y \tag{4.2.1}$$

$$\vec{r} = r\sin(\theta)\cos(\phi)\vec{e}_x + r\sin(\theta)\sin(\phi)\vec{e}_y + r\cos(\theta)\vec{e}_z \tag{4.2.2}$$

$$\begin{aligned}\vec{r}_i(m,n) = &\left\{r\sin(\theta)\cos(\phi) - (m-m_c)L\right\}\vec{e}_x + \left\{r\sin(\theta)\sin(\phi)\vec{e}_y - (n-n_c)D\right\}\vec{e}_y \\ &+ r\cos(\theta)\vec{e}_z\end{aligned} \tag{4.2.3}$$

where (m_c,n_c) is the coordinate of the central element, *L* and *D* are the element pitches in the *x* and *y* directions respectively and they are assumed to be constants in the entire array for this analysis for simplicity but can also be treated as variables, and r_i is the distance between the central element and point (r,θ,ϕ) in the medium.

4.2.1. Array Circuit Equations

Figure 4.2.1.1 shows the equivalent circuit representation of a pMUT array which parallels circuit modeling representations that have previously been reported for thickness-mode piezoelectric arrays [4] and the cMUT arrays [57, 60]. The material properties and specific geometrical dimensions of the curved and flat pMUTs are listed in Table 4.3.1 and Table

4.3.2. The circuit is made up of the electromechanical equivalent parameters of individual elements as well as the acoustic impedance matrix, which models the interaction of the pMUT elements directly with the acoustic medium and with one another through the acoustic medium. In the figure, V_{inJ} is the voltage between the electrodes of pMUT number J, C_{0J} is the feedthrough capacitance, η_J is the electromechanical transformer ratio, v_{vol_J} is the volumetric velocity, Z_{mJ} is the mechanical impedance, Z_J is the input mechano-acoustical impedance, and P_{I_J} is the incidence pressure of the J'th pMUT element. Furthermore, $[Z_a]_{ij}$ is a $N_{tot}\times N_{tot}$ matrix that represents the self- and mutual-acoustic impedances between the transducers, where $N_{tot}=M\times N$ is the total number of transducers in the array.

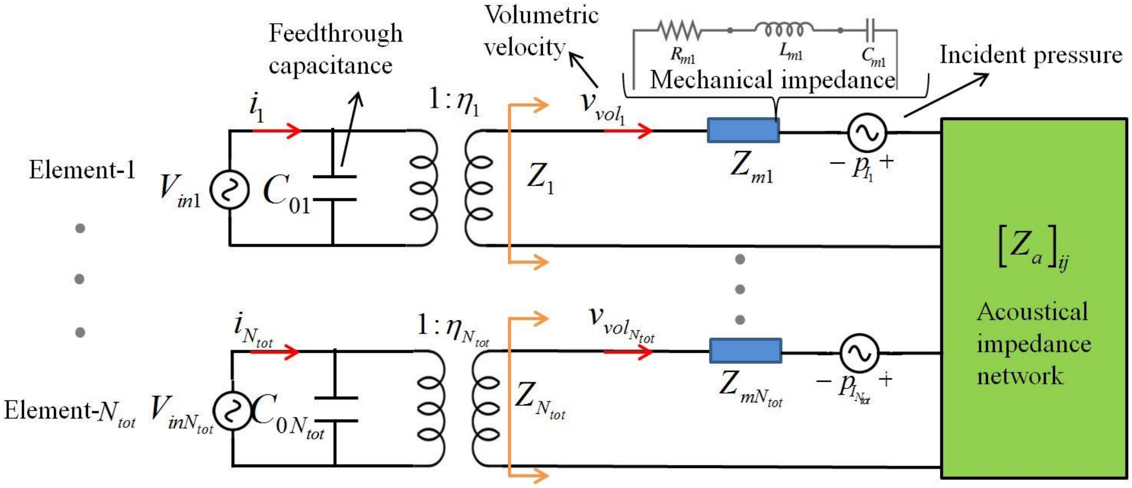

Fig. 4.2.1.1. Equivalent circuit model for the pMUT array. Different elements can be driven separately, but they can interact with one another through the acoustic domain, modeled as an acoustic impedance matrix which consists of self and mutual radiation of the elements.

The input mechano-acoustical impedance of the i^{th} pMUT, Z_i, is the summation of the mechanical impedance Z_{mi}, the self-radiation impedance, Z_{ii}, and the mutual impedances Z_{ij} as [4]:

$$Z_i = Z_{mi} + Z_{ii} + \sum_{\substack{j=1 \\ i\neq j}}^{N_{tot}} \frac{v_{volj}}{v_{voli}} Z_{ij} = Z_{mi} + \sum_{j=1}^{N_{tot}} \frac{v_{volj}}{v_{voli}} Z_{ij} \tag{4.2.1.1}$$

The mechanical and self-radiation impedances (i.e. Z_{mi} and Z_{ii}) are introduced and expressed analytically in previous sections. For example, the mechanical admittance is explicitly derived and shown in Table 4.3.3 for a clamped curved pMUT with spherical-shape diaphragm. The self-radiation acoustic impedance is expressed in an integral form in Eq. (2.5.4) with its value calculated for clamped curved pMUT by substitution of Eq. (2.5.1) to (2.5.3) into Eq. (2.5.4). In this notation, $Z_{ii}=Z_s$ for clamped spherical curved pMUT.

The self-radiation impedance for a curved pMUT can also be estimated from the radiation impedance of a flat piston moving in a rigid baffle, assuming that the shell center depth from the baffle plane is negligible comparing to the transducer diameter, or in other words, the radius of curvature of the spherical cap is much larger than its physical dimensions [67].

$$Z_{ii} = k_{c1}(\rho C / (\pi r_{eff}{}^{2}))\left[1-(2/\gamma)J_1(\gamma)+(4/\pi)\int_0^{\pi/2}\sin(\gamma\cos(x))\sin^2(x)dx\right] \qquad (4.2.1.2)$$

where C is the speed of sound, r_{eff} is the effective radius of the diaphragm and can be approximated as $r_{eff} \approx a/\sqrt{3}$, $\gamma=2\omega r_{eff}/C$ for clamped pMUT, J_1 is the Bessel function of the first kind of the first order, and k_{c1} is a correction factor which turned out to be ≈0.82 for the case of a spherical clamped diaphragm and is 1 for flat disk-shape diaphragm.

Any of the Eq. (2.5.4) or (4.2.1.2) can be used to evaluate the self-radiation impedance of pMUT, but the choice depends on the requirement on the accuracy of the data according to the given geometry. For instance, Eq. (4.2.1.2) is only a good estimation for shallow curved pMUT, but Eq. (2.5.4) is the most general form despite the fact that it requires numerical integration.

The mutual radiation impedance comes from the interaction of the pMUT elements with each other through the acoustic environment and can be expressed as a function of the wave number, k, the transducer radius, a, and the center-to-center distance between the elements, d [4]. The mutual radiation impedance causes the volumetric displacement of the individual element not to be a direct function of its applied voltage and distorts the displacement amplitude and the phase. It also impacts the system to produce multiple resonant frequencies and generally increases the system bandwidth but reduces the average volumetric displacement of each element. Here, the mutual radiation impedance equation in the flexural mode can be derived similar to the prior works in [57] & [58] for clamped disk type radiator elements by assuming that the curved pMUT is “shallow” (i.e. the center depth is much smaller than the radius ($g<<a$)):

$$Z_{ij} = k_{c2}\frac{9\rho C}{5\pi a^2}A(ka)\frac{\sin(kd)+j\cos(kd)}{kd} \qquad (4.2.1.3)$$

where d is the distance between the two elements, and k_{c2} is a geometrical correction factor which is 1 for a flat pMUT and is assumed to be 1 for shallow curved pMUTs as well, but is less than 1 for concave pMUTs when g is comparable to a. It can be observed that Z_{ij} is a descending function of the normalized distance between the two elements, kd, and the real and imaginary parts fluctuate sinusoidally as a function of kd and are 90^{o} out of phase. The function “*A”* can be modeled as a polynomial and is estimated to 10 orders in [57], and is a function of geometry relative to the wavelength.

In the transmission mode, the volumetric velocity of each pMUT needs to be solved which can be calculated by the KVL equations for circuit model presented in Fig. 4.2.1.1, with known input voltages. The induced current can also be found from the KCL equations at the nodes connecting the inputs to the blocked capacitance and the electromechanical transformer. Similar to the methods used for the thickness mode piezoelectric transducer arrays [4] and cMUT arrays [60], the equivalent circuit KVL and KCL equations can be written as:

$$\eta_i V_i = Z_i v_{voli} = Z_{mi} v_{voli} + \sum_{j=1}^{N_{tot}} v_{volj} Z_{ij} \qquad (4.2.1.4)$$

$$i_i = \eta_i v_{voli} + Y_{0i} V_i \tag{4.2.1.5}$$

Furthermore, the volumetric velocity matrix can be written in a matrix-form equation as:

$$v_{vol_{N_{tot}\times 1}} = \left\{ I_{N_{tot}\times N_{tot}} Z_{m_{N_{tot}\times 1}} + Z_{a_{N_{tot}\times N_{tot}}} \right\}^{-1} \mathrm{diag}\left(\eta_{N_{tot}\times 1} V^{T}_{1\times N_{tot}} \right) \tag{4.2.1.6}$$

Now the pressure can be calculated at any arbitrary point in the field by superposing the pressure generated by each pMUT of the array [4]:

$$p(r,\theta,\phi) = \sum_{n=1}^{N}\sum_{m=1}^{M} p_i(m,n) = \sum_{n=1}^{N}\sum_{m=1}^{M}\left(\frac{j\rho c k v_{voli}}{2\pi} dir(\theta,\phi) \frac{e^{-jkr_i(m,n)}}{r_i(m,n)} e^{jk\mu_{mn}} e^{j\omega\tau_{mn}} \right) \tag{4.2.1.7}$$

where $dir(\theta,\phi)$ is the directivity function of each element, which can be assumed to be 1 if $ka<<1$ as is valid for most pMUT designs, and μ_{mn} and τ_{mn} are the steering and focusing factors for element (m,n) tuned electronically by phase variation of input voltages. It is noted that μ_{mn} can be interpreted as the difference between the normal distances to a plane located at a certain orientation relative to the array plane from elements (1,1) and (m,n) that the radiated waves must travel before they reach the plane. In other words, when the radiated beam is to be steered to a certain orientation (θ_0,ϕ_0), certain phase delays are applied that correspond to the differences between the distances the emitted waves from the elements must travel to form a flat wave propagating in the (θ_0,ϕ_0) direction.

$$\mu_{mn} = -((m-1)L\sin(\theta_0)\cos(\phi_0) + (n-1)D\sin(\theta_0)\sin(\phi_0)) \tag{4.2.1.8}$$

τ_{mn} is the time delay for element (m,n) when the beam is to be focused on a specific point with a certain distance from the array. Similarly, it is associated with the emitted wave path differences between the element (m,n), and the central element (m_c,n_c). For example, if the focal point is set at z_f and the 1D focusing is conducted by applying phase delays along the rows of Fig. 4.2.1, then:

$$\tau_m = \left[L\left(m_c - m\right) \right]^2 / (2z_f c) \tag{4.2.1.9}$$

4.2.2. Array Simulation Results

Both curved pMUT and flat pMUT arrays of 32×32 elements, with 460 µm element-pitch are used as the modeling examples. The curved pMUT elements are made of aluminum nitride with thickness of 1 µm, diameter of 120 µm, and radius of curvature of 650 µm, and resonant frequency of 0.97 MHz while the flat pMUT elements have the same diameter as well as the similar natural frequency of 0.97 MHz (in water) with aluminum nitride thickness of 500 nm and silicon thickness of 2.3µm. The top electrode coverage for the flat pMUT elements are 70% of the diaphragm total diameter so that the input electrical energy for both the curved and the flat elements are equal if the same input voltages are applied. The applied voltage amplitudes are kept at 10 Vac for all the elements for both models and the driving frequency is 1.1 MHz unless otherwise specified. Water is chosen as the medium of operation for both models. The mechano-acoustical impedance matrix is calculated from Eq. (4.2.1.1), including the derivations of the mechanical impedance from the single pMUT equivalent circuit model, self-radiation impedances, and mutual-radiation impedances between each and every two elements. The equivalent circuit parameters and their theoretical expressions for both curved and flat pMUT arrays are listed in Table 4.3.3. The $N_{tot} \times N_{tot}$ mechano-acoustical matrix has $N_{tot}(N_{tot}+1)/2$ independent elements. From the impedance matrix, and the given voltage matrix, the elements' volumetric velocity and displacement can be calculated according to Eq. (4.2.1.6). Figure 4.2.2.1 shows the mesh plot of volumetric displacement amplitude and phase for the curved pMUT array versus the location of the elements when all the elements are actuated with the same voltage and phase. The difference in displacement amplitudes and phases of elements can be seen, although they are all actuated by the same voltage. This phenomenon is due to the existence of the mutual impedances and interaction of the elements with one another through the medium which is a function of the elements' relative distances for a given frequency and the transducer geometry [4, 57]. For example, it is observed that the elements at the corners and edges of the array typically have more displacement phase variations from the average comparing to the central elements since the outer elements are more isolated and have less mutual interactions with other elements and have more different boundary conditions than the central elements. As a result, for design purposes, such phase variations must also be taken into account along with the displacement amplitude and distance of every element from the point of interest in the medium. Appropriate information about the phase also enables us to design a desirable phase delay algorithm by considering such natural phase variations between the elements and accounting for their effects in beam steering [4].

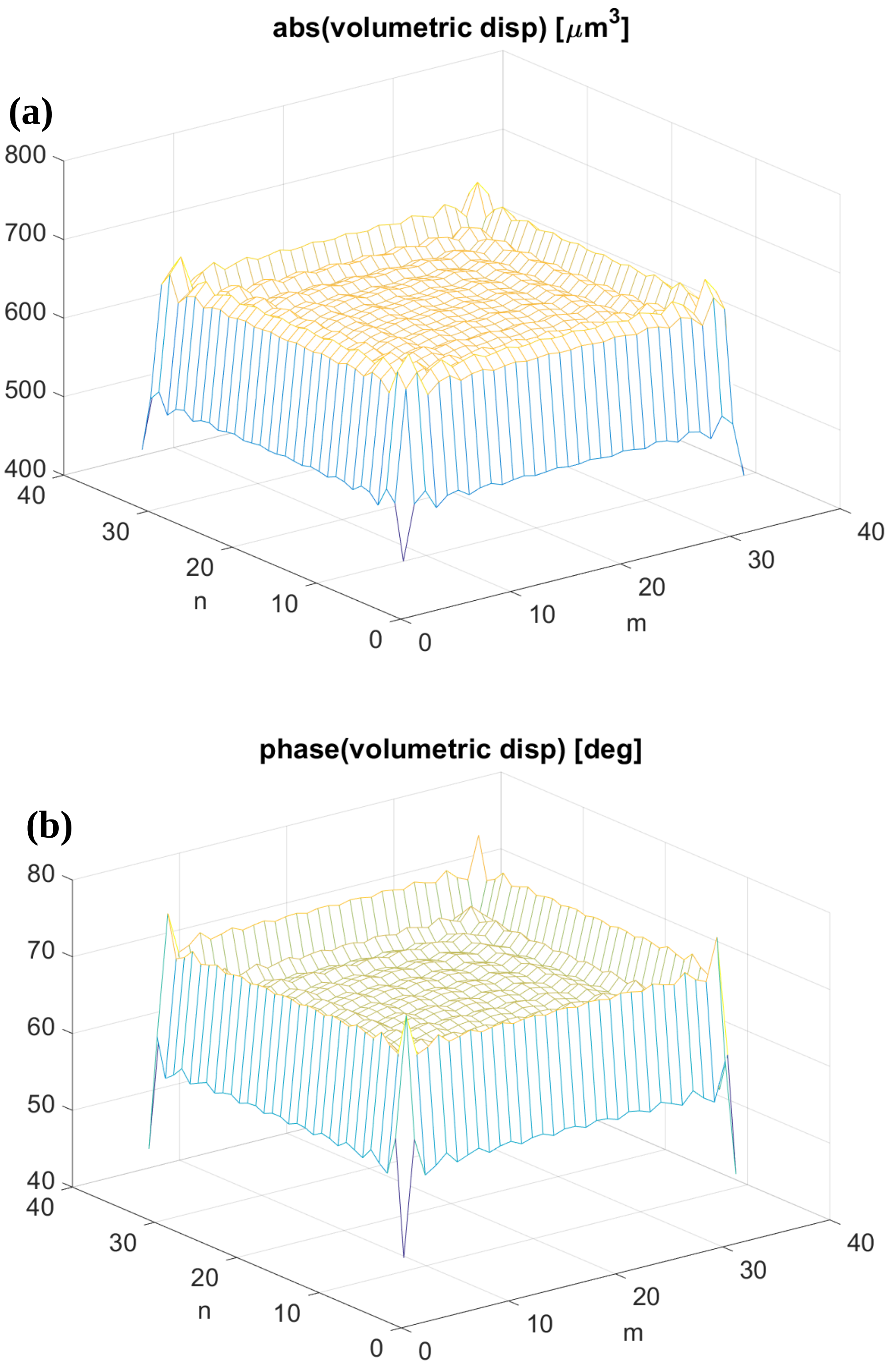

Fig. 4.2.2.1. 3D plot of the volumetric displacement amplitude (a) and phase (b) of the elements of the model curved pMUT array.

Figure 4.2.2.2a shows the axial acoustic pressure when all elements are driven in-phase for the curved- and the flat-element pMUT array, while Fig. 4.2.2.2b shows the lateral acoustic pressure at a vertical distance 40 mm away from the arrays. From Fig. 4.2.2.2a, it is observed that the crossover point between far field and near field is located at 48 mm away from the arrays. In the case of a continuous piston transducer with dimensions $(ML+2a)\times(ND+2a)$ which is equal to ~14.9×14.9 mm in this example, the far field and near field edge is located at $a_{piston}^2/\lambda=(14.9/2)^2/1.36=$ 41 mm which is close to the simulated value of 52.5 mm. The 22% difference is due to the fundamental differences between the pMUT array and the continuous piston radiator, including discontinuity of the pMUT array, and different modes of operation. It is also be noted that in the near field region, the axial field varies rapidly with distance due to the alternative constructive and destructive superposition of the radiated waves from different elements. Theoretically, this is mainly due to the phase factor, $kr_i(m,n)$, variations in Eq. (4.2.1.7) [5]. In the near field region, $r_i(m,n)$ is a strong function of the element location in the array, i.e. $(m\text{-}m_c)L$ and $(n\text{-}n_c)D$ in Eq. (4.2.3), which causes the element contributions to add in-phase or out-of-phase. However, in the far field region, $r_i(m,n)\sim r$, thus all the element contributions add constructively. In this region, smooth pressure decrease with respect to distance is observed as a function of $\sim 1/r$ [5]. From Fig. 4.2.2.2b, it can be observed that the pressure level for the curved pMUT array is ~2.9 times higher than the flat pMUT array. By using the 1D phase delay focusing scheme using Eq. (4.2.1.9), it is observed that the main lobe peak pressure amplitude is higher under the beam focusing scheme with narrower beam width and suppressed side lobes for both curved and flat pMUT arrays as expected [4, 23]. For the curved pMUT array example, it is observed that without the focusing scheme, the main pedestal secondary lobe is -2.8 dB and the first side lobe is -9.7 dB lower than the peak value, respectively. However, by applying the focusing scheme, the secondary lobe of the main pedestal becomes separated from the main lobe and is -11.9 dB below the peak value while the originally first side lobe is suppressed to -16.4 dB below the peak value. The 6 dB-beam width also has a 65% reduction using the focusing scheme. Phased delay focusing is a very common method for lateral resolution enhancement.

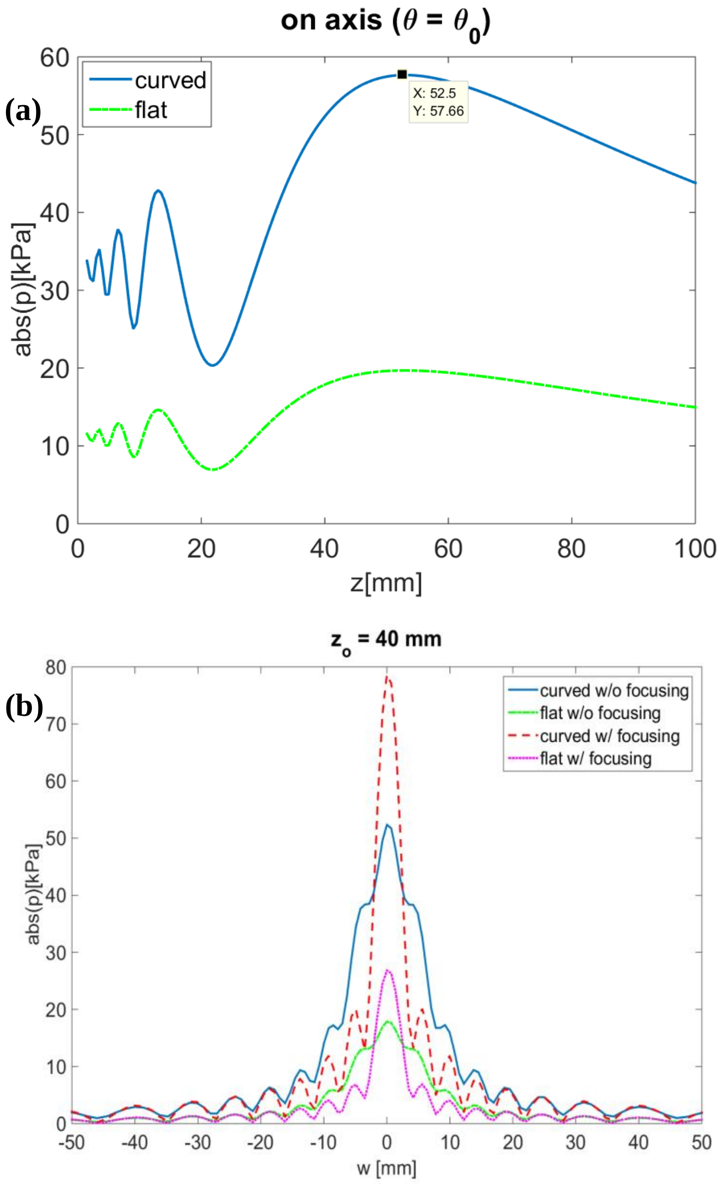

Fig. 4.2.2.2. (a) Pressure for both curved and flat pMUT arrays. (b) Beam profile at z = 40 mm for both arrays, with and without electronic focusing at z = 30 mm.

Figure 4.2.2.3 is the acoustic pressure versus the azimuthal angle, θ, at the radial distance of 40 mm away from the arrays' center. Figure 4.2.2.3a shows the pressure profile with and without the focusing scheme for the steering angle of θ_0=0 for both curved and flat pMUT arrays, and the steering angle is set to θ_0=30° for Fig. 4.2.2.3b.

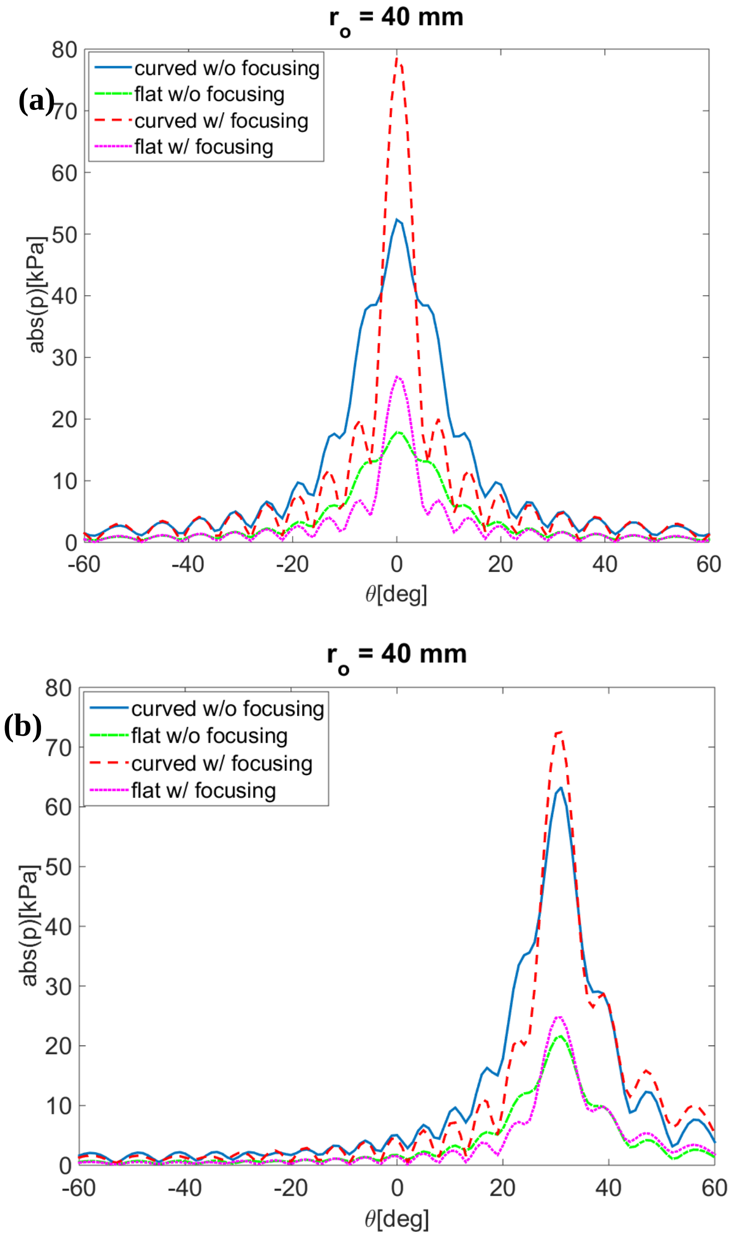

Fig. 4.2.2.3. Acoustic pressure versus the azimuthal angle at radial distance of 40 mm for the pMUT array models for (a) θ_0=0, and (b) θ_0=30^o.

The focusing distance was chosen to be 30 mm away from the array. It is observed that the curved pMUT array can generate higher pressure level comparing to the flat pMUT array. Furthermore, the electronic focusing helps to increase the main lobe pressure amplitude, reduce the beam width, and consequently enhance the SNR and lateral resolution, respectively [4]. These results also demonstrate the capability of the developed model for beamforming application, which is important for array designs such as the arrays used in the ultrasonic imaging applications by performing electronic B-mode sector scan for 2D image formations.

Figure 4.2.2.4 shows the acoustic pressure contour plots using curved pMUT arrays as the example for (a) without, and (b) with the phased delay focusing scheme with focal distance of z = 30 mm. The beam pattern is mainly a function of the array geometry as well as the wavelength. The pressure level at each point of the medium is determined by the volumetric displacement of the elements, frequency, and distance of the point from the array elements. It is noted that the focusing scheme will increase the pressure level and shrink main lobe width. It is important to design the array geometry and pMUT element properties (e.g. resonant frequency and electromechanical properties) according to the required design specifications of the array, such as: frequency of operation, bandwidth, depth of interest, beam width, and the pressure level, and the models developed here can provide accurate and efficient results to model pMUT arrays.

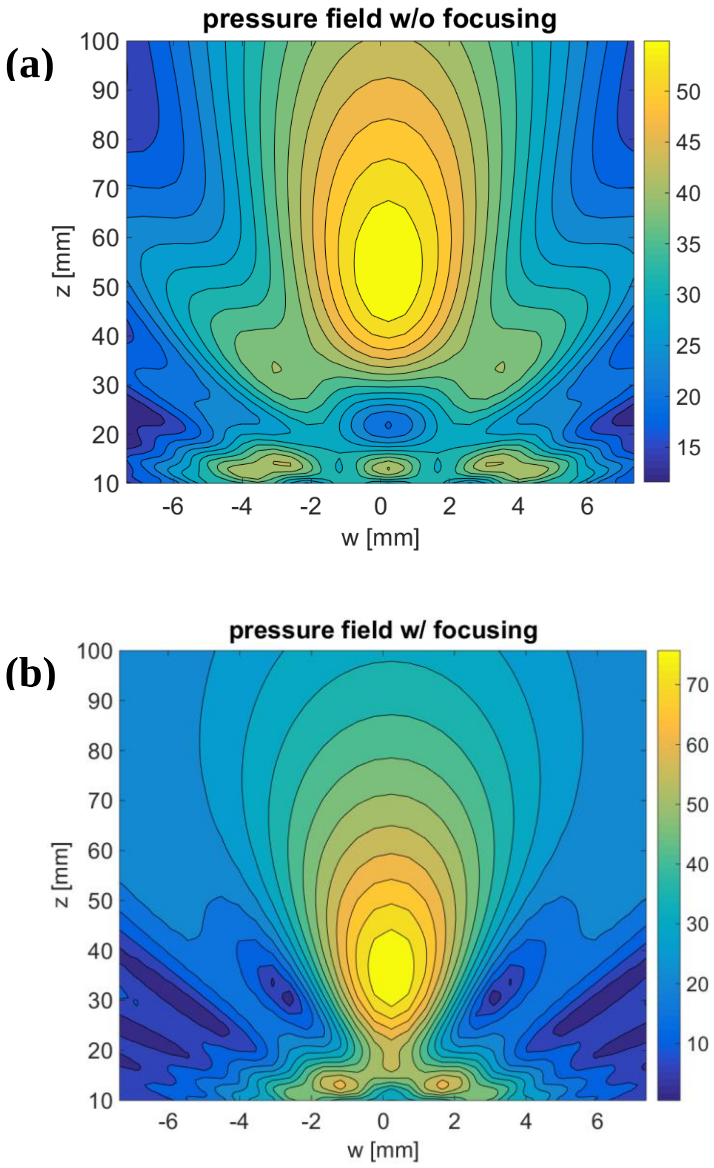

Fig. 4.2.2.4 Acoustic pressure contour plot of the curved pMUT array (a) without and (b) with phased delay focusing at 30 mm away from the array.

The overall performance of the whole array relies not only on the performance of each of individual transducers, but also on the system architecture and the configuration of the transducers [4]. It is also important to note that the frequency response of each of the transducers is different when it operates in the setup of an array or in the setup of an individual transducer, due to the mutual interactions between the elements and variations of the boundary conditions of each transducer from a single-transducer model [4, 57]. The neglect of the mutual effects could cause substantial inaccuracy in the simulations. For example, as shown in Fig. 4.2.2.5, if the mutual impedances of the example array operating at 1 MHz are set to zero, i.e. the impedance matrix in Eq. (4.2.1.1) becomes diagonal with only nonzero self-radiation impedance values, then the simulated pressure magnitude is 2.6 times higher than that when the mutual impedances are incorporated in the model.

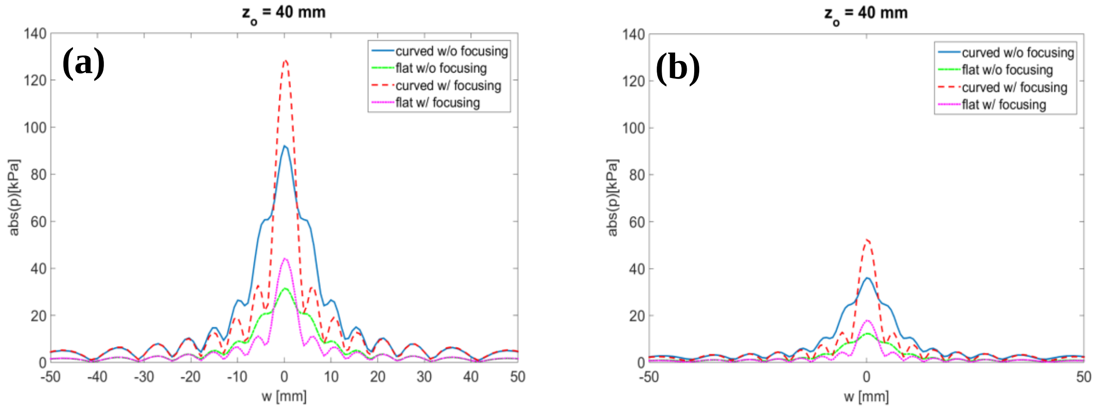

Fig. 4.2.2.5. Pressure for both curved and flat pMUT arrays operating in 1 MHz at Z=40 mm axial distance with and without electronic focusing at Z=30 mm: (a) without considering the mutual impedances; (b) including the mutual impedances.

In order to estimate the frequency response of the array, the frequency responses of all the elements (which are different from one another even if all are driven with the same input voltage) must be calculated. One way to estimate the far field frequency response shape of the array is to calculate the average volumetric displacement of all the transducers in the array. Figures 4.2.2.6a&b show the volumetric displacement frequency responses of pMUT (1,1), (1,N/2), (M//2,N/2), and the average of the curved pMUT array with 460 μm in pitch distance while considering the mutual impedances, as well as the average volumetric displacement when the mutual impedances are suppressed (which is equal to N_{tot} times the volumetric displacement of a single pMUT). It can be seen that each pMUT has a different frequency response depending on its location and that the average volumetric displacement has a different resonant frequency, 1.06 MHz in this case, than the resonant frequency of each pMUT at 0.97 MHz. Furthermore, the maximum average volumetric displacement magnitude drops by a factor of 2 while the 6dB bandwidth has increased almost 100%, from 150 kHz to 300 kHz. Such changes are directly associated with the mutual interactions and can be tuned by changing the array configuration. For instance, if the pitch is set to be 320 μm (Figures 4.2.2.7a&b), the magnitude maximum drops by a factor of 4.2 comparing to the case with no mutual impedances, while the 6dB bandwidth has a 370% increase to 660 kHz.

There have been several works on bandwidth improvement [77] and gain-bandwidth optimization [78] of cMUT based on similar schemes.

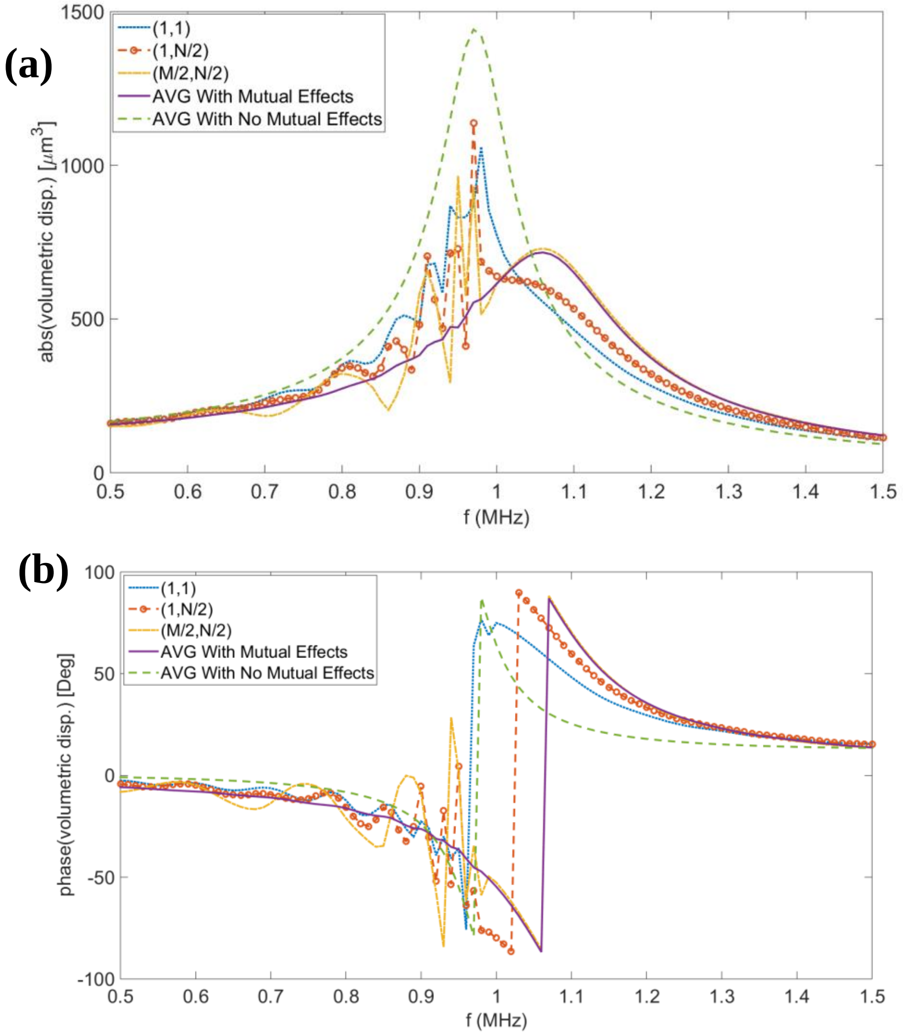

Fig. 4.2.2.6. Volumetric displacement frequency responses ((a) magnitude, (b) phase) of pMUT (1,1), (1,N/2), (M//2,N/2), and the average volumetric displacement of the curved pMUT array with 460 µm, pitch distance

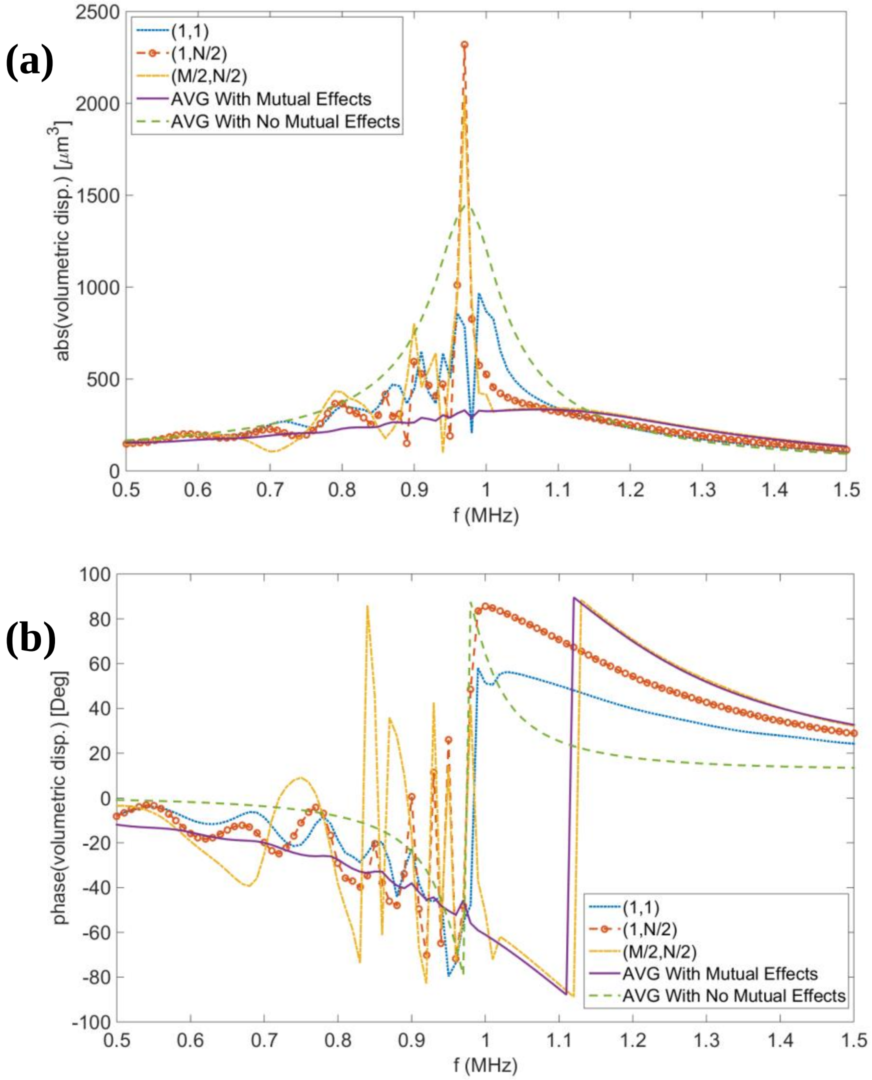

Fig. 4.2.2.7. Volumetric displacement frequency responses ((a) magnitude, (b) phase) of pMUT (1,1), (1,N/2), (M//2,N/2), and the average volumetric displacement of the curved pMUT array with 320 μm, pitch distance

By taking a closer look at the average volumetric displacement frequency responses of the model array structures in Fig. 4.2.2.6&7, spurious variations can be observed at frequencies lower than the resonant frequency. It was analytically shown in [60] that such low-frequency resonances can be due to the Rayleigh-Bloch (R-B) surface waves. Such surface waves can be generated in an array of periodically placed resonators [79]. It was mentioned in [80], [81] that such waves can exist at the cMUT-fluid interface in infinitely large cMUT arrays. For a finite size array, the reflections of R-B waves from the edges of the array can create Fabry-Pérot standing waves [60]. It was shown that at such frequencies the normalized velocity fluctuation of the array peaks and it can be an identifier of this type of standing wave. Following a similar definition used in [60], the normalized volumetric displacement fluctuation frequency response of the curved pMUT array is calculated and shown in Fig. 4.2.2.8. Several resonant frequencies can be seen as the formation of a standing wave on the array. For example, Fig. 4.2.2.9 shows the volumetric displacement amplitude of the array transducers at 0.86 kHz, which is approximately predicted as a standing wave resonant frequency in Fig. 4.2.2.8. It is observed that the vibration amplitude of the transducers away from the edges and along a row or a column varies periodically from a maximum value to a minimum value, which is about 1/5 of the maximum and is close to a standing wave condition. Similar forms were observed for the other resonant frequencies seen in Fig. 4.2.2.8.

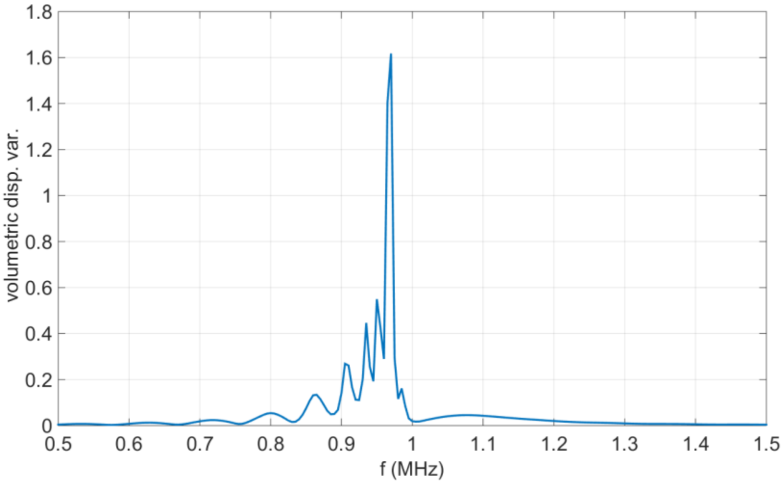

Fig. 4.2.2.8 Normalized volumetric displacement fluctuation of the model curved pMUT array.

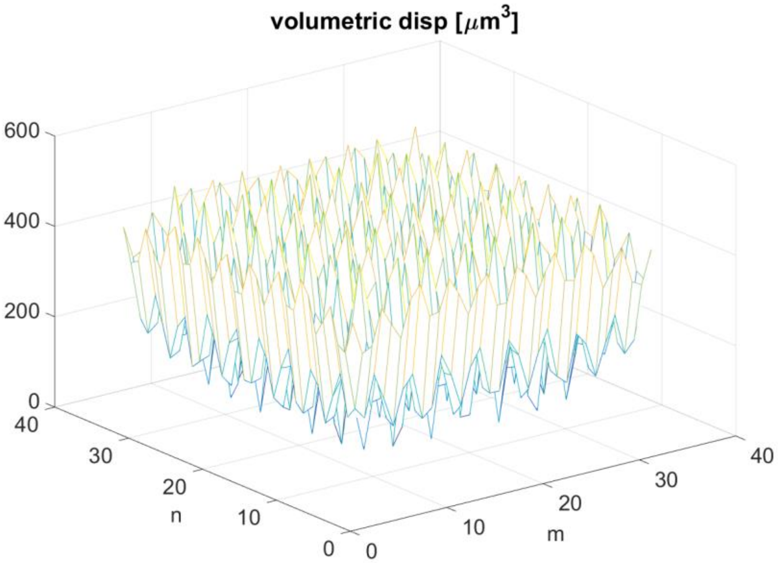

Fig. 4.2.2.9 Volumetric displacement of the model curved pMUT array at 0.86 MHz which is one of the resonant frequency of Fig. 4.2.2.8.

4.3. Conclusion

Using the calculated electromechanical equivalent circuit model for single pMUT and the self and mutual acoustic radiation impedances developed in previous works, an analytical model has been developed for curved and flat pMUT arrays by applying similar approaches used for thickness-mode piezoelectric [4] and cMUT arrays [57]. Such circuit models connect the electrical, mechanical, and acoustical domains to one another in order to calculate the output pressure field with respect to the applied voltage matrix and vice versa. Furthermore, the array model is capable of incorporating beam steering and focusing and predicting the acoustic beam shape and sound pressure level, as well as calculating the volumetric displacement and induced current in individual pMUTs. The developed methods for building the electromechanical circuit models for curved and flat pMUTs can be further generalized to derive circuit models for other pMUT architectures and their array forms.

Table 4.3.1. The material properties used in the analysis and simulations

Parameter	**Description**	**Value**	**Unit**
ρ_{AlN}	AlN density	3300	Kg/m^3
$Y_{0\text{-}AlN}$	AlN Young’s modulus	348	GPa
v_{AlN}	AlN Poisson’s ratio	0.30	
$d_{31\text{-}AlN}$	AlN Piezoelectric charge constant	2.20	m/V
ε_{AlN}	AlN Dielectric constant	10.26	
ρ_{Si}	Poly-Si density	2329	Kg/m^3
$Y_{0\text{-}Si}$	Poly-Si Young’s modulus	170	GPa
v_{Si}	Poly-Si Poisson’s ratio	0.28	

Table 4.3.2. List of curved and flat pMUT parameters used for array simulations.

Parameter	**Description**	**Curved pMUT**	**Flat pMUT**

a	radius	60 µm	60 µm
h_{AlN}	AlN thickness	1µm	0.5 µm
h_{Si}	Si thickness	-	2.3 µm
R_c	Radius of curvature	650 µm	-
a_1'' / a	Top electrode coverage ratio	100%	70%
f_{r_air}	Resonant frequency in air	3.8 MHz	3.7 MHz
f_{r_water}	Resonant frequency in water	0.97 MHz	0.97 MHz

Table 4.3.3. List of important circuit parameters and expressions for curved and flat pMUT.

Parameter	**Description**	**Expressions for Curved pMUT**	**Expressions for Flat pMUT***
Y_m	Mechanical admittance	$2\pi R_c^2 X(\omega)$	$(2j\omega a^4 / \pi D)\sum_{k=1}^{\infty} \Phi_k^2 / (\Lambda_k \Gamma_k)$
$b_{t(,j)}{}^{**}$	Transduction coefficient	$\left[4\pi Y_0 d_{31} R_c / (1-v)\right] X(\omega)$	$(2j\omega\pi a Y'_{0,p} d'_{31,p} Z_p / D)\left[O_k(a''_j) - O_k(a'_j)\right]\sum_{k=1}^{\infty} \Phi_k / (\Lambda_k \Gamma_k)$
$C_{0(,j)}$	Blocked capacitance	$2\pi\left(1-\cos\phi_0\right) R_c^2 \varepsilon_r \times (1-k_e{}^2)/h$	$\varepsilon'_z A_j / h$
$\eta_{(j)}$	Electrical to mechanical transformer ratio	$2Y_0 d_{31} / \left[R_c(1-v)\right]$	$(\pi^2 Y'_{0,p} d'_{31,p} Z_p / a^3)\left\{\left[\sum_{k=1}^{\infty}(O_k(a''_j) - O_k(a'_j)) \times \Phi_k / (\Lambda_k \Gamma_k)\right] / \left[\sum_{k=1}^{\infty} \Phi_k^2 / (\Lambda_k \Gamma_k)\right]\right\}$

$w / w_{\max}$	Normalized normal displacement (1st mode)	$\left(-0.30\left(\frac{r'}{a}\right)^6+0.34\left(\frac{r'}{a}\right)^5+1.13\left(\frac{r'}{a}\right)^4 -0.10\left(\frac{r'}{a}\right)^3-2.04\left(\frac{r'}{a}\right)^2-0.02\left(\frac{r'}{a}\right)+1\right)$	$\left(1-\left(\frac{r'}{a}\right)^2\right)^2$
Z_{ii}	Self-radiation acoustic impedance	$k_{c1}(\rho C/(\pi r_{eff}{}^2))[1-(2/\gamma)J_1(\gamma) +(4/\pi)\int_0^{\pi/2}\sin(\gamma\cos(x))\sin^2(x)dx$	$(\rho C/(\pi r_{eff}{}^2))[1-(2/\gamma)J_1(\gamma) +(4/\pi)\int_0^{\pi/2}\sin(\gamma\cos(x))\sin^2(x)dx$
Z_{ij}	Mutual-radiation acoustic impedance	$k_{c2}\frac{9\rho C}{5\pi a^2}A(ka)\frac{\sin(kd)+j\cos(kd)}{kd}$	$\frac{9\rho C}{5\pi a^2}A(ka)\frac{\sin(kd)+j\cos(kd)}{kd}$

***** The variables and the expression derivations for the flat pMUT equivalent circuit can be found in [36].

** (*j*) subscript indicates the electrode number in a multiple electrode flat pMUT. In this paper we used a conventional single-electrode flat pMUT.

Chapter 5

DEB PMUT for Muscle Spasm Diagnosis

5.1. Introduction

Muscle injuries related to ergonomics and repetitive motion have become a major medical problem in today's working environment. A method of monitoring muscular behavior capable of predicting and/or mitigating this problem could be valuable. The ultrasound technology has been used as a nondestructive method in various applications such as, range finding, nondestructive testing, medical imaging and treatments [1]-[7]. In the medical imaging and diagnosis field, various methods has been implemented for different applications such as, B-mode pulse-echo imaging, Doppler ultrasound for blood flow measurements, high-intensity focused ultrasound (HIFU) for laparoscopic surgery, and shock wave lithotripsy for kidney stone treatment [1], [3], [5], [6]. Sonoelastography is another way of medical imaging in which color-coded elasticity maps of the medium is formed [83]-[88]. A common way of forming such an image is to excite shear waves inside the tissue by mechanical means to form shear strains and a displacement map would be captured using Doppler ultrasound. The elasticity map can then be generated using the collected displacement data [83]-[87]. Currently, sonoelastography has been mainly implemented in prostate tumor detection, liver disease, and Musculoskeletal diagnosis for tendons and fascia evaluations [85]-[86].

In this chapter, we demonstrate the feasibility of muscle spasm detection using an array of DEB pMUT [17]-[18] by both pulse-echo and continuous wave modes. In practice, the DEB pMUT array can be directly integrated with a portable handheld device or used as a dermal patch as the monitoring device for real-time or off-line evaluations. In addition to on-line self-monitoring by the patient, the collected data can also be stored and later studied by the specialist for chronic pain examination purposes.

5.2. Concept and Experimental Setup

In order to investigate the possibility of capturing the mechanical changes of muscle between the relaxed and cramped states, two PDMS samples with different mechanical properties were fabricated. It is shown that slight difference of speed of sound between the two samples can be detected using a 1D DEB pMUT array operating in the pulse-echo mode. Figure 5.2.1 shows a schematic diagram of the pules-echo measurements using the right side pMUT for transmission by driving it with a sinusoidal pulse and receiving the reflected echo with the left side pMUT. The generated pulse passes through the mineral oil that simulates fat, skin, and the matching gel and reaches the muscle mimicking material, PDMS. The transmitted pulse would be reflected off of the mismatched boundary, such as air or bone, and travel back to the receiver pMUT.

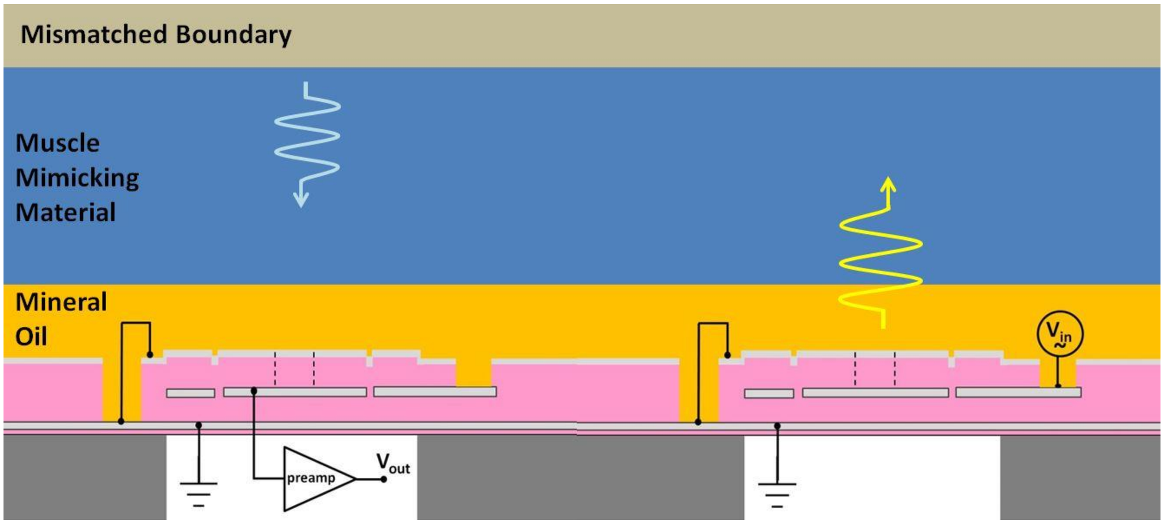

Fig. 5.2.1. Schematic drawing of the pule-echo measurement scheme using DEB pMUT.

5.2.1. Muscle Mimicking Sample Preparation

Polydimethylsiloxane (PDMS) and other types of silicone materials have been previously used as tissue mimicking materials [89]-[91]. Here, two PDMS samples with base to curing agent ratios of 10:1 and 50:1 were fabricated using the Sylgard 184 Silicone Elastomer Kit. A custom 3D printed mold was used to make PDMS samples as shown in Fig. 5.2.1.1. The PDMS samples were fabricated by transferring the PDMS solution to the mold, degassing under vacuum for 1 hour and curing in oven at 65^{o}C for 4 hrs. Although the speed of sound and elasticity of the fabricated PDMS samples are not exactly the same as those for human muscles - sound speed of about 1575-1595 m/s in the relaxed state [92] and Young's modulus varying from a few to tens of kilopascals [93]-[95] - the measured speed of sound of the PDMS samples were in the same order of magnitude [96] and similar elasticity variations for human muscles in different states [93].

Fig. 5.2.1.1 3D printed mold to make the PDMS samples.

5.2.2. PMUT Array Sensitivity Measurements

A 5-channel 1D DEB pMUT array with 6×27 DEB pMUTs per channel and 2.76 mm channel pitch was fabricated and only 3 consequent channels were used in the prototype experiments with the middle channel as the receiving transducer and the two outer channels as the transmission transducers. The pMUTs are 120 μm in diameter with 460 μm pMUT pitch per channel. Figure 5.2.2.1 shows a 3D schematic of the 1D DEB pMUT array illustrating the Rx and one of the Tx channels. The figure also shows a cross-sectional view of a DEB pMUT consisting of two active aluminum nitride (AlN) piezoelectric layers; top, bottom, middle inner, and middle outer Molybdenum (Mo) electrodes with full areal coverage of the top and bottom electrodes and 50% areal coverage of each of the middle electrodes. Thin PECVD SiO_2 layers were also deposited under the middle and top electrodes to prevent the diffusion and shorting of the following Mo electrodes through AlN [97]. Figure 5.2.2.1 also shows the stack thicknesses of the DEB pMUTs while the comprehensive illustration of design and fabrication of DEB pMUT can be found in [17]-[18].

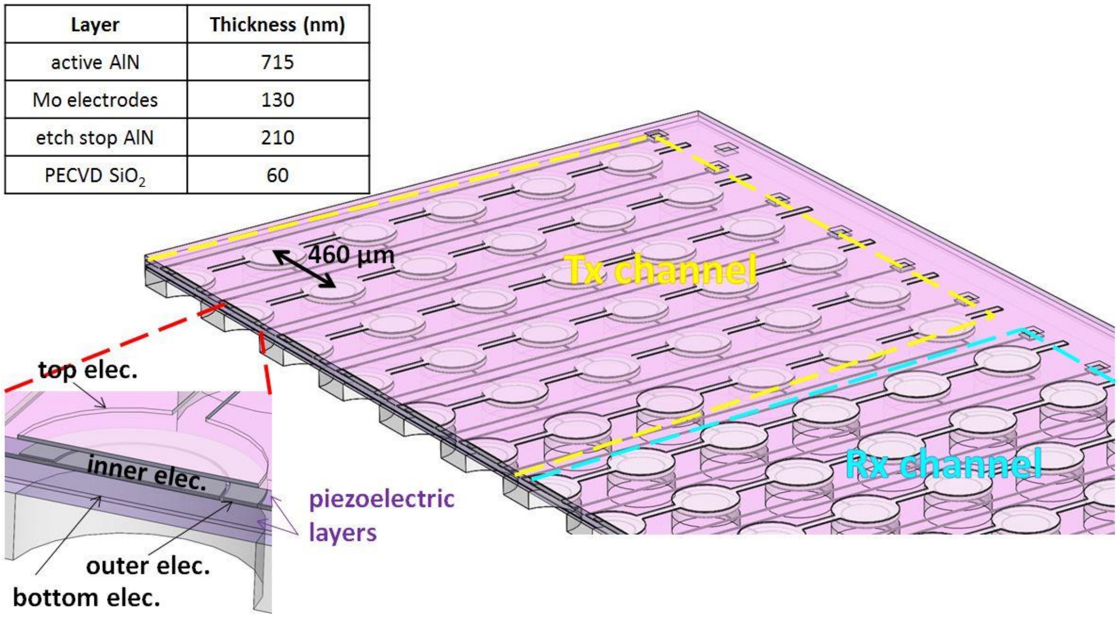

Layer	Thickness (nm)
active AlN	715
Mo electrodes	130
etch stop AlN	210
PECVD SiO_2	60

Fig. 5.2.2.1. 3D view of the DEB pMUT array showing part of the Rx and one full set of the Tx channels. The enlarged view is a DEB pMUT with a table of the stack thicknesses.

Figure 5.2.2.2 shows an optical image of two side-by-side 5-channel 1D DEB pMUT arrays and only the first three channels on the left side as marked were used for testing. The arrays were bonded to the custom PCB using a thermal release tape and their edges were sealed using silicone adhesive to prevent penetration of liquid to the backside of the pMUTs. The arrays were finally wire-bonded to the PCB for testing purposes.

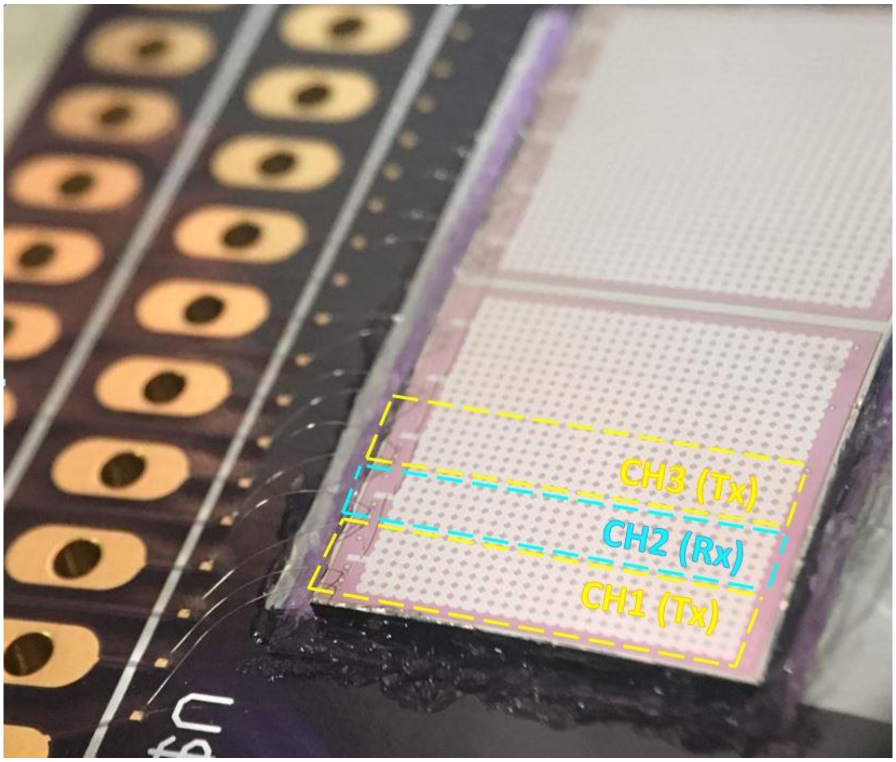

Fig. 5.2.2.2. Optical image of the DEB pMUT arrays showing both the Tx and Rx channels for testing.

In order to measure the driving and receiving sensitivity of the pMUT channels, a commercial ultrasonic transducer (UZ250, Noliac) was used to transmit signals to and receive from the pMUT array. For the evaluation of the receiving sensitivity, the ultrasonic transducer was placed at an axial distance of 20 mm from the pMUT array in a mineral oil tank and was driven with 4.7 V_{pp} to generate 6.43 kPa at the pMUT surface. The induced voltage on channel 2 (middle channel of the 3-channel 1D DEB pMUT array) was 10 mV which results in the receive sensitivity of 1.56 $\mu V_{pp\text{-}out}$/Pa without any amplification. On the other hand, the drive sensitivity of the pMUT was measured by driving channel 1 (one of the side channels of the 3-channel 1D DEB pMUT array) at 1.1 V_{pp} and measuring the responses of the commercial ultrasonic transducer at an axial distance of 20 mm away from the pMUT arrays in the oil tank. The measurement results on the receiver was 300 mV which corresponded to 218 Pa ultrasound pressure, or a drive sensitivity of 3.96 kPa.mm/$V_{pp\text{-}in}$ which shows the generated pressure amplitude per input peak-to-peak voltage at unit axial distance. Finally, the round trip sensitivity of the channels from an object with 100% acoustic reflection was calculated to be 78.3 $mV_{pp\text{-}out}/V_{pp\text{-}in}.mm|_{round\ trip}$ by driving channel 1 and receiving the signals from channel 2 with 25.5X amplification on the receiver using a commercial hydrophone preamplifier (AH-2010 Preamplifier, Onda Corp.). This means that given the input voltage on channel 1 and the axial distance between the object of interest and the pMUT array, the maximum possible signal induced on channel 2 can be estimated.

5.2.3. Sample Mounting Setup

In order to capture the ultrasound responses from the PDMS samples, a 3D printed mounting setup was designed (Figure 5.2.3.1a) and fabricated (Fig. 5.2.3.1b). Figure 5.2.3.1b shows the 3D printed mounting setup with a custom PCB and a PDMS sample positioned in the designated areas. The mounting setup contains a gap for the pMUT PCB with two cantilever locking springs to prevent it from sliding out. The muscle mimicking sample can be placed through the pressed-fitted metal rods on top of the PCB. An 8-mm gap was designed between the PCB and the muscle mimicking sample that will be filled with oil during the experiment. This oil-filled gap was also intended to simulate fat, skin, and the matching gel/material that would come into play in practical muscle diagnosis applications [98]-[99]. The top cap can be used to sandwich and fix the muscle mimicking sample vertically and also can be designed to mimic other body structures such as bones.

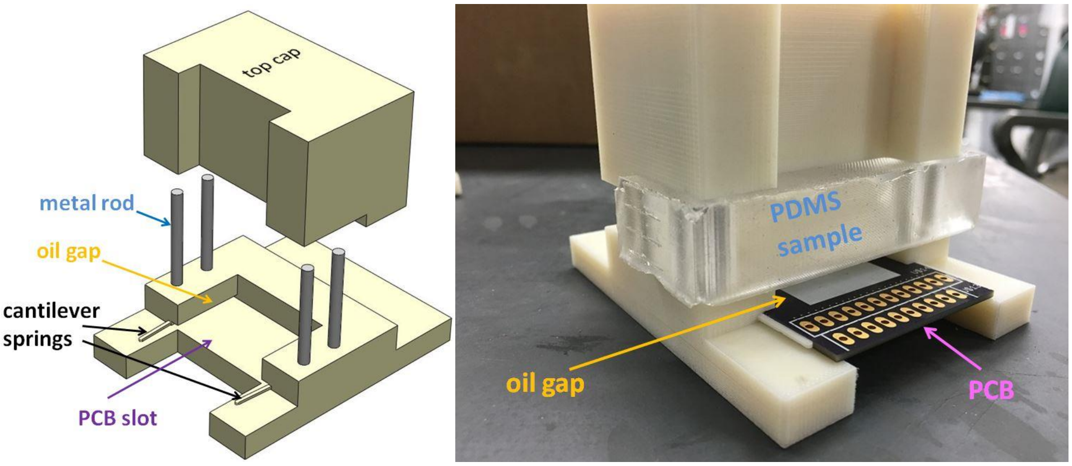

Fig. 5.2.3.1. (a, left) 3D schematic of the mounting setup; (b, right) The 3D printed mounting setup with the custom PCB (5×5 cm^2 in size) and the PDMS sample positioned in the designated locations.

Figure 5.2.3.2 shows the experimental setup where the pMUT PCB was inserted into the mounting setup which was placed in a plastic container to be filled with mineral oil without the PDMS sample (Figure 5.2.3.2a) and with the PDMS sample (Figure 5.2.3.2b). The bonding pads were wire bonded to the PCB which is connected to the Tx and Rx setup outside of the tank. The tank will be filled with mineral oil during the experiment up to the point that the gap between the PDMS sample and pMUT array is completely filled.

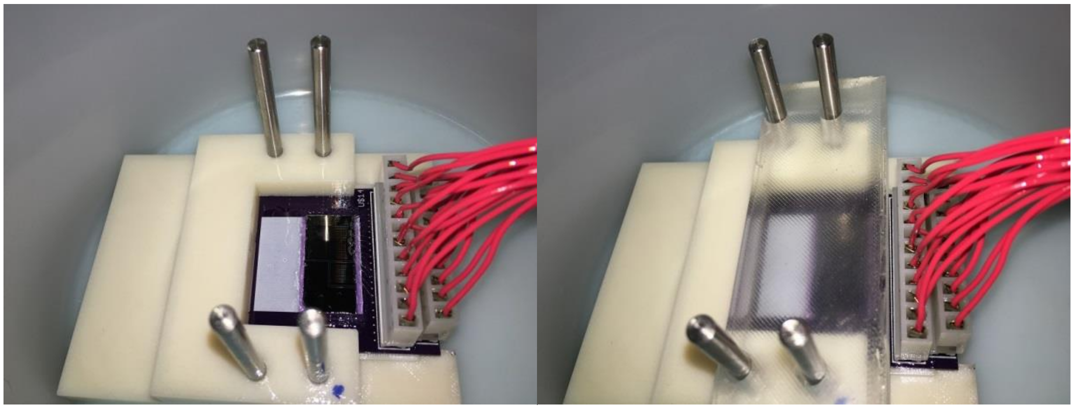

Fig. 5.2.3.2. Mounting setup with pMUT PCB where the setup is placed in a plastic container to be filled with mineral oil (a, left) without and (b, right) with a PDMS sample placed on top of the pMUT arrays.

5.3. Experimental Results for Pulse-echo Tests

It has been shown that the mechanical properties of human muscles, such as elasticity, can alter under different muscle states [93]-[94]. In this experiment, pulse-echo method was implemented to measure and detect the change of speed of sound as an indicative characteristic of the mechanical property differences between the two PDMS samples.

Figure 5.3.1 shows the pulse-echo responses of the pMUT array for the PDMS samples: (a) the 10:1 sample of 17.3 mm in thickness; and (b) the 50:1 sample of 21.7 mm in thickness. During the tests, channel 1 inner electrodes and channel 3 outer electrodes were driven with 7-cycle, 300 kHz sinusoidal bursts with 9.7 V_{pp} while the rest of the electrodes of the two channels were grounded. Channel 2 was used as the receiver with its inner electrodes connected to the preamp and the rest of its electrodes grounded. The launched acoustic pulses entered the PDMS sample with minimal reflection at the oil-PDMS interface but were reflected back at the air-PDMS interface since air had a significantly different acoustic impedance than that of PDMS. In the real application for muscle spasm diagnosis, bone also has very different acoustic impedance than that of muscle to reflect the acoustic pulses. It is noted that in the aforementioned two cases, the reflected pulse signals off of bone and air would have opposite phases with almost the same amplitudes and here the only important parameter under investigation is the time of flight of the first echo which would be equal in both cases. Figure 5.3.1a shows that the first echo for the 10:1 sample is received at t = 48 μs while Fig. 5.3.1b shows that the first echo for the 50:1 sample is received at t = 54.8 μs. The second echoes that are generated by the reflection of the first echoes from the pMUT surface can also be observed at about twice the first echo arrival time in both Figs. 5.3.1a&b but with further reduced amplitudes. The electrical cross-talk can also be observed at the receiver during the driving period and it is not of importance as long as settling time is fast such that the cross-talk signals would not merge with the reflected echo signals. However, for continuous wave (CW) measurements such signal will be mixed with the echo signal and it needs to be filtered (subtracted) out from the main signal. This topic will be discussed in more details in section 5.4 and 5.5.

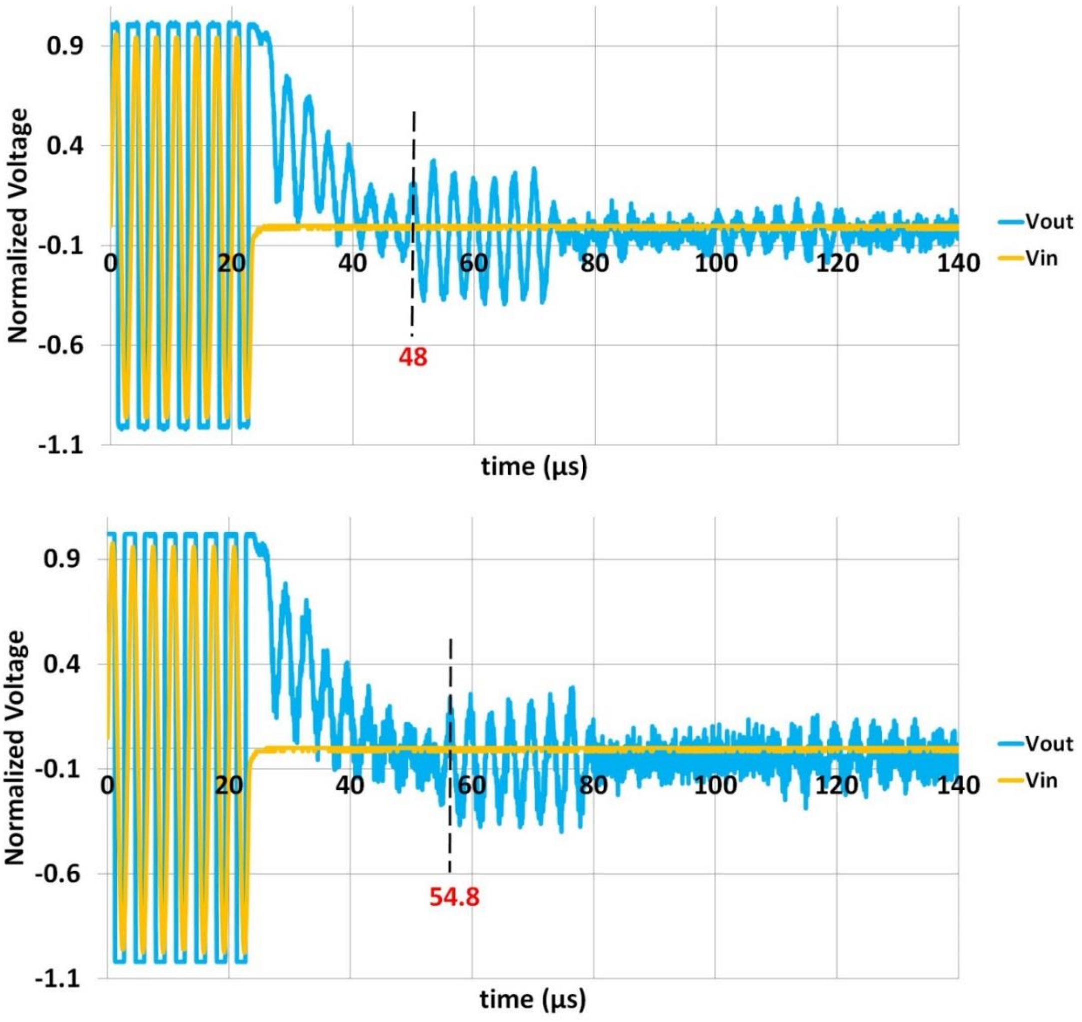

Fig. 5.3.1. Pulse-echo responses of the pMUT array with (a, top) the 10:1 sample; and (b, bottom) the 50:1 sample.

Since the speed of sound in the mineral oil is 1440 m/s, and the mineral oil height is 8mm in the prototype setup, the speed of sound in the PDMS can be calculated as:

$$C_{PDMS} = \frac{2h_{PDMS}}{(TOF - 2h_{oil} / C_{oil})} \tag{5.3.1}$$

where C_{PDMS} and C_{oil} are the speeds of sound in PDMS and oil respectively, h_{PDMS} and h_{oil} are the thicknesses of the PDMS and oil gap respectively, and *TOF* is the round trip time of flight of the first pulse-echo.

Experimental results show that the speeds of sound of the 10:1 sample and 50:1 sample are 938 and 993 m/s, respectively. It must be noted that although 50:1 PDMS has lower Young's modulus, it has slightly higher Poisson's ratio and Eq. 5.3.2 shows that the speed of sound in a material can be approximated by the Young's modulus (*Y*); the density (ρ); and Poisson's ratio (*v*), for $0 < v < 0.5$ of the material as [100]:

$$C_{solid} = \sqrt{\frac{Y(1-\nu)}{\rho(1+\nu)(1-2\nu)}} \tag{5.3.2}$$

The 5.9% change of speed of sound between the two PDMS samples represents muscles in different states and can be detected using this technique. Such changes could be caused by the variations of muscle mechanical properties in different states [93]-[94].

Figure 5.3.2 shows the received peak-to-peak voltage after the preamp versus the input peak-to-peak voltage. The plots reveal that the received voltage of the reflected echoes is a linear function of the input voltage. Furthermore, the received voltages for the 50:1 sample is lower than those for the 10:1 sample due to the longer round trip distance of the pulse and echo for the 50:1 PDMS with higher thickness resulting in more losses during the travel of the signal. After eliminating the spreading loss effects which are proportional to the round trip length in the far field region, the received voltages per input voltages for the two cases were almost equal with 1.8% average of the errors and 5% standard deviation of the errors. This shows that the main cause of pressure amplitude attenuation is due to spreading loss rather than the material loss.

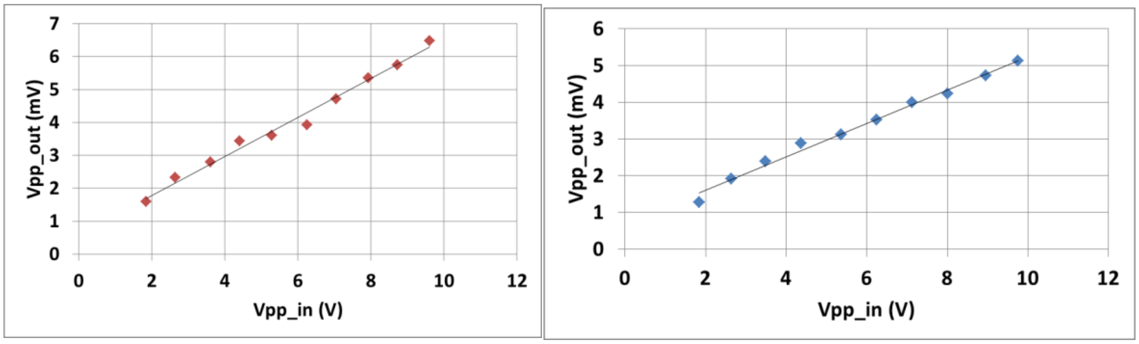

Fig. 5.3.2. Received peak-to-peak voltage after the preamp versus the input peak-to-peak voltage from the driver at 300 kHz for (a, left) 10:1 PDMS and (b, right) 50:1 PDMS.

In real muscular applications, the muscle in the cramped state might have changes in both stiffness and thickness and it may be difficult to decouple the individual contributions from the acoustic response. However, as long as the change is significant, whether it is caused by the speed of sound or thickness, the two states can be detected with this simple method using such low-cost, low-power, MEMS ultrasonic arrays for various applications.

5.4. Continuous Wave Response

Another approach is to apply the continuous wave mode to create standing waves between the pMUT array and the mismatched boundary to detect the steady state pressure amplitude at the receiver. The advantage of using the continuous wave mode is that the received signal can potentially be intensified by adding up echoes constructively from multiple reflections of echoes to increase the SNR. Furthermore, by choosing the right operation frequency (thus the right wavelength), it might be possible to achieve significantly different pressure levels at the receiver between the two states of muscle where in one state the echoes could all add up constructively at the receiver to generate a high pressure while in the other state this would not be the case to receive a lower pressure level. On the other hand, this technique is very sensitive to the thickness and property variations such that a sophisticated calibration procedure will be required. Furthermore, the cross-talk noise issue must be attenuated to achieve high SNR.

FEA simulations using COMSOL Multiphysics were implemented to investigate the effects of change of sound speed in muscles based on the continuous wave responses. 2D axisymmetric acoustic simulations were performed where a circular transducer with radius of 4.5 mm was used as the receiver while an annular piston transducer with a width of 3 mm was used as the transmitter around the receiver to transmit continuous waves at 118 kHz with displacement amplitude of 3.3 nm. The previously measured transducer responses are used in the model so the response of the annular transducer would be close to fabricated DEB pMUT array.

Figure 5.4.1 shows the real part of the acoustic pressure profiles for two cases with the assumption that the speed of sound in muscle is (a) 1590 m/s and (b) 1880 m/s, respectively. Table 5.4.1 shows the geometric and acoustic properties of the materials used in COMSOL simulations where the acoustic attenuation coefficients, *a* and *b*, are the parameters used in the attenuation equation [5]:

$$A(z) = A_0 \exp(-af^{b} z / 8.7) \tag{5.4.1}$$

where $A(z)$ is the acoustic wave amplitude; A_0 is the amplitude at $z=0$, z is the axial distance between A and A_0, f is the frequency of operation, and a and b are the attenuation coefficients.

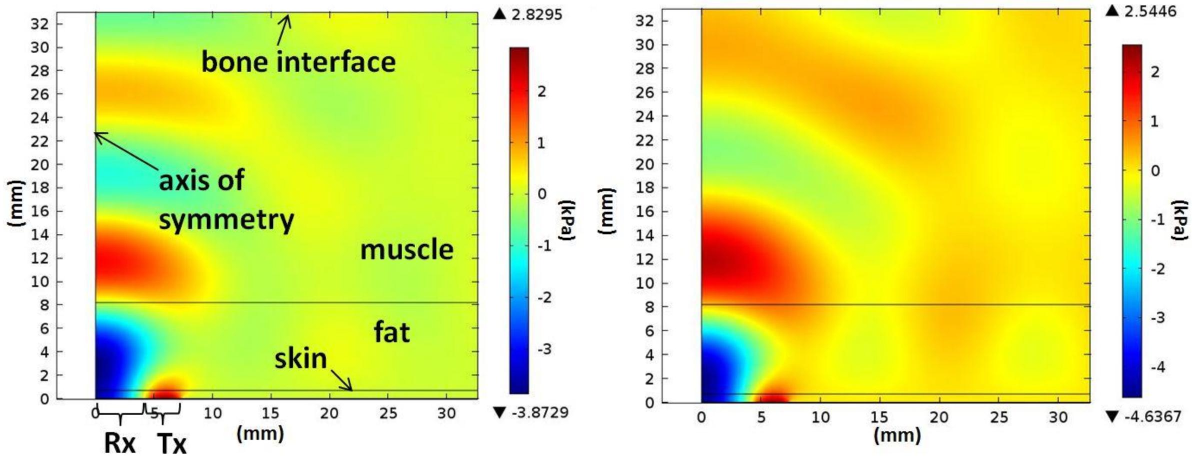

Fig. 5.4.1. Real part of the acoustic pressure for muscle-like material with the speed of sound of (a, left) 1590 m/s and (b, right) 1880 m/s with Tx transducer in continuous mode at 118 kHz with 3.3 nm displacement.

Table 5.4.1. COMSOL material parameters

Parameter	Value
Skin thickness	0.7 [mm]
Fat thickness	7.5 [mm]
Muscle thickness	25 [mm]
Skin speed of sound	1730 [m/s]
Fat speed of sound	1450 [m/s]
Muscle speed of sound	1590-1880 [m/s]
Skin density	1150 [kg/m^3]
Fat density	950 [kg/m^3]
Muscle density	1065 [kg/m^3]
Skin attenuation coefficients	a=0.54, b=1
Fat attenuation coefficients	a=0.48, b=1
Muscle attenuation coefficients	a=3.3, b=1

The frequency of operation must be selected in a way such that the difference between the two states is distinguishable. For example, if the medium were homogenous with the total distance of L between the ultrasonic transducer and the mismatched boundary (i.e. round trip = $2L$) with sound speed of C. By setting $\lambda=2L/n$ or $f=nC/2L$ (where n is an integer number), constructive interference of the transmitted wave and the reflections at the receiver will be assured. By setting $\lambda=4L/(2n+1)$ or $f=(2n+1)C/4L$, the destructive interference of odds and even reflections at the receiver will be accomplished. However, the medium is generally not homogenous such that it is difficult to derive an analytical formula for the optimum operation frequency that can distinguish the two states. Using the FEA simulations, it was found that at f=118 kHz the two states can be well distinguished for the prototype example. Figure 5.4.2 show the real and imaginary part of the radial pressure at the receiver of Fig. 5.4.1 at the operation frequency of 118 kHz. By integrating the receiver area, it was found that the absolute average pressure on the receiver using the example of the 1590 m/s muscle sound speed was 3.54 kPa while the value for the 1880 m/s muscle sound speed was 4.56 kPa. It can be seen that 18% difference in speed of sound results in 29% change in the amplitude of the receiver pressure in the CW mode. Consequently, it can be observed that the CW mode in an ideal case might have better sensitivity over the pulse-echo mode, although it is more complicated to implement this method in the real application.

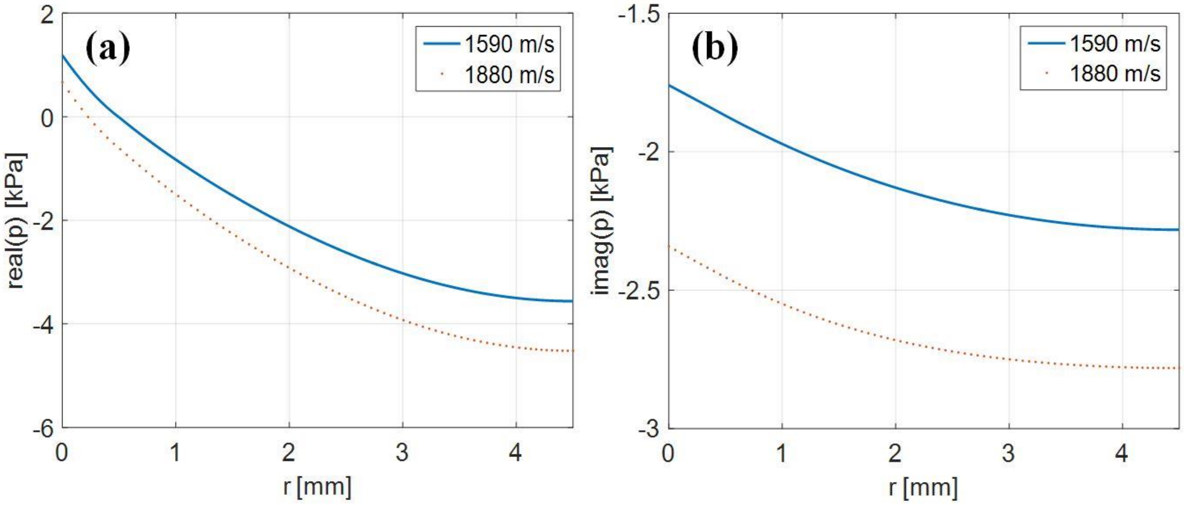

Fig. 5.4.2. (a) real and (b) imaginary part of the radial pressure at the receiver of Fig. 5.4.1.

5.5. Electrical Cross-talk

It can be seen from Fig. 5.3.1 that the electrical cross-talk occurs at the receiver during the transmission period. The main reason behind such phenomenon is that the transmitter and the receiver devices are internally connected at some nodes including the common grounds. For instance, Fig. 5.5.1 shows the simplified circuit models of the transmitter (Tx) and the receiver (Rx) of pMUTs at the operation frequency where they share a common node connected to the ground. However, due to the parasitic impedances of the connections from the common node to the real ground, Z_{pg}, the common node between the transmitter and the receiver has a different potential than that of the actual ground.

In Fig. 5.5.1, v_s is the transmitter source voltage, v_i is the input voltage on the transmitter, v_o is the receiver voltage after the preamp, R_i is the input series resistance to the transmitter, T_X and R_X are the transmitter and receiver equivalent impedance models respectively, v_c is the voltage of the common node between the T_X and R_X, and v_m is the induced voltage on the receiver pMUT due to mechanical motion of the transducer caused by the incoming acoustic wave.

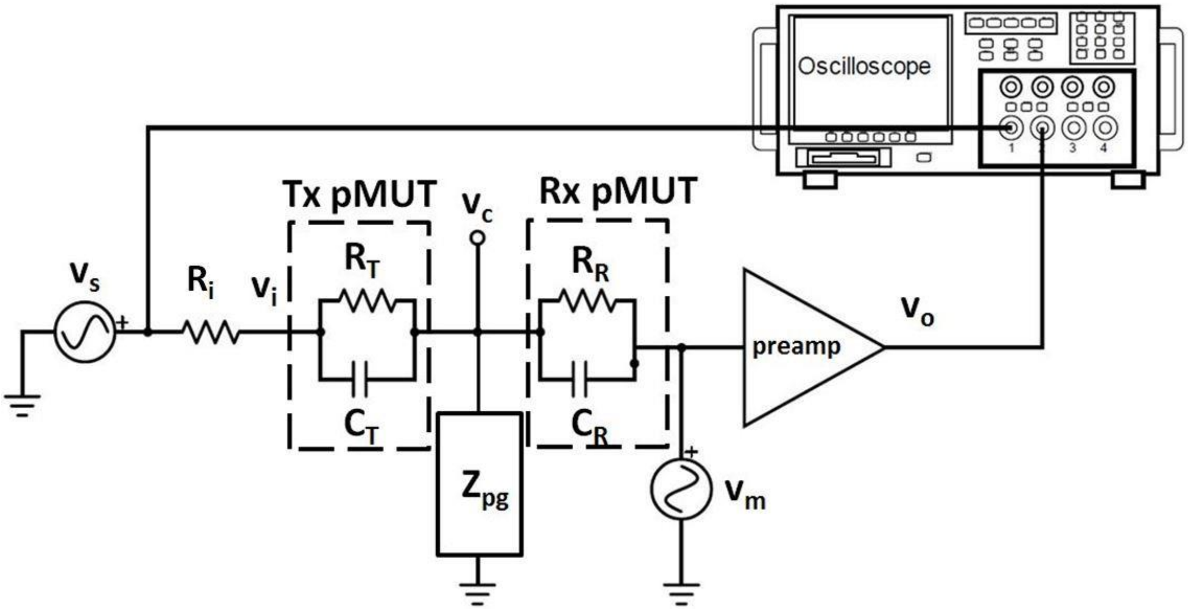

Fig. 5.5.1. Circuit schematic of Tx/Rx with parasitic impedance modeled at the ground node causing the electrical cross-talk between the transmitter and receiver.

In order to eliminate the cross-talk signals, one can take multiple approaches such as: (1) if operating under fixed conditions such as input voltage amplitude and frequency which result in a certain cross-talk waveform, the generated waveform can be stored and subtracted from the received signal in software level at the signal processing stage; (2) if there exist a dummy channel with the same structure as the receiver but with non-released pMUT diaphragms so that it cannot capture any acoustic responses from the reflected echo, the induced cross-talk on that channel can be directly subtracted from the Rx channel to achieve the induced signal only due to the acoustic reflection at the receiver; (3) if Z_{pg} can be modeled well based on the calculation of the v_c/v_i transfer function, then the cross-talk voltage can be directly generated from v_s and can be subtracted from the received signal at circuit level by building an equivalent Z_{pg} and feeding it with the input voltage. Here, the third approach is investigated to validate the proposed theory behind the cross-talk and the feasibility of the method because approach#(1) is doable at software level for a certain frequency but is not in the scope of this study; and approach#(2) requires an extra dummy Rx channel which was not available for the fabricated arrays.

In this approach, Z_{pg} is modeled as a parallel RLC load with the following impedance:

$$Z_{pg\_\mathrm{model}} = \frac{R_{pg} L_{pg} j\omega}{R_{pg} - R_{pg} L_{pg} C_{pg} \omega^2 + L_{pg} j\omega} \tag{5.5.1}$$

where R_{pg}, L_{pg}, and C_{pg} are the equivalent parallel resistor, inductor, and the capacitor forming Z_{pg_model} and ω is the angular frequency. On the other hand, Z_{pg} can be calculated by measuring the $H(\omega)=v_o/v_i$ transfer function. Since the receiver impedance looking from the common node is very large, Z_{pg} can be calculated as:

$$Z_{pg\_meas} = \frac{H(\omega)/G_p\left((R_T C_T j\omega+1)R_i + R_T\right)}{\left(1-H(\omega)/G_p\right)\left(R_T C_T j\omega+1\right)} \tag{5.5.2}$$

where G_p is the preamp gain, and $v_c|_{vm=0} \approx v_o/G_p$. Now, the least square method can be implemented to derive the optimum values of R_{pg}, L_{pg}, and C_{pg} for the model impedance as shown in Eq. (5.5.3) using Eqs. (5.5.1) and (5.5.2) and sweeping the frequency of operation.

$$\left(R_{pg}, L_{pg}, C_{pg}\right) = Arg\min \left\{RSS = \sum_i w_i \left(Z_{pg\_\mathrm{model}}(f_i) - Z_{pg\_\mathrm{meas}}(f_i)\right)^2\right\} \tag{5.5.3}$$

where RSS is the residual sum of squares, f_i is the i th frequency, and w_i is the weighing function which was chosen to be 3 units at the center frequency (300 kHz) and 1 at the end of the upper frequency (400 kHz) and lower frequency (200 kHz) with a linear trend toward the range limits. Figure 5.5.2 show the results predicted by the model and measurement showing the amplitude and phase of the $H(\omega)=v_o/v_i$ when v_m=0. The Z_{pg} parameters were derived from Eq. (5.5.3) with values: R_{pg}=0.78 Ω, L_{pg}=0.97 µH, and C_{pg}=0.47 µF where the transmitter circuit parameters were R_i=6 Ω, R_T=100 MΩ, and C_T=4.18 nF. The model and experimental results show good agreement while the differences are mainly due to the model simplifications and neglecting of the acoustic effects on the Rx such as the surface acoustic waves generated from Tx. Building more complex circuit models can result in better agreement between the model and the measurements. In addition, if the operation frequency is fixed, the model can be well-matched to the measurements at that frequency. It can also be seen that even though the cross-talk might have other causes, it still can be well-modeled using this method. Building such equivalent load and driving it with the same input voltage, v_i, results in the same output as the observed cross-talk part of the main signal at the receiver can be subtracted from the main signal to achieve v_o only due to v_m. By the elimination of cross-talk, continuous wave mode can be implemented in practice to potentially obtain better sensitivity.

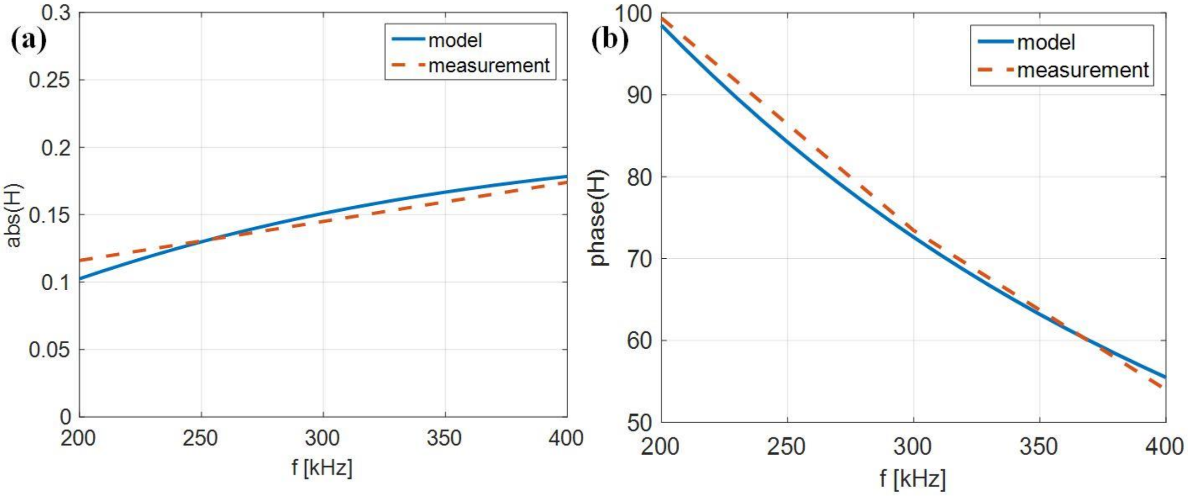

Fig. 5.5.2. (a) Amplitude and (b) phase of the v_o/v_i transfer function when v_m=0 for both the model and the measurement results.

5.6. Conclusion

In this chapter we demonstrated that pMUT arrays can be used to detect mechanical changes such as variation of speed of sound in materials with acoustical properties close to human muscles. A 1D DEB pMUT array was used to capture the pulse-echo responses from two different PDMS samples with slightly different speed of sounds situated in a custom 3D printed mounting setup with an oil gap between the pMUT array and the samples. In this testing, two outer channels were used for driving while the middle channel was used for receiving. By capturing the time of flight of the pulse and echo, a 5.9% speed of sound variation between the two samples was identified. In addition, the captured echo showed a linear amplitude trend with respect to the input voltage. Using FEA simulations, it was also shown that by performing continuous wave measurements in the absence of electrical cross-talk between the transmitter and the receiver under the right frequency, a 18% speed of sound difference between the two samples can produce a 29% average pressure difference on the receiver which makes the receiving more sensitive than the pulse-echo method. Finally, three methods were presented to eliminate the electrical cross-talk between the transmitter and the receiver to increase the SNR and one of the methods were investigated with well-matched analytical and measurement results. These results indicate that pMUT arrays can be used for real-time muscle spasm diagnosis in low-power portable handheld devices like cell phones or in form of external dermal patches with cable or wireless communication to a portable device.

Chapter 6

Conclusions and Future Work

6.1 Conclusions

We have demonstrated high-efficiency, CMOS-compatible, piezoelectric micromachined ultrasonic transducers with two novel designs, curved pMUT and dual-electrode bimorph pMUT, with significantly higher electromechanical efficiencies than those of the state-of-the-art pMUT architecture. We have derived the vibration theory of clamped spherical piezoelectric elastic shells followed by an equivalent circuit model of clamped, spherical-shape, curved pMUT with explicit expressions for the equivalent electromechanical circuit parameters and its acoustic radiation patterns. Prototype curved pMUT with two different fabrication techniques have been demonstrated with good consistency between the experimental, analytical, and FEA simulation results.

We have successfully fabricated single-transducers as well as various arrays of DEB pMUT for both air- and liquid-coupled applications utilizing new fabrication techniques for the development of the prototype devices with excellent crystal quality of AlN layers and good manufacturing yield. Experimental results match well with analytical and FEA simulation results to confirm that the energy efficiency and drive sensitivity of the DEB transducer can be 4X higher than those of the state-of-the-art single-electrode unimorph pMUT. Furthermore, a liquid-coupled array have shown the highest normalized acoustic intensity, $I_n = I/(VNd_{31})^2$, at a distance of 1.5 mm away from the array and the measurement results show that such array can be potentially used in low-voltage handheld medical ultrasonic devices.

An analytical model has been developed for curved and flat pMUT arrays by applying the calculated electromechanical equivalent circuit model for single pMUT with the inclusions of the self and mutual acoustic radiation impedances. Such circuit models connect the electrical, mechanical, and acoustical domains to one another in order to calculate the output pressure field with respect to the applied voltage matrix and vice versa. The array model is capable of incorporating beam steering and focusing and predicting the acoustic beam shape and sound pressure level, as well as calculating the volumetric displacement and induced current in individual pMUTs. The developed methods for building the electromechanical circuit models for curved and flat pMUTs can be further generalized to derive circuit models for other pMUT architectures and their array forms. Such analytical modeling is much faster than the commercial multi-physics FEA simulations tools, [52, 53] with better accuracy and information than the single-physics analytical acoustic programs [54, 55]. Such model provides a fast and solid guideline for pMUT array design, analysis, and optimization.

6.2 Future Work

The purpose of this works was to create high efficiency and sensitivity pMUT that can be integrated with consumer electronics such as battery-powered handheld devices for diagnosis applications, like muscle spasm diagnosis, or low-cost ultrasound devices with high acoustic intensity requirements for applications such as medical therapy. Feasibility of such applications has been shown in this thesis and the implementation of these pMUT devices in future products can be further investigated.

References

[1] A. J. Tajik, J. B. Seward, D. J. Hagler, D. D. Mair, J. T. Lie, “Two-dimensional real-time ultrasonic imaging of the heart and great vessels. Technique, image orientation, structure identification, and validation,” *Mayo Clin. Proc.*, vol. 53, pp. 271-303, 1978.

[2] S. Mitragotri, “Healing sound: the use of ultrasound in drug delivery and other therapeutic applications,” *Nature Reviews Discovery*, vol. 4, pp. 255-260, 2005.

[3] B. W. Drinkwater and P. D. Wilcox, "Ultrasonic arrays for non-destructive evaluation: A review," *Ndt & E International,* vol. 39, pp. 525-541, Oct 2006.

[4] C. H. Sherman and J. L. Butler, *Transducers and Arrays for Underwater Sound* (The Underwater Acoustic Series). New York, NY: Springer, 2007.

[5] G. S. Kino, *Acoustic Waves: Device, Imaging, and Analog Signal Processing*, Prentice Hall, 1987.

[6] D. L. Miller, N. B. Smith, M. R. Bailey, G. J. Czarnota, K. Hynynen, I. R. S. Makin, *et al.*, "Overview of Therapeutic Ultrasound Applications and Safety Considerations," *Journal of Ultrasound in Medicine,* vol. 31, pp. 623-634, Apr 2012.

[7] G. Ogris, T. Stiefmeier, H. Junker, P. Lukowicz, G. Tröster, “Using Ultrasonic Hand Tracking to Augment Motion Analysis Based Recognition of Manipulative Gestures,” Proceedings of the 9th IEEE International Symposium on Wearable Computers,” pp. 152-159, October 2005.

[8] J. F. Dias, “Construction and performance of an experimental phased array acoustic imaging transducer,” *Ultrasonic Imaging,* vol. 3, pp. 352-368, 1981.

[9] B. T. Khuri-Yakub and O. Oralkan, "Capacitive micromachined ultrasonic transducers for medical imaging and therapy," *Journal of Micromechanics and Microengineering,* vol. 21, May 2011.

[10] P. Muralt, N. Ledermann, J. Baborowski, A. Barzegar, S. Gentil, B. Belgacem, *et al.*, "Piezoelectric micromachined ultrasonic transducers based on PZT thin films," *IEEE Transactions on Ultrasonics Ferroelectrics and Frequency Control,* vol. 52, pp. 2276-2288, Dec. 2005.

[11] G. G. Yaralioglu, A. S. Ergun, B. Bayram, E. Haeggstrom, and B. T. Khuri-Yakub, "Calculation and measurement of electromechanical coupling coefficient of capacitive micromachined ultrasonic transducers," *Ieee Transactions on Ultrasonics Ferroelectrics and Frequency Control,* vol. 50, pp. 449-456, Apr 2003.

[12] F. Sammoura, S. Akhbari, L. Lin, and S.-G. Kim, "Enhanced coupling of piezoelectric micromachined ultrasonic transducers with initial static deflection," in *2013 IEEE Sensors,* Baltimore, MD, USA, 2013, pp. 1-4.

[13] F. Sammoura, S. Akhari, N. Aqab, M. Mahmoud, and L. Lin, "Multiple electrode piezoelectric micromachined ultrasonic transducers," in *2014 IEEE International*

Ultrasonics Symposium (IUS), Chicago, IL, USA, 2014, pp. 305-308.

[14] F. Sammoura, S. Shelton, S. Akhbari, D. Horsley, and L. Lin, "A two-port piezoelectric micromachined ultrasonic transducer," in *Proc. 2014 Joint IEEE International Symposium on the Applications of Ferroelectrics, International Workshop on Acoustic Transduction Materials and Devices & Workshop on Piezoresponse Force Microscopy (ISAF/IWATMD/PFM),* State College, PA, 2014, pp. 1-4.

[15] S. Shelton, O. Rozen, A. Guedes, R. Przybyla, B. Boser, and D. A. Horsley, "Improved acoustic coupling of air-coupled micromachined ultrasonic transducers," in *Proc. 2014 IEEE 27th International Conference on Micro Electro Mechanical Systems (MEMS)*, San Francisco, CA, USA, 2014, pp. 753-756.

[16] Y. Lu, O. Rozen, H.-Y. Tang, G. L. Smith, S. Fung, B. E. Boser, *et al.*, "Broadband piezoelectric micromachined ultrasonic transducers based on dual resonance modes," in *Proc. 2015 28th IEEE International Conference on Micro Electro Mechanical Systems (MEMS),* Estoril, Portugal, 2015, pp. 146-149.

[17] S. Akhbari, F. Sammoura, C. Yang, M. Mahmoud, N. Aqab, and L. Lin, "Bimorph pMUT with dual electrodes," in *Proc. 2015 28th IEEE International Conference on Micro Electro Mechanical Systems (MEMS)*, Estoril, Portugal, 2015, pp. 928-931.

[18] S. Akhbari, F. Sammoura, B. Eovino, C. Yang, and L. Lin, “Bimorph Piezoelectric Micromachined Ultrasonic Transducers,” *J. Microelectromechanical Syst.*, pp. 1–11, 2016.

[19] G.-H. Feng, C. C. Sharp, Q. F. Zhou, W. Pang, E. S. Kim, and K. K. Shung, "Fabrication of MEMS ZnO dome-shaped-diaphragm transducers for high-frequency ultrasonic imaging," *Journal of Micromechanics and Microengineering,* vol. 15, pp. 586-590, March 2005.

[20] D. J. Morris, R. F. Need, M. J. Anderson, and D. F. Bahr, "Enhanced actuation and acoustic transduction by pressurization of micromachined piezoelectric diaphragms," *Sensors and Actuators a-Physical,* vol. 161, pp. 164-172, Jun 2010.

[21] A. Hajati, D. Latev, D. Gardner, A. Hajati, D. Imai, M. Torrey, *et al.*, "Three-dimensional micro electromechanical system piezoelectric ultrasound transducer," *Applied Physics Letters,* vol. 101, 17 Dec. 2012.

[22] F. Sammoura, S. Akhbari, and L. Lin, "An Analytical Solution for Curved Piezoelectric Micromachined Ultrasonic Transducers With Spherically Shaped Diaphragms," *IEEE Transactions on Ultrasonics Ferroelectrics and Frequency Control*, vol. 61, pp. 1533-1544, Sept. 2014.

[23] S. Akhbari, F. Sammoura, and L. Lin, "An equivalent circuit model for curved piezoelectric micromachined ultrasonic transducers with spherical-shape diaphragms," in *Proc. 2014 IEEE International Ultrasonics Symposium (IUS)*, Chicago, IL, USA, 2014, pp. 301-304.

[24] S. Akhbari, F. Sammoura, and L. Lin, “Equivalent Circuit Models for Large Arrays of Curved and Flat Piezoelectric Micromachined Ultrasonic Transducers,” *IEEE Trans. Ultrason. Ferroelectr. Freq. Control*, vol. 63, no. 3, pp. 432–447, 2016.

[25] S. Akhbari, F. Sammoura, S. Shelton, Y. Chen, D. Horsley, and L. Lin, "Highly responsive curved aluminum nitride pMUT," in *Proc. 2014 IEEE 27th International Conference on Micro Electro Mechanical Systems (MEMS)*, San Francisco, CA, USA, 2014, pp. 124-127.

[26] S. Akhbari, F. Sammoura, C. Yang, A. Heidari, D. Horsley, and L. Lin, "Self-curved diaphragms by stress engineering for highly responsive pMUT," in *Proc. 2015 28th IEEE International Conference on Micro Electro Mechanical Systems (MEMS)*, Estoril, Portugal, 2015, pp. 837-840.

[27] R. Krimholtz, D. A. Leedom, and G. L. Mathaei, “New Equivalent Circuit for Piezoelectric Transducers,” *Electronic Letters*, vol. 6, pp. 398-399 & 560, 1970.

[28] A. Lohfink and P. C. Eccardt, "Linear and nonlinear equivalent circuit modeling of CMUTs," *IEEE Transactions on Ultrasonics Ferroelectrics and Frequency Control*, vol. 52, pp. 2163-2172, Dec 2005.

[29] I. O. Wygant, M. Kupnik, and B. T. Khuri-yakub, “Analytically calculating membrane displacement and the equivalent circuit model of a circular CMUT cell,” in *2008 IEEE International Ultrasonics Symposium*, 2008, no. 6, pp. 2111–2114.

[30] H. Köymen, A. Atalar, E. Aydoğdu, C. Kocabaş, H. K. Oğuz, S. Olçum, A. Ozgurluk, and A. Ünlügedik, “An improved lumped element nonlinear circuit model for a circular CMUT cell,” *IEEE Trans. Ultrason. Ferroelectr. Freq. Control*, vol. 59, no. 8, pp. 1791–1799, 2012.

[31] H. K. Oguz, S. Olcum, M. N. Senlik, V. Taş, A. Atalar, and H. Köymen, “Nonlinear modeling of an immersed transmitting capacitive micromachined ultrasonic transducer for harmonic balance analysis.,” *IEEE Trans. Ultrason. Ferroelectr. Freq. Control*, vol. 57, no. 2, pp. 438–447, 2010.

[32] S. A. N. Prasad, Q. Gallas, S. Horowitz, B. Homeijer, B. V. Sankar, L. N. Cattafesta, *et al.*, "Analytical electroacoustic model of a piezoelectric composite circular plate," *Aiaa Journal*, vol. 44, pp. 2311-2318, Oct 2006.

[33] F. Sammoura, K. Smyth, and S. G. Kim., “Working Equations of a Circular Multimorph Piezoelectric Micromachined Ultrasonic Transducer,” in *Proc. 2012 IECON - 38th Annu. Conf. IEEE Ind. Electron. Soc.*, Canada, Montreal, pp. 3991-3996, October 25-28, 2012.

[34] K. Smyth, S. Bathurst, F. Sammoura, and S. G. Kim, “Analytic Solution for N-electrode actuated Piezoelectric Disk with Application to Piezoelectric Micromachnined Ultrasonic Transducers,” *IEEE Trans. Ultras. Ferroelectr. Freq. Control*, in press.

[35] F. Sammoura, K. Smyth, S. Bathurst, and S. G. Kim, “An Analytical Analysis of the

Sensitivity of Circular Piezoelectric Micromachined Ultrasonic Transducers to Residual Stress," *in Proc.* 2012 *IEEE Int. Ultrason. Symp. (IUS)*, pp. 485-489, Dresden, Germany, October 7-10, 2012.

[36] F. Sammoura, K. Smyth, and S. G. Kim, "An Accurate Equivalent Circuit for the Clamped Circular Multiple-Electrode PMUT with Residual Stress," *2013 IEEE International Ultrasonics Symposium (IUS)*, Prague, Czech Republic, July 21-25, 2013, accepted.

[37] F. Sammoura, K. Smyth, and S. G. Kim, "Optimizing the Electrode Size of Circular Bimorph Plates with Different Boundary Conditions for Maximum Deflection of Piezoelectric Micromachined Ultrasonic Transducers," *Ultrasonics*, vol. 53, pp. 328-334, February 2013.

[38] F. Sammoura, K. Smyth, and S. G. Kim, "Piezoelectric Micromachined Ultrasonic Transducer (PMUT) with Patterned Electrodes for Large Deflection and Acoustic Pressure Output," USPTO Patent Application 13/34247.

[39] F. Sammoura and S. G. Kim, "Theoretical Modeling and Equivalent Electric Circuit of a Bimorph Piezoelectric Micromachined Ultrasonic Transducer," *IEEE Trans. Ultras. Ferroelectr. Freq. Control*, vol. 59, no. 5, pp. 990-998, May 2012.

[40] F. Sammoura, K. Smyth, and S. G. Kim, "An Equivalent Network Representation of a Clamped Bimorph Piezoelectric Micromachined Ultrasonic Transducer with Circular and Annular Electrodes using Matrix Manipulation Techniques," *IEEE Transactions on Ultrasonics, Ferroelectrics, and Frequency Control*, in press. pp. 1989-2003, vol. 60, no. 9, September 2013.

[41] J. Peng, C. Chao, and H. Tang, "Piezoelectric micromachined ultrasonic transducer based on dome-shaped piezoelectric single layer," *Microsyst. Technol.*, vol. 16, pp. 1771-1775, 2010.

[42] M. Toda and S. Tosima, "Theory of Curved, Clamped, Piezoelectric Film, Air-Borne Transducers," *IEEE Transactions on Ultrasonics, Ferroelectrics, and Frequency Control*, in press. pp. 1421-1431, vol. 47, no. 6, November 2000.

[43] J. Berry, "On thin hemispherical shells subjected to concentrated edge moments and forces," *Proceedings of the Midwestern Conference on Solid Mechanics*, pp. 25-44, 1955.

[44] P. M. Naghdi and A. Kalnins, "On Vibrations on Elastic Spherical Shells," *Journal of Applied Mechanics*, pp. 65-72, March 1962.

[45] D. M. Mills, "Medical imaging with capacitive micromachined ultrasound transducer (cMUT) arrays," in *Proceedings - IEEE Ultrasonics Symposium*, 2004, vol. 1, no. c, pp. 384–390.

[46] F. L. Degertekin, R. O. Guldiken, and M. Karaman, "Annular-ring CMUT arrays for forward-looking IVUS: Transducer characterization and imaging," *IEEE Trans.*

Ultrason. Ferroelectr. Freq. Control, vol. 53, no. 2, pp. 474–482, 2006.

[47] D. E. Dausch, J. B. Castellucci, D. R. Chou, O. T. von Ramm, and Ieee, "Piezoelectric Micromachined Ultrasound Transducer (pMUT) Arrays for 3D Imaging Probes," in *2006 IEEE Ultrasonics Symposium, Vols 1-5, Proceedings,* Vancouver, CANADA, 2006, pp. 934-937.

[48] Y. Yang, H. Tian, Y.-F. Wang, Y. Shu, C.-J. Zhou, H. Sun, *et al.*, "An Ultra-High Element Density pMUT Array with Low Crosstalk for 3-D Medical Imaging," *Sensors,* vol. 13, pp. 9624-34, July 2013.

[49] Y. Lu, H.-Y. Tang, S. Fung, B. E. Boser, and D. A. Horsley, "Short-range and high-resolution ultrasound imaging using an 8 MHz Aluminum Nitride PMUT array," in *Proc. 2015 28th IEEE International Conference on Micro Electro Mechanical Systems (MEMS),* Estoril, Portugal, 2015, pp. 140-143.

[50] J. Jung, S. Kim, W. Lee, and H. Choi, "Fabrication of a two-dimensional piezoelectric micromachined ultrasonic transducer array using a top-crossover-to-bottom structure and metal bridge connections," *Journal of Micromechanics and Microengineering,* vol. 23, p. 125037 (9 pp.), Nov. 2013.

[51] R. J. Przybyla, H.-Y. Tang, A. Guedes, S. E. Shelton, D. A. Horsley, and B. E. Boser, "3D Ultrasonic Rangefinder on a Chip," *IEEE Journal of Solid-State Circuits,* vol. 50, pp. 320-334, Jan. 2015.

[52] COMSOL Multiphysics (version 4.3) [software], (2012).

[53] ANSYS (version 14.5) [software], (2012).

[54] Ultrasim (version 07) [software], (2011), University of Oslo, Nordre Aker, Oslo, Norway.

[55] FOCUS (Fast Object-oriented C++ Ultrasound Simulation) (version 0.796) [software], (2015). Michigan State University, MI, USA.

[56] B. Bayram, M. Kupnik, G. G. Yaralioglu, Ö. Oralkan, A. S. Ergun, D. S. Lin, S. H. Wong, and B. T. Khuri-Yakub, “Finite element modeling and experimental characterization of crosstalk in 1-D CMUT arrays,” *IEEE Trans. Ultrason. Ferroelectr. Freq. Control*, vol. 54, no. 2, pp. 418–429, 2007.

[57] H. K. Oguz , A. Atalar, and H. Koymen, "Equivalent Circuit-Based Analysis of CMUT Cell Dynamics in Arrays (vol 60, pg 1016, 2013)," *IEEE Transactions on Ultrasonics Ferroelectrics and Frequency Control,* vol. 60, pp. 1016-1024, May 2013.

[58] D. T. Porter, "Self- and Mutual-Radiation Impedance and Beam Patterns for Flexural Disks in a Rigid Plane," *Journal of the Acoustical Society of America,* vol. 36, pp. 1154-&, 1964 1964.

[59] M. N. Senlik, S. Olcum, H. Koymen, and A. Atalar, “Radiation impedance of an array of circular capacitive micromachined ultrasonic transducers,” *IEEE Trans. Ultrason.*

Ferroelectr. Freq. Control, vol. 57, no. 4, pp. 969–976, 2010.

[60] A. Atalar, H. Köymen, and H. K. Oguz, “Rayleigh – Bloch Waves in CMUT Arrays,” *IEEE Trans. Ultrason. Ferroelectr. Freq. Control*, vol. 61, no. 12, 2014.

[61] J. N. Reddy, Theory and Analysis of Elastic Plates and Shells, 2nd ed., Boca Raton, FL: CRC Press, 2007.

[62] T. Ikeda, Fundamentals of Piezoelectricity. New York, NY: Oxford University Press, 1990.

[63] S. Shelton et al., “CMOS-Compatible AlN Piezoelectric Micromachined Ultrasonic Transducers,” *2009 IEEE International Ultrasonics Symposium (IUS)*, pp. 402-405, Rome, Italy, September 20-23, 2009.

[64] F. V. Hunt, *Electroacoustics: The Analysis of Transduction, and Its Historical Background*. New York, NY: Acoustical Society of America,1954.

[65] D. A. Berlincourt, D. R. Curran. H. Jaffe, "Piezoelectric and piezomagnetic materials and their function in transducers," in *Physical Acoustics*, vol. I, Part A, New York: Academic Press, 1964, pp. 233-256.

[66] A. Erturk and D. J. Inman, “An experimentally validated bimorph cantilever model for piezoelectric energy harvesting from base excitations,” Smart Mater. Struct., vol. 18 (2009) 025009.

[67] D. T. Blackstock, Fundamentals of Physical Acoustics. John Wiley & Sons, 2000

[68] C. Rubin, M. Bolander, J. P. Ryaby, and M. Hadjiargyrou, “The use of low-intensity ultrasound to accelerate the healing of fractures.,” *J. Bone Joint Surg. Am.*, vol. 83-A, pp. 259–270, 2001.

[69] J. W. Busse, M. Bhandari, A. V. Kulkarni, and E. Tunks, “The effect of low-intensity pulsed ultrasound therapy on time to fracture healing: A meta-analysis,” *Cmaj*, vol. 166, no. 4, pp. 437–441, 2002.

[70] S. J. Warden, “A new direction for ultrasound therapy in sports medicine.,” *Sports Med.*, vol. 33, no. 2, pp. 95–107, 2003.

[71] S. Jingushi, K. Mizuno, T. Matsushita, and M. Itoman, “Low-intensity pulsed ultrasound treatment for postoperative delayed union or nonunion of long bone fractures.,” *J. Orthop. Sci.*, vol. 12, no. 1, pp. 35–41, 2007.

[72] J. Jung, S. Kim, W. Lee, and H. Choi, "Fabrication of a two-dimensional piezoelectric micromachined ultrasonic transducer array using a top-crossover-to-bottom structure and metal bridge connections," *Journal of Micromechanics and Microengineering*, vol. 23, p. 125037 (9 pp.), Nov. 2013.

[73] D. E. Dausch, J. B. Castellucci, D. R. Chou, and O. T. von Ramm, "Piezoelectric Micromachined Ultrasound Transducer (pMUT) Arrays for 3D Imaging Probes," in

2006 IEEE Ultrasonics Symposium, Vols 1-5, Proceedings, Vancouver, CANADA, 2006, pp. 934-937.

[74] Y. Lu, S. Shelton, and D. A. Horsley, "High frequency and high fill factor piezoelectric micromachined ultrasonic transducers based on cavity SOI wafers," in *Proc. Solid-State Sensors, Actuators and Microsystems Workshop,* Hilton Head, SC, 2014, pp. 131-134.

[75] H. Tang, Y. Lu, S. Fung, J. M. Tsai, M. Daneman, D. A. Horsley, and B. E. Boser, "Pulse-Echo Ultrasonic Fingerprint Sensor on A Chip," in *the Int. Conf. Solid- State Sensors, Actuators & Microsystems (Transducers),* Achorage, Ak, USA, 2015, pp. 674-677.

[76] Y. Lu, H.-Y. Tang, S. Fung, B. E. Boser, and D. A. Horsley, "Short-range and high-resolution ultrasound imaging using an 8 MHz Aluminum Nitride PMUT array," in *Proc. 2015 28th IEEE International Conference on Micro Electro Mechanical Systems (MEMS),* Estoril, Portugal, 2015, pp. 140-143.

[77] C. Bayram, S. Olcum, M. N. Senlik, and A. Atalar, “Bandwidth improvement in a cMUT array with mixed sized elements,” in *IEEE International Ultrasonics Symposium*, 2005, vol. 00, no. c, pp. 1956–1959.

[78] S. Olcum, M. N. Senlik, and A. Atalar, “Optimization of the gain-bandwidth product of capacitive micromachined ultrasonic transducers.,” IEEE Trans. Ultrason. Ferroelectr. Freq. Control, vol. 52, no. 12, pp. 2211–9, 2005.

[79] R. Porter and D. V. Evans, “Rayleigh–Bloch surface waves along periodic gratings and their connection with trapped modes in waveguides,” *J. Fluid Mech.*, vol. 386, no. 1, pp. 233–258, 1999.

[80] A. Rønnekleiv, “CMUT array modeling through free acoustic CMUT modes and analysis of the fluid-CMUT interface through Fourier transform methods,” *IEEE Trans. Ultrason. Ferroelectr. Freq. Control*, vol. 52, no. 12, pp. 2173–2184, 2005.

[81] Wilm, A. Reinhardt, V. Laude, R. Armati, W. Daniau, and S. Ballandras, “Three dimensional modelling of micromachined-ultrasonic- transducer arrays operating in water,” *Ultrasonics*, vol. 43, no. 6, pp. 457–465, 2005.

[82] MATLAB (version R2014b) [software], (2014), The MathWorks Inc., Natick, MA, USA.

[83] E. E. Drakonaki, G. M. Allen, and D. J. Wilson, “Ultrasound elastography for musculoskeletal applications,” *Br. J. Radiol.*, vol. 85, no. 1019, pp. 1435–1445, 2012.

[84] K. J. Parker, D. Fu, S. M. GRACESWKI, F. YEUNG, and S. F. LEVINSON, “VIBRATION SONOELASTOGRAPHY AND THE DETECTABILITY OF LESIONS,” *Ultrasound Med. Biol*, vol. 24, no. 9, pp. 1437–1447, 1998.

[85] Y. Li and J. G. Snedeker, “Elastography: Modality-specific approaches, clinical

applications, and research horizons,” *Skeletal Radiol.*, vol. 40, no. 4, pp. 389–397, 2011.

[86] C. H. Wu, W. S. Chen, G. Y. Park, T. G. Wang, and H. L. Lew, “Musculoskeletal Sonoelastography: A Focused Review of its Diagnostic Applications for Evaluating Tendons and Fascia,” *J. Med. Ultrasound*, vol. 20, no. 2, pp. 79–86, 2012.

[87] K. Hoyt, T. Kneezel, B. Castaneda, and K. J. Parker, “Quantitative sonoelastography for the in vivo assessment of skeletal muscle viscoelasticity.,” *Phys. Med. Biol.*, vol. 53, no. 15, pp. 4063–4080, 2008.

[88] E. a. Barannik, a. Girnyk, V. Tovstiak, a. I. Marusenko, S. Y. Emelianov, and a. P. Sarvazyan, “Doppler ultrasound detection of shear waves remotely induced in tissue phantoms and tissue in vitro,” *Ultrasonics*, vol. 40, no. 1–8, pp. 849–852, 2002.

[89] Z. Wang, A. a. Volinsky, and N. D. Gallant, “Crosslinking effect on polydimethylsiloxane elastic modulus measured by custom-built compression instrument,” *J. Appl. Polym. Sci.*, vol. 41050, pp. 1–4, 2014.

[90] R. N. Palchesko, L. Zhang, Y. Sun, and A. W. Feinberg, “Development of Polydimethylsiloxane Substrates with Tunable Elastic Modulus to Study Cell Mechanobiology in Muscle and Nerve,” *PLoS One*, vol. 7, no. 12, 2012.

[91] (2016, March 31). Supplementary Material (ESI) for Lab on a Chip, This journal is © The Royal Society of Chemistry 2007 [online]. Available: http://www.rsc.org/suppdata/lc/b7/b704449f/b704449f.pdf

[92] (2016, March 31). TYPICAL ACOUSTIC PROPERTIES OF TISSUES [online]. Available: http://onlinelibrary.wiley.com/doi/10.1002/9780470561478.app1/pdf

[93] S. T. Chan, P. K. Fung, N. Y. Ng, T. L. Ngan, M. Y. Chong, C. N. Tang, J. F. He, and Y. P. Zheng, “Dynamic changes of elasticity, cross-sectional area, and fat infiltration of multifidus at different postures in men with chronic low back pain,” *Spine J.*, vol. 12, no. 5, pp. 381–388, 2012.

[94] E. J. Chen, J. Novakofski, W. K. Jenkins, and W. D. O. Brien, “Young’s Modulus Measurements of Soft Tissues with Application to Elasticity Imaging,” *IEEE Trans. Ultrason. Ferroelectr. Freq. Control*, vol. 43, no. 1, pp. 191–194, 1996.

[95] J. L. Sparks, N. a Vavalle, K. E. Kasting, B. Long, M. L. Tanaka, P. a Sanger, K. Schnell, and T. a Conner-kerr, “Use of Silicone Materials to Simulate Tissue Biomechanics as Related to Deep Tissue Injury,” *Adv. Ski. Wound Care*, vol. 28, no. 2, pp. 59–68, 2015.

[96] A. C. M. Kuo, *Poly (dimethylsiloxane)*. Oxford University Press, Inc., 1999.

[97] S. Akhbari, A. Voie, Z. Li, B. Eovino, and L. Lin, "Dual-electrode Bimorph PMUT Arrays for Hanhled Therapeutic Medical Devices," in *Proc. 2016 29th IEEE International Conference on Micro Electro Mechanical Systems (MEMS)*, Shanghai, China, 2016, pp. 1102-1105.

[98] J. S. Petrofsky, M. Prowse, and E. Lohman, “The influence of ageing and diabetes on skin and subcutaneous fat thickness in different regions of the body,” *J. Appl. Res.*, vol. 8, no. 1, pp. 55–61, 2008.

[99] A. C. Dupont, E. E. Sauerbrei, P. V. Fenton, P. C. Shragge, G. E. Loeb, and F. J. R. Richmond, “Real-time sonography to estimate muscle thickness: Comparison with MRI and CT,” *J. Clin. Ultrasound*, vol. 29, no. 4, pp. 230–236, 2001.

[100] L. E. Kinsler et al. (2000), Fundamentals of acoustics, 4th Ed., John Wiley and sons Inc., New York, USA.